

Micro and nanofibrillated cellulose (MNFC) as additive in complex suspensions : influence on rheology and dewatering

Katarina Dimic-Misic



Micro and nanofibrillated cellulose (MNFC) as additive in complex suspensions: influence on rheology and dewatering

Katarina Dimic-Misic

A doctoral dissertation completed for the degree of Doctor of Science (Technology) to be defended, with the permission of the Aalto University School of Chemical Technology at a public examination in Auditorium Puu 2 at the Aalto University School of Chemical Technology (Espoo, Finland) on the 12th of June 2014 at 12 noon.

Aalto University
School of Chemical Technology
Department of Forest Product Technology
Natural Fiber Products

Supervising professor

Professor Jouni Paltakari

Thesis advisor

Professor Patrick Gane

Preliminary examiners

Professor Jasna Djonlagic,
Faculty of Technology and Metallurgy, University of Belgrade, Serbia
Professor Markku Kataja,
Department of Physics, University of Jyväskylä, Finland

Opponents

Professor Daniel Söderberg,
KTH Royal Institute of Technology, Stockholm, Sweden

Aalto University publication series

DOCTORAL DISSERTATIONS 73/2014

© Katarina Dimic-Misic

ISBN 978-952-60-5696-8

ISBN 978-952-60-5697-5 (pdf)

ISSN-L 1799-4934

ISSN 1799-4934 (printed)

ISSN 1799-4942 (pdf)

<http://urn.fi/URN:ISBN:978-952-60-5697-5>

Unigrafia Oy

Helsinki 2014

Finland

Publication orders (printed book):

Unigrafia Oy, Helsinki

Author

Katarina Dimic-Misic

Name of the doctoral dissertation

Micro and nanofibrillated cellulose (MNFC) as additive in complex suspensions: influence on rheology and dewatering

Publisher School of Chemical Technology

Unit Department of Forest Product Technology

Series Aalto University publication series DOCTORAL DISSERTATIONS 73/2014

Field of research Natural Fiber Product

Manuscript submitted 30 January 2014

Date of the defence 12 June 2014

Permission to publish granted (date) 5 March 2014

Language English

Monograph

Article dissertation (summary + original articles)

Abstract

The traditional forest products, such as paper, packaging and viscose products, have their well-established place, but further efforts urgently need to be made to meet growing ecological demands, increasing economic pressure and to develop new technologies for utilisation of high performance materials. Nanocellulose applied in paper making suspensions and as water retention control aids may introduce additional strength properties in traditional products, and when considered for coatings may deliver oil and gas barrier properties as well as targeted liquid interactions based on surface energy criteria and designed pore and gel network structures. The properties increase the potential for their use in a broad range of novel products. The processes, firstly by which nanocellulose is both created, as part of cellulose structures in nature, and subsequently produced determine their aqueous suspension rheology and dewatering behaviour, and thus, by using knowledge of their rheological behaviour when utilised in complex suspensions, will support the creation of new controls in water-based production processes.

The use of rheology for the characterisation of nanocellulose suspensions and their applications in a range of industries as diverse as the oil and papermaking industries has been the subject of numerous studies in recent years. Although many studies have been conducted relating to papermaking furnishes and their water suspensions while including nanocellulose containing materials, these rheological investigations were conducted independently from conditions of dynamic dewatering. For the first time, this work sets out to observe and try to overcome experimental difficulties related to rheometry and dynamic dewatering of high consistency viscoelastic gel-like nanocellulose suspensions using a variety of experimental techniques and methods.

Once reliable rheological measurements were designed and the methodology established, the work goes on to analyse the possible structures attained by nanocellulose containing suspensions in combination with macroscopic fibres, pigments and fibril dispersing polymers, which traditionally are used as pigment flocculant water retention aids. These analyses are used to support and challenge the basic hypotheses of the thesis in relation to the impact these structures will have on properties such as process applicability, phase separation, substrate coverage, coating and material uniformity.

Keywords rheology, nanocellulose, coating, dewatering, immobilisation

ISBN (printed) 978-952-60-5696-8

ISBN (pdf) 978-952-60-5697-5

ISSN-L 1799-4934

ISSN (printed) 1799-4934

ISSN (pdf) 1799-4942

Location of publisher Helsinki

Location of printing Helsinki

Year 2014

Pages 281

urn <http://urn.fi/URN:ISBN:978-952-60-5697-5>

**Micro and nanofibrillated cellulose
(MNFC) as additive in complex
suspensions: influence on rheology
and dewatering**

Katarina Dimic-Misic

2014

**This thesis is dedicated to my late father Prof. Dr. Tech. Miroljub Dimic.
His love and words of encouragement remain always with me.**

“I do not think there is any thrill that can go through the human heart like that felt by the inventor as he sees some creation of the brain unfolding to success . . . Such emotions make a man forget food, sleep, friends, love, everything.”

“One must be sane to think clearly, but one can think deeply and be quite insane.”

Nikola Tesla (1856-1943), Serbian-born American immigrant

Acknowledgements

I thank Professor Hannu Paulapuro for introducing me (mother of two) to the, at that time novel, area of the rheometrical study of coating colour suspension immobilisation during dewatering, and giving me the opportunity for postgraduate studies. I feel honoured to graduate with a topic from the field of rheology, to step into the world of “Panta Rhei” and realise truth of the words, “no man ever steps into the same river twice”, from the father of rheology, Heraclitus (c.535-c.475).

I was fortunate to be able to finalise this thesis and previously complete a Licentiate thesis under the supervision of Professor Jouni Paltakari, who accepted me back to school (then already mother of three) after many years spent abroad, and introduced me to the fascinating world of nanofibrillar cellulose, giving me freedom in developing research methods.

I also thank Professor Thaddeus Maloney for generously accepting me into his team and Effnet project, introducing me (DI mechanical engineer) to the importance of surface chemistry in the complexity of nanocellulose research. He opened many doors for me, one of them was into Professor Mikko Alava’s rheology “Disneyland”.

This thesis, nor in fact the future of nanocellulose based coatings, would not be the same without the help of Professor Patrick Gane, who generously treated me as one of his own students, providing patient guidance with never – ending ideas, through the last and most difficult stages of my work. He introduced me to the world of porosimetry and the amazing way of connecting things in research. I have learnt so much from him and, through that process, realised that real science is both talent and hard work, which “never sleeps”.

I wish to express my gratitude to my two pre-examiners, Professor Jasna Djonlagic and Professor Markku Kataja for critical and efficient evaluation of this thesis.

I am grateful to Professor Herbert Sixta for his tolerance and support, as his team members were always there for me. Thanks to Dr. Michael Hummel I was able to perform very difficult rheological measurements successfully, as he was always there to help and discuss. My dear friend and co-author Kaarlo Nieminen helped me with the smoothing of enormous amounts of initially strange looking data through the years. Finally, we even ended up developing our own “method”. I cannot imagine going into rheology of high consistency complex suspensions without the help of my dear co-author, Dr. Antti Puisto, true master of his art! I see that my valued co-author Mikael Mohtaschemi is following in his footsteps. Many thanks to my co-author, Dr. Cathy Ridgway, of Omya International AG, for collaboration with the detailed porosimetric analysis and liquid-pore structure interactions in coatings, for her patient teaching, and making my time visiting Professor Gane’s “Omya R&D” laboratory an enjoyable experience.

Working on this thesis has been less stressful knowing that one had great support from my colleagues that one can count on. Good friends and excellent technicians Leena Nolvi, Nguyen Tuyen, and Christian Orassaari, with my co-author Tuomo Salo provided the

great service of checking out my challenging “chemical” calculations. I am also grateful to fellow researcher Naveen Chenna for good humour and valuable help with RefWork. Special thanks go to office mates, Anne Vikkula, Heikki Hannukainen, Eveliina Jutila and Terhi Toivari.

Sirje Liukko became my very close friend through our mutual work processes, and encouraged me daily, with real “girl power”. Also, I cannot imagine finalising this thesis without the spiritual support of my dear friend, researcher Shailesh Chouhan, who was always there for me. To many other friends, “outside the Aalto”, who helped me through the years, and who shared hardships and jokes with me, I thank you.

My sincerest thanks go to my family members for their unwavering support and love. My deep gratitude goes to my mother Dragica Dimic, for flying long distance to replace me at home for so many months, far away from the Serbian sun. My father Mirosljub Dimic, the last and final time we met, helped me with polishing tablet samples used for porosimetric analysis, which I brought to Belgrade to grind, throwing in a joke that at the end of his life I am pushing him into supporting Finnish science.

I want to apologise to my children, my golden boys, Viktor, Filip and Marko for all those days and weekends that I was not at home, and I hope they will understand one day that this was another kind of love, but deep love also.

Finally, without the tremendous understanding and patience of my husband Stefan Mistic it all would never have been conceivable.

List of publications

This thesis is based on the following list of publications. The listed journal publications have been peer-reviewed. For all publications, the principal author (thesis author) undertook the major role in preparation and execution of measurements, analysis of results and first draft of the manuscript.

[I] Katarina Dimic-Misic, Antti Puisto, Patrick Gane, Kaarlo Nieminen, Mikko Alava, Jouni Paltakari, Thaddeus Maloney (2013) *The role of MFC/NFC swelling in the rheological behavior and dewatering of high consistency furnishes*, Cellulose 6: 2847-2861

[II] Katarina Dimic-Misic, Antti Puisto, Jouni Paltakari, Mikko Alava, Thaddeus Maloney (2013) *The influence of shear on the dewatering of high consistency nanofibrillated cellulose furnishes*, Cellulose 20:1853-2020

[III] Katarina Dimic-Misic, Patrick Gane, Jouni Paltakari (2013): *Micro and nanofibrillated cellulose as rheology modifier additive in CMC-containing pigment coating formulations*, Industrial and Engineering Chemistry Research 52: 16055-16083

[IV] Katarina Dimic-Misic, Tuomo Salo, Jouni Paltakari, Patrick Gane (2014) *Comparing the Rheological Properties of Novel Nanofibrillar Cellulose-formulated Pigment Coating Colours with those using Traditional Thickener*, Nordic Pulp and Paper Journal 29: 253-270

[V] Katarina Dimic-Misic, Cathy Ridgway, Thaddeus Maloney, Jouni Paltakari, Patrick Gane (2014) *Influence on pore structure of micro/nanofibrillar cellulose in pigmented coating formulations*, Transport in Porous Media: DOI10.1007/s11242-014-0293-8

[VI] Mikael Mohtaschemi, Katarina Dimic-Misic, Antti Puisto, Marko Korhonen, Thaddeus Maloney, Jouni Paltakari, Mikko Alava (2014) *Rheological characterisation of fibrillated cellulose suspensions via bucket vane viscometer*, Cellulose : 10.107/s10570-014-0235-1

[VII] Associated publication

Katarina Dimic-Misic, Kaarlo Nieminen, Patrick Gane, Thaddeus Maloney, Herbert Sixta, Jouni Paltakari (2014) *Deriving a process viscosity for complex particulate nanofibrillar cellulose gel-containing suspensions*, Applied Rheology 29: 35616

Principal author's contributions in relation to co-authors

In all publications, the principal author carried out all rheological and dewatering measurements, data analysis and reporting of the results, and wrote the first draft of the manuscript.

Publications **I, II, III, IV, V, VI**: author prepared samples of MNFC suspensions, MNFC furnishes and coating colours.

Publications **II, III, IV**: smoothing of raw data in immobilisation measurements was performed by assistance of Kaarlo Nieminen.

Publication **IV**: coating colours were prepared by Tuomo Salo.

Publication **V**: liquid absorption and permeability measurements, together with their analyses, were performed by Dr. Cathy Ridgway, Omya International AG, and Prof. Patrick Gane, Aalto University and Omya International AG.

Publication **VI**: author was assisted in data analysis, reporting and first draft manuscript writing by Mikael Mohtaschemi.

Nomenclature and Abbreviations

3ITT	3 interval time test
A_{IMC}	cross-sectional area/filter area (IMC and permeability) (m^2)
$A_{\text{ÅA-GWR}}$	cross-sectional area/filter area (ÅA-GWR) (m^2)
ÅA-GWR	Åbo Akademi gravimetric dewatering device
a_p	radius of isolated particle (m)
b	fitting constant Darcy Law
c	mass concentration (%)
c_c	cross exponent - Carreau model
cGCC	coarse particle size ground calcium carbonate
C_m	mass consistency (%)
CMC	carboxymethyl cellulose
CNC	crystalline nanocellulose
CSR	controlled stress (mode) rheometry
C_v	volumetric concentration (%)
$c_{V(t)}$	mass of the compact bed at time t (g)
d	capillary diameter (m)
d	fibre diameter (m)
De	Deborah number
DLS	dynamic light scattering
DP	degree of polymerisation
D_p	particle diameter (m)
DS	degree of substitution (NFC)
DSC	differential scanning calorimetry
DSO	direct strain oscillation mode
dV/dt	volume flow rate (m^3s^{-1})
FCC	first critical concentration
fGCC	fine particle size ground calcium carbonate
FTIR	Fourier-transform-infrared spectrometry
G	relaxation modulus (Pa)
G	Gibbs free energy (J mol^{-1})
G^*	complex shear modulus (Pa)
G'	dynamic storage shear modulus / elastic modulus (Pa)
G''	dynamic loss shear modulus /viscous modulus (Pa)
G_0'	initial dynamic storage shear modulus /initial elastic modulus (at the beginning of the measurement) (Pa)
G_0''	initial dynamic loss modulus / linitial oss modulus (Pa)/ (at the beginning of the measurement) (Pa)

G_G	Gibbs free energy of the gel (Jmol ⁻¹)
G_{Coul}	Coulombic interaction energy (Jmol ⁻¹)
G_{dis}	dissociation energy of acid groups on the available network sites (Jmol ⁻¹)
G_f'	final elastic modulus (Pa)/ at the end of measurement
G_{net}	free energy of the neutral network (Jmol ⁻¹)
G_{sol}	free energy for a dilute solution of ions or neutral molecules within the gel (Jmol ⁻¹)
$h(t)$	compact bed height (m)
h_0	height of the non-networked suspension filtration (m)
HB	Herschel-Bulkley function
Hg	mercury
IMC	immobilisation cell
k	flow index (power law)
k_v	flow index Herschel-Bulkley function (vane bucket geometry)
k_1	Kozeny shape factor
k_D	Darcy permeability coefficient (m ²)
k_{FC}	Filter cake permeability coefficient (IMC) (m ²)
k_e	elastic constant of the system
l	absorption length of tablet sample (m)
L	fibre length (m)
L	total length of the tablet sample (m).
$l(t)$	depth (extent) of permeable layer at time t (m)
l_{FC}^*	normalised apparent cake thickness (IMC) (mm ⁻³)
l_0	initial measuring gap (m)
l_a	apparent filter cake thickness (m)
l_e	effective measuring gap (m)
l_e	is the height of non-immobilised coating colour (m)
l_{FC}	filter cake thickness (m)
l_{ti}	measuring gap at the immobilisation time (m)
LVE	linear viscoelastic region
m	mass (g)
M	torque input by viscometer (Nm)
m	fitting constant Carman-Kozeny equation
$m_{after\ absorption(n)}$	mass after the respective absorption experiment
m_{dry}	the dry mass of the tablet (g)
MFC	microfibrillated cellulose

MFFT	minimum film forming temperature
MNFC	family of nanocellulose containing fibrillar materials
MRI	magnetic resonance imaging
M_{ss}	bulk modulus of the solid sample (MPa)
N	crowding number
n	power law exponent
NFC	nanofibrillar cellulose
OBA	optical brightening agent
P	applied pressure (Pa)
P^l	atmospheric pressure (Pa)
PCC	precipitated calcium carbonate
P_{ext}	external pressure (Pa)
p_g	pressure in the gel (Pa)
PVAc	poly (vinyl acetate)
PSD	particle size distribution
r	cylindrical hydraulic pore of radius (m)
R	membrane hydraulic resistance
$r(\phi)$	hydrodynamic interaction between nearest neighbour particles
R_v	radius of vane spindle edge (m)
R_c	outer radius of concentric cylinder (m)
SA - latex	styrene-acrylic latex
SB - latex	styrene-butadiene latex
SCC	second critical concentration
SEM	scanning electron microscopy
SR	Schopper-Riegler number
S_v	the specific volume surface area ($m^2 m^{-3}$)
t	time (s)
T	temperature ($^{\circ}C$)
T	viscometer torque (%)
$\tan \delta$	loss factor
T_{gs}	glass transition temperature ($^{\circ}C$)
t_i	immobilisation point (s)
t_p	immobilisation onset point (s)
UDV	ultrasonic Doppler velocimetry
$V_{swollen}$	volume of swollen gel (m^3)
V_0	gel volume in initial dry state (m^3)
V_{bulk}^1	specific sample bulk volume at atmospheric pressure ($cm^3 g^{-1}$)
$V(t)$	volume flow in time t (m^3)
V	filtrate volume (m^3)
V_{AA-GWR}	filtrate volume from gravimetric dewatering (m^3)
V_{IMC}	filtrate volume from IMC dynamic dewatering (m^3)
v_{FC}	volume of filter cake per unit volume filtrate ($m^3 m^{-3}$)

$V_{\text{Hg}(l)}$	total pore volume of the sample (cm^3)
V_{int}	volume of intrusion into the sample (m^3)
$V_{\text{liq}(n)}$	liquid volume within tablet wetting distance (m^3)
V_{obs}	intruded mercury volume reading (m^3)
δV_{blank}	change in the blank run volume reading (cm^3)
V_p	average particle volume (m^3)
W_b	bound water content (g)
W_c	water content (g)
W_f	mass of free water (g)
w_f	fibre coarseness (g m^{-1})
W_{fb}	mass of freezing bound water (g)
W_{nf}	mass of non-freezing water (g)
WRV	water retention value (g g^{-1})
w/w%	weight/mass concentration (%)
x	liquid wicked distance (m)
x_p	distance of penetrated liquid (m)
ZS	Zetasizer Nano instrument
γ	strain (dimensionless or %)
γ_A	strain amplitude (dimensionless or %)
γ_c	critical strain (%)
γ_{LV}	liquid-vapour surface tension (Nm^{-1})
$\dot{\gamma}$	shear rate (s^{-1})
$\dot{\gamma}_c$	critical shear rate (s^{-1})
δ	phase angle
ΔH_{ml}	melting enthalpy (J g^{-1})
ΔP	pressure difference (Pa)
ε	the porosity or void volume
ζ	zeta potential (mV)
η	dynamic viscosity (Pa s)
η_v	dynamic viscosity (Brookfield viscometer) for given rpm (Pa s)
η^*	complex viscosity (Pa s)
η^+	transient viscosity (Pa s)
η_0	the zero shear dynamic viscosity of the filtrate (Pa s)
η_f	final dynamic viscosity (Pa s)/ at the end of measurement
$\eta_{t=1000}$	dynamic viscosity after 1000(s) (Pa s)
θ	contact angle at the liquid-solid contact line ($^\circ$)
α	specific compact bad resistance (m^{-2})
λ	characteristic relaxation time of a fluid
λ_{H}	exponent in the Herschel-Bulkley function (vane bucket geometry)
λ_{SD}	Stokes drag coefficient for an isolated particle
μ	chemical potential (μS)

τ	stress (Pa)
τ_A	stress amplitude (Pa)
τ_0^d	dynamic yield stress (Pa)
τ_0^s	static yield stress (Pa)
$\tau_{0(H)}^v$	dynamic yield stress with Herschel-Bulkley fit (viscometry) (Pa)
$\tau_0^y(\phi)$	compressive yield stress (Pa)
φ	volume fraction (dimensionless/ %)
φ_p	volume fraction of polymer/NFC in the swollen state (dimensionless/ %)
φ_{Hg}	volume intruded by porosimetry (cm ³)
ϕ	specific pore volume (cm ³ g ⁻¹)
Φ^1	porosity at atmospheric pressure (dimensionless/ %)
ϕ_{cc}	solid volume fraction in coating colour (dimensionless/ %)
ϕ_{FC}	solid volume fraction of filter cake (dimensionless/ %)
ϕ_g	volume fraction at fibre gel point (dimensionless/ %)
ϕ_m	volume fraction of particles in the filter cake (dimensionless/ %)
ψ	surface charge (mV)
ω	angular frequency (rad s ⁻¹)
Ω	rotational frequency of viscometer (min ⁻¹)

Table of Contents

Acknowledgments	i
List of Publications	iii
Nomenclature and Abbreviations	v
1 Introduction and outline of the study	1
1.1 The research questions to be answered and hypotheses of the thesis	1
1.2 Rheological behaviour of MFNC suspensions and its impact on dewatering	2
1.2.1 The influence of apparent swelling of MNFC on the rheological and dewatering properties of suspensions and high consistency nanocellulose based furnishes	3
1.2.2 Use of MFC/NFC in coating colours as a co-binder	4
2 Background of methodology and theory of measurements	6
2.1 From cellulose to nanocellulose	8
2.1.1 Microfibrillated cellulose MFC	9
2.1.2 Nanofibrillar cellulose NFC	10
2.1.3 Structural and rheological properties of MFC/NFC containing suspensions	11
2.1.4 Surface interactions between MNFC	12
2.1.5 Bound water on surface of MNFC	14
2.2 Viscoelasticity	15
2.2.1 Microstructure affects viscoelastic behaviour of complex suspensions	15
2.2.2 Flow phenomena of non-Newtonian fluids	20
2.2.3 Fibre suspensions	27
2.2.4 Viscoelasticity and flow properties of MNFC	30
2.2.5 Wall slip and shear banding	31
2.2.6 Coating colours	33
2.3 Filtration	40
2.3.1 Modelling the filter cake formation	40
2.3.2 Filtration in paper forming	41
2.3.3 Formation of filter cake in coating colours	42
2.3.4 Gel water retention	43
2.4 Coating layer structure	44
2.4.1 Porosity of dry coating layer structure	44
3 Materials and methods	47
3.1 Materials sourcing	47
3.1.1 Pigments	47

3.1.2 MFC and NFC	48
3.1.3 Binders and co-binders used in coating colours.....	48
3.1.4 MFC/NFC suspensions	49
3.1.5 High consistency MNFC furnishes	50
3.1.6 Coating colours	51
3.2 Methods applied in the study	51
3.2.1 Specific surface area and agglomerate size measurements	51
3.2.2 Viscometry	52
3.2.3 Water retention test WRV	53
3.2.4 Particle level swelling	54
3.2.5 Rate of dewatering: static and dynamic measurements	55
3.2.6 Gravimetric dewatering measurement with the ÅA-GWR	55
3.2.7 Rheometry	56
3.2.8 Dynamic dewatering measurement with the Immobilisation Cell (IMC)	57
3.2.9 IMC measurement	58
3.2.10 Tablet forming	60
3.2.11 Mercury intrusion	61
3.2.12 The liquid absorption apparatus.....	62
3.2.13 Permeability measurement cell.....	63
3.2.14 Additional measurements	64
4 Experimental.....	67
4.1. Part I: MNFC suspensions	67
4.1.1 Viscometry, oscillatory rheometry and gravimetric dewatering.....	67
4.2 Part II: Application of MNFC in papermaking suspensions	75
4.2.1 Viscometry, oscillatory and gravimetric dewatering of high consistency MFNC furnishes.....	75
4.2.2 Immobilisation measurements (IMC) for high consistency MFNC furnishes..	77
4.2.3 Behaviour under shear rates conditions and implementation in shear-induced dewatering of high consistency MFNC furnishes	80
4.2.5 Use of MFC/NFC in coating colours as a co-binder.....	84
4.2.6 MFC/NFC compared as partial and total substitute for CMC in coating colours	94
4.3 Coating structure of MNFC containing coatings	101
4.3.1 SEM images for MNFC containing coatings	101
4.3.2 Mercury intrusion porosimetry : MNFC containing coatings	103
4.3.3 Hexadecane Absorption: non-polar liquid interaction with MNFC containing coatings.....	104
4.3.4 Water Absorption: rewetting interaction with MNFC containing coatings ...	105

4.3.5 Extractives present in MNFC containing coatings	108
4.3.6 Selective permeability of MNFC containing coatings.....	108
5 Conclusions	110
5.1 Future work	112
6 References	113

1 Introduction and Outline of the study

1.1 The research questions to be answered and hypotheses of the thesis

The main hypothesis of this thesis is that the rheological structure contribution of aqueous gel-like nanocellulose materials in complex papermaking suspensions and coating colours is to form a network matrix that will drastically change their processability and dewatering behaviour. Nanocellulose containing materials in this thesis is the term used to for microfibrillar cellulose (MFC) and nanofibrillar cellulose (NFC), and will be termed collectively as MNFC.

Central to the idea of utilisation of MNFC in the paper industry is the necessity of gaining deeper understanding in which way it will affect rheological and dewatering properties. Dewatering and filtration of high consistency MNFC based furnishes, and coating colours that have MNFC as co-binder, are expected to be different to that of classical cellulose fibre based furnishes and coating colours that have traditional co-binders.

However, there have been no controlled studies which incorporate differences in the MNFC types, with different swelling and water binding properties, and their impact on rheological and immobilisation behaviour. The target of this thesis is to analyse in detail, and therefore evaluate and validate, in which way utilisation of MNFC will affect rheological measurement complexity, processability and dewatering behaviour when implemented as

- (i) bonding enhancing additive in high consistency fibre-filler furnishes allowing an increase in amount of filler in papermaking furnishes,
- (ii) partial or total substitution of traditional co-binders in coating colour formulations.

To achieve this analysis it has been necessary to develop, modify and apply a variety of measurement and data handling techniques based primarily on

- (iii) new experimental design linked to the development of new schemes for manipulating rheological MNFC flow curves due to their non-linear behaviour.

The thesis findings are based on six publications. The schematic structure of the thesis and the publications are presented in Fig. 1.

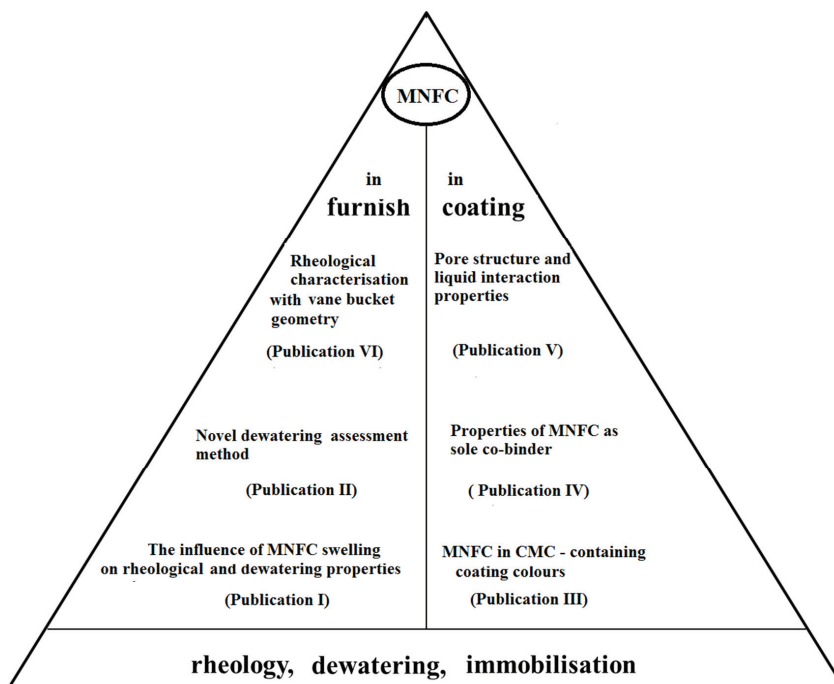


Figure 1 Schematic structure of publications presented in this thesis

The structure of this thesis follows research development and understanding of the behaviour of the rheological response of the individual MNFC component properties through learning to derive an interpretation of their mutual and interspecies interactions indirectly which are otherwise too complex to observe directly.

Web forming, wet pressing, drying or coating processes and related process equipment are essentially out of the scope of this study, and thus excluded. Nonetheless, the link between the rheological properties and the processability on papermaking and coating equipment can readily be inferred. The focus, therefore, is to show how implementation of MNFC containing gel forming suspensions can be employed in modifying and developing new operations and product qualities in paper, board and allied materials composites manufacturing.

1.2 Rheological behaviour of MNFC suspensions and its impact on dewatering

MNFC suspensions display very different properties compared with traditional pulp fibres, including higher particulate charge and water trapping properties in a polymer-like matrix rather than individual fibre structure swelling. Additionally, when combined with other components in composite structures, such as paper, board or coatings, the application of MNFC material demands the control of the complex interactions on a colloidal level, which manifests itself at the macro level in flow-related processes. Rheological analysis is a tool to probe the flow properties under shear and controlled

strain, simulating flow continuity and induced stress, as in a real industrial application. Physical parameters obtained by rheological measurements reveal the resulting average reaction of the suspension to externally applied changes in strain derived from the internal component interactions.

The main objectives of this rheological study are to determine what impact introducing MNFC in (i) paper furnish formulations and (ii) coating colour recipes as a co-binder will have on the derived complex suspension network strength, water retention and structure of the final product. The scope of this research includes utilising findings related to the influence of the production route on the agglomeration and colloidal gel-like nature of MNFC suspensions, which further influences its rheological dewatering properties, in order to propose ways in which these complex materials can successfully be measured, classified and applied.

The observation that nanocellulose could possibly be used in paper or other coating formulations as a co-binder opens questions related to porosity, pore size distribution and permeability of such coating layers as a function of coating layer thickness, and the reaction of such coatings when exposed to subsequent printing and the interaction with specific liquids and environmental factors in application. These topics are addressed by applying techniques of pore structure analysis, competitive liquid imbibition (polar and non-polar) and pressure-driven permeation.

1.2.1 The influence of apparent swelling of MNFC on the rheological and dewatering properties of suspensions and high consistency nanocellulose based furnishes

(Publications I, II, VI)

High consistency composite materials consisting of a mixture of traditional pulp fibres and MNFC have attracted much attention in recent years. Such composites are attractive due to the possibility to use reduced amounts of pulp fibres and drastically increased amounts of fillers, which is enabled via increased hydrogen bonding of high aspect ratio MNFC, which adds to the increase in both optical properties and strength of the final product. Problems arising in practice with such high consistency MNFC furnishes were related mainly to the difficulty in dewatering. Therefore, in order to propose novel processes for their implementation it is necessary to understand the complex behaviour in relation to dewatering and rheology of such systems (Publications I, II).

i) In Publication I, the flow behaviour of the MNFC materials was investigated and the findings related to flocculation of MFC and a high water binding gelation of NFC, which results in different viscoelastic effects and flow oriented structures during the rheological measurements. The influence of surface charge on the rheological and dewatering properties of nanocellulose suspensions was evaluated. This study introduced a new experimental method for evaluation of dewatering and rheological behaviour of both MNFC suspensions and high consistency furnishes, which is found to be influenced by the type of fibrillar nanocellulose and its source derivation. Establishing the method which will enable determination of immobilisation intervals, during which dewatering is shown to be a very slow process, will enable further research on the application of nanocellulose in complex high consistency suspensions.

ii) In Publication **II**, findings related to the gel-like nature of MNFC were accompanied with further determination of the impact of MNFC on the resultant high yield stress and strong shear thinning behaviour of high consistency furnishes, and whether these properties can be steered to apply shear induced dewatering. Exploiting the rheological characteristics of the MNFC containing high consistency furnishes it was possible to incorporate shear rotation in order to shear thin the furnish viscoelastic structure with intermediate application of vacuum. When the water trapping microstructure of the MNFC containing furnish is broken by the shear field, the process is able to propagate out-flow channels within the gel-like matrix. Afterwards, liberated water can be easily removed from the fluidised phase within the sample matrix by a simple vacuum.

iii) In Publication **VI** the bucket vane viscometer was utilised in order to avoid the wall-slip effect in order to probe the rheology of MFC and NFC suspensions. In addition, it was demonstrated that a correction method for non-Newtonian fluids in concentric cylinders geometry needs to be used to account for the highly non-linear rheological response of these materials.

1.2.2 Use of MNFC in coating colours as a co-binder

(Publications III, IV, V)

Paper surfaces are coated in order to provide a substrate with improved printability, optical properties and smoothness. Surface chemistry, inducing colloidal interaction between the components in a coating suspension, plays a significant role in the coating process, through stabilisation of suspension components and flocculation effects of co-binder on pigments and latex binder, which induces elasticity and develops static water retention. MNFC containing materials are potential additives which could at least partly substitute other natural and synthetic co-binders, such as viscoelasticity inducing starch, carboxymethyl cellulose (CMC) or polyacrylic thickeners, in paper coating colour formulations. In this part of the thesis, which investigates coating colours, an attempt made to determine whether MNFC can completely/partially substitute CMC as co-binder, in order to combine stiffness and strength generating properties of nanofibrillar material with its thickening and water retention behaviour, is reported. Systematic comparison of the rheological characteristics of coating colours and their dewatering and immobilisation, based on different pigments and utilising the findings from Publications **I** and **II**, enables an understanding of the mechanism by which MNFC will influence rheology and dewatering. Also to be reported here is the investigation of the effect of partial substitution of CMC with MNFC on the structural nature of the final coating layer through pore size and pore size distribution analysis.

i) In Publication **III**, MNFC variants are used to substitute, at least partially, the standard co-binder material CMC in pigmented coating colours. Rheological results show that MNFC material, being gel-like coagulants with high shear thinning properties, will not induce the standard type of pigment/latex-CMC flocculation within coating colour formulations, which would impart interesting properties of high water retention without generating inhomogeneous regions of flocculation in the end coating structure.

ii) Publication **IV** illustrates the validity of potential use of MNFC in coating colours as sole co-binder, which can be used in applications on slow running coaters. In the case of permeable substrates this approach could be used to implement gas barrier and oil resistant properties. In this investigation, the change of rheological and dewatering

behaviour of coating colours is studied when CMC is used as sole co-binder and during its partial and total replacement with MNFC. This study identifies the importance of the presence of a small amount of polymer thickener in the coating colour matrix when MNFC is used as a co-binder, to ensure the minimal amount of pigment/latex flocculation needed to provide elasticity recovery and particle interlocking at immobilisation.

iii) Publication **V** reports the effect of gel-like MNFC immobilisation on the pore structure of pigment coatings when they partially substitute CMC (Publications **I** and **III**). The pore structure of pigmented coatings, liquid absorption and permeability is analysed in respect to the influence of partially substituting CMC with MNFC. Mercury porosimetry, permeability, and the differences in absorption rate with respect to the polar (water) and non-polar liquid (hexadecane), are combined to determine the coating layer structure, effective pore connectivity and pore size distribution. Differentiation of absorption between the polar and non-polar liquids impacts on the likely printing properties for a wide range of printing techniques.

2 Background of methodology and theory of measurements

This thesis uses rheology as a tool to answer questions related to the way in which processability of MNFC affects its application. Firstly the focus is placed on how using MNFC in a furnish mix for paper and board manufacture can influence paper suspension rheological and dewatering behaviour, and therefore the literature review which follows considers literature which connects processability of various papermaking suspensions with their rheology and that of the MNFC they contain.

As the MNFC materials are greatly influenced not only by the processing method but also by the source of cellulose, the thesis considers briefly different sources and production routes and their consequently different properties to that of traditional cellulose fibres. The properties of MNFC create a high sensitivity to physical and chemical surface activity within MNFC suspensions. Differences in production route and different pre-treatments of MNFC result in different amounts and availability of reactive carboxyl groups.

Association of particles and/or interphase association, here in the presence of MNFC, related to particle-particle, particle-polymer and particle-water interactions induces formation of an internal structural three-dimensional network in aqueous suspension. This is such as between particles or typical water based polymers and bound water, or strong repulsion at high solids content, discussed in terms of the solid particles and polymers dispersed into the liquid phase, which provide the largest component effects of non-Newtonian fluids, in which group fall also paper making suspensions, i.e. coating colour suspensions, fibre suspensions and, of main interest here, MNFC colloids. Bulk rheological properties of complex suspensions depend on the net potential energy manifested by the many secondary forces (electrostatic, van der Waals, steric or solvation) and mechanical effects due to hydrodynamic phenomena, forming complex flow “structure” behaviour. Nanocellulose containing suspensions are viscoelastic, i.e. demonstrate elastic solid-like behaviour together with viscous energy dissipating flow. Therefore it is of interest to a wide range of applications to discuss the basics of viscoelasticity in solubilised polymeric substances in dispersions, like MNFC, as they have a profound effect on bulk rheology.

Fibre suspensions have shear thinning behaviour, which depends on size and flocculation tendency of the fibres, while coating colours have a static structure followed by shear thinning to a Newtonian or nearly Newtonian region at medium shear rates, followed by further shear thickening and finally a shear thinning region at high shear rates. MNFC suspensions are typically very prone to shear thinning behaviour, which is discussed through both their fibrillar and colloidal nature.

Existence of yield stress in fibre suspensions has been studied in the literature and it was observed that though the non-coherent fibre suspension does not actually have a true yield stress, as the flocs have a higher concentration than the suspension average, creating points of greater cohesive strength than the other parts of the suspension. Some of the most frequently used yield stress models are discussed, which give most satisfying fits to the complex suspension rheograms for both fibre suspensions and coating colours.

The phase separable nature of MNFC while under typical measurement conditions regularly displays wall slip and shear banding phenomena, which affect experimental results and can be reduced by using modified surfaces on the standard rheological geometries.

The main function of thickeners is to adjust viscosity of the coating colour to the desired level and impart the necessary degree of water retention. Thickeners need to be able to interact strongly both with water molecules and with other ingredients of coating formulations, especially pigments, in order to display a thickening effect. These interactional properties are important to understand when considering partial / total substitution of standard thickeners, such as CMC, with MNFC. To obtain a uniform coating layer with good printability characteristics, it is necessary that high solids accompanied with sufficient water retention properties be controlled throughout the application and levelling process.

In the thesis we consider the combination of NFC either as a constituent part of microfibrillar cellulose (MFC) or as a blend material in its own right in standard filler containing fibrous furnish or fine pigmented coating colours. Therefore, the rheology and dewatering will reflect the level of interaction between the gel material and the other components present. As the thesis studies two types of suspension systems, namely the inclusion of MNFC in furnish, where the balance of flow properties depends on the ratio of fibrous furnish to MNFC, and in coating colours, which consist of high concentration pigment suspensions in which MNFC is considered as an additive in ratio with pigment and other polymer additives, such as CMC, the different dewatering and filtration mechanisms arising are discussed.

Application of the coating colour to the paper leads instantaneously to the onset of liquid drainage from the coating colour to the base paper, resulting in an increasing particle concentration (solid content) in the coating layer and increasing surface roughness of the base paper due to hydraulic impression. Coatings can exhibit unique flow behaviour in the blade nip and they may not have enough time to relax after the large strain deformation, such that the coating colour surface becomes affected by retention and/or inducement of elasticity. Therefore, it is important to adjust and control the rheology of the coating colour in order that during the application to the base paper the right viscosity and elasticity enable optimal filtration and water retention.

The filtration mechanisms, for both fibre suspensions and coating colours are compared to that of gel dewatering, since in the presence of MNFC the dewatering properties are controlled predominantly by gelation. Rheological observation of a sample (furnish pad or coating colour) during filter cake formation is very important, as continual removal of water alters the material flow properties, and shear stresses imposed during the process may also change the sample's rheological and dewatering responses.

From the contrasting rheological and dewatering properties of coating colours compared with furnishes, we can conclude that dispersing agents promote colloidal stability of the pigment particles and latex binders, which is a crucial effect under application shear and during the dewatering process as it affects the rheology and determines the immobilisation characteristics of the interacting components during drying.

The resulting different pore structure of coated layer when using thickeners versus MNFC affects a wide range of properties, including light scattering and printability, i.e. the interaction of the coating with applied liquids during printing.

Due to the difficulty in studying thin layers, tablet forming methods are used for modelling of the paper coating layer behaviour allowing both liquid contact and equilibrium absorption and permeation to be studied. Porosity and pore size distribution based on the model of parallel capillaries can be determined by measuring the non-wetting intrusion permeation of the structure using the technique of mercury porosimetry. Also water (polar) and hexadecane (non-polar) liquids can be used to establish the relationship between the solid phase surface energy and the surface tension of each respective liquid, and so to determine their relative absorption rates as a function of time.

In the following sections, the background to the manufacture of the fibrillar materials is considered for each size range in turn, and then the description for the background to the general rheological theories and methodology is outlined.

2.1 From cellulose to micro- and on to nanocellulose: an introduction

Cellulose is the most common organic polymer on earth, produced by biosynthesis with simple primary molecular structure, both unique in its ability for intra and intermolecular interactions and for developing structural formations of several levels of organisation, as presented in Fig.2. Cellulose is a linear homopolysaccharide consisting of β -(1,4)-D-glucopyranosyl units. The degree of polymerisation (DP) of natural cellulose may be as high as 15 000 (cotton) while typical Kraft pulp cellulose has a DP of 500 - 2 000 (O'Sullivan 1997, Klemm *et al.* 2009). The cellulose elementary fibril is joined or coated with other wood constituents, such as hemicellulose, proteins, pectin or lignin, forming a microfibril (Somerville 2004, Ding and Himmel 2006).

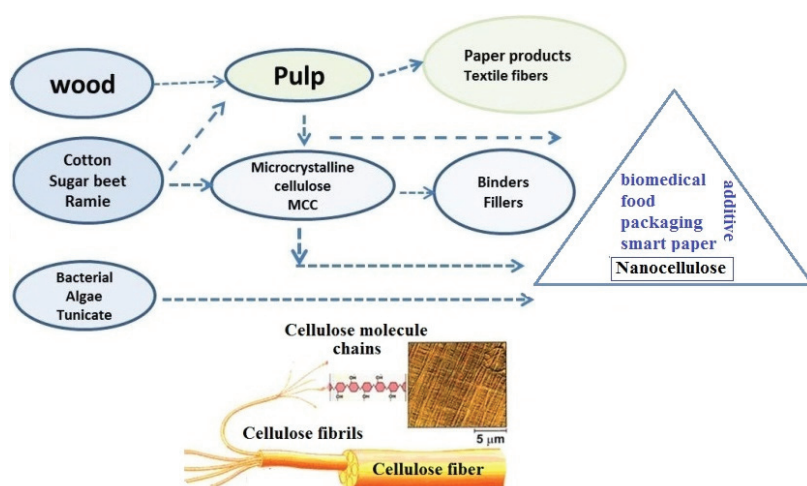


Figure 2 Traditional products from different cellulose sources and novel high performance MNFC based products / Modified from biologie.uni-hamburg.de

2.1.1 Microfibrillated cellulose MFC

MFC can be manufactured from numerous different cellulosic sources, but wood, as most abundant, is the most important industrial source, and thus main raw material for its production. The primary function of cellulose in wood is to give mechanical strength of the composite, enabled with hemicellulose and lignin which bind cellulose fibrils together, Fig. 3 (Henriksson *et al.* 2009, Siro and Plackett 2010).

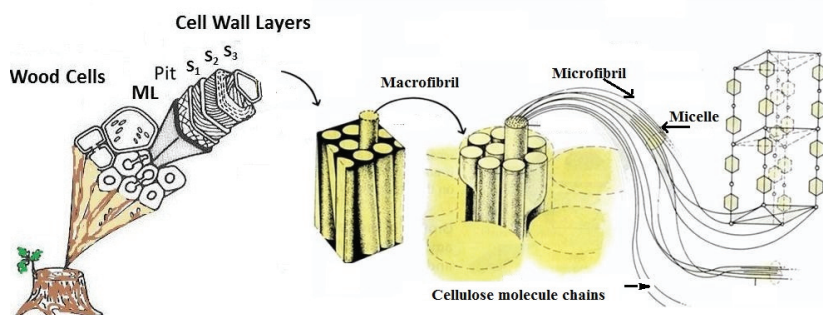


Figure 3 Schematic formations of cellulose microfibrils in wood / Modified from nickrentlab.siu.edu

In order to facilitate the disintegration of wood down to its fibrillar level, the wood material is typically first purified with a chemical pulping process. Hence, a common raw material source for wood-based MFC is bleached Kraft pulp. The first production of speciality microfibrils from wood pulp was already reported in the 1980s (Turbak *et al.* 1984), and it was obtained by disintegration of microscopic fibres through an homogenisation process, and, therefore, named by Turbak microfibrillated cellulose (MFC). The method utilised repeated passage of cellulose pulp water suspensions through a mechanical homogeniser accompanied with a high pressure drop in order to facilitate cavitation and fibrillation, with the final product consisting of long fibrils that had much higher surface area than traditional fibres. The thus produced MFC consisted of high viscosity microfibril aggregates, with a diameter ranging from 20 to even 100 nm having a length of several micrometres. The degree of fibrillation was improved by increasing the number of passes through the homogeniser, which also further increased energy consumption, damaging the microfibril structure by reducing the degree of polymerisation (DP) by up to 27 % (Turbak *et al.* 1984, Henriksson *et al.* 2007, Klemm *et al.* 2009). The method was later improved by introducing, in addition to the high pressure homogenisation, extensive shearing and an impact force (Nakagito and Yano 2004, Henriksson *et al.* 2007, Iwamoto *et al.* 2008). Frictional grinding methods developed by Abe and Mair (Abe and Mair 2005) further decreased energy consumption.

The introduction of anionically charged groups into the pulp fibres has been known to enhance delamination of the fibre wall by inducing swelling of the wall resulting in a lower cohesion prior to delamination (Walecka 1956). One of the most efficient ways to weaken and swell the fibre cell walls in the fibrillation process is to utilise enzymatic pre-treatment combined with a refining step. Very good results in terms of product uniformity

were accomplished with use of endoglucanase, which reacts with only amorphous, disordered regions (Pääkkö *et al.* 2007, Henriksson *et al.* 2007). Increasing the charge density of MFC fibrils enables charge repulsion between the fibrils which leads to a drop in the tendency to flocculate, thus decreasing viscosity and reducing clogging in the homogeniser (Horvath and Lindström 2007, Hubbe and Panczyk 2007).

2.1.2 Nanofibrillar cellulose NFC

Later, new MFC production methods, which incorporated chemical pre-treatment prior to fibrillation, resulted in both consumed energy reduction, up to 91 % (Pääkkö *et al.* 2007), and decreased aggregation, further resulting in a final product having nanoscale individual fibrils and therefore named nanofibrillar cellulose (NFC). The pre-treatment of cellulose fibres such as by selective oxidation with 2,2,6,6-tetramethyl-piperidinyl-1-oxyl (TEMPO) radical as catalyst (Saito *et al.* 2007) or the introduction of charge to fibres via carboxymethylation (CM) (Notley and Wågberg 2005) is a primary technique today allowing production of nanoscale fibrils. The carboxymethylation process involves solvent exchange from water to ethanol, impregnation with monochloroacetic acid and by adding NaOH in a mixture of methanol and isopropanol, after which only one pass through the homogeniser is sufficient for good product uniformity, with further decreased energy consumption (Klemm *et al.* 2011, Larsson *et al.* 2012, Wang *et al.* 2012, Pöhler *et al.* 2011). By introducing charged carboxylate groups on the surface of the fibre, the C6 primary hydroxyl group of cellulose is selectively converted to carboxylate groups via C6 aldehyde groups, which results in separation of nanofibrils within the fibres (Saito 2007). When the carboxylate content reaches approximately 1.5 mmol g^{-1} , the oxidised cellulose slurries are mostly converted to transparent, highly viscous dispersions, having nanofibrils 3-4 nm wide and a few micrometres long (Saito 2007). The TEMPO oxidation pre-treatments are typically followed by mechanical treatment with a double-cylinder type homogeniser or sonication (Isogai 2011).

Another way of producing NFC is to use bacteria which create a thick gel, called pellicle, that is composed of nanoscale cellulose fibrils and 97 % water (Klemm *et al.* 2009, Klemm *et al.* 2011, Yoshinaga *et al.* 1997). The difference between a bacterially synthesised cellulose network and that of NFC is that they consist of a fully joined fibril network of pure native cellulose.

Different nanocellulose pre-treatment and production methods result in products with different morphology, DP, aspect ratio, surface charge and mechanical properties, all of which affect their rheological behaviour in aqueous suspension. A simplified illustration of the different types of MNFC products derived from cellulose fibres is presented in Fig.4.

Methods to manufacture nanocellulose products

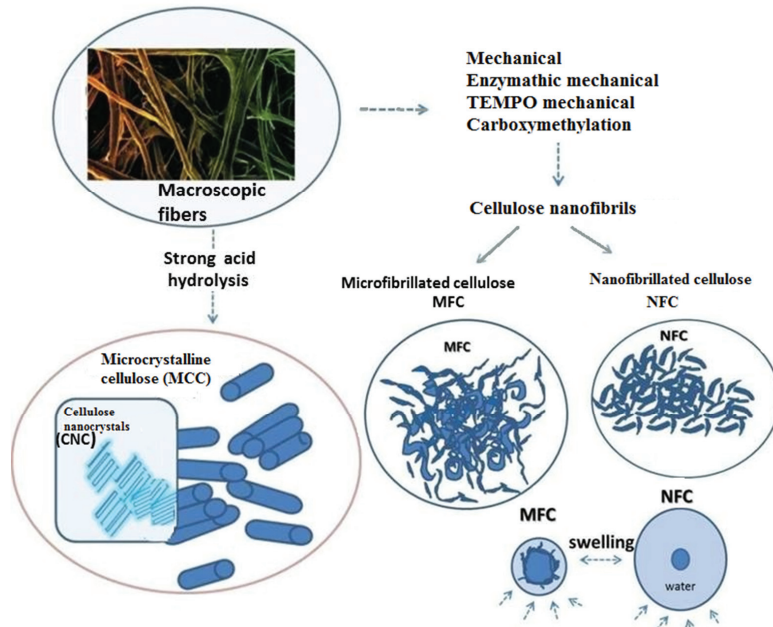


Figure 4 Preparation routes for MCC (microcrystalline cellulose), CNC (crystalline nanocellulose), MNFC (MFC/NFC) / Modified from reference (Kettunen 2013)

2.1.3 Structural and rheological properties of MFC/NFC containing suspensions

The final product properties of MNFC are greatly influenced not only by the processing method but also by the source of cellulose (Bulota 2012, Hubbe *et al.* 2008, Klemm *et al.* 2011). The small nanoparticle size results in high aspect ratio, for example microfibrils having a size of 6 nm in diameter and 1 μm length result in 2.3×10^{16} particles g^{-1} with specific surface area $431 \text{ m}^2\text{g}^{-1}$, which corresponds to 106 cellulose fibres with specific surface area of $1 \text{ m}^2\text{g}^{-1}$ as reported by Klemm *et al.* (Klemm *et al.* 2011). These properties of MNFC create a high sensitivity to physical and chemical surface activity within suspensions. The interaction forces acting between colloidal MNFC particles in suspensions or between these surfaces play an important role in implementation of these materials in variety of industrial processes. MNFC possess distinctly different properties of traditional cellulose fibres displaying very high mechanical strength, low thermal expansion, high surface area and unique optical and self-assembly characteristics (Agoda-Tandiwa *et al.* 2010, Saito *et al.* 2007, Subramanian *et al.* 2011). Rheologically, through having a strong networking tendency and large water retention capacity, MNFC suspensions are highly viscous thixotropic transparent (or semi-transparent, depending on residual fibrous material) gels at concentrations already above 1 w/w% (Herrick *et al.* 1983, Iotti *et al.* 2011, Pääkkö *et al.* 2007).

2.1.4 Surface interactions between MNFC

MNFC consist of small fibrous particles with high aspect ratio, of width in the nanometre range and length in the micrometre range, and high specific surface area properties behaving like colloidal suspensions under dilute conditions and as aqueous gels when more concentrated. Additionally, they clearly are in the size and density range to undergo Brownian motion, and exhibit rotational and translational diffusion (Tanaka 2012, Mashkour *et al.* 2013).

2.1.4.1 DLVO forces in MNFC suspensions

Most surfaces, including cellulosic substrates such as MNFC, are charged when in contact with water, which results in formation of an electrical double layer consisting of attracted secondary charge. The DLVO theory (Derjaguin 1941, Verwey *et al.* 1999) is often used to describe the combined interaction forces arising from van der Waals short range attraction and electrostatic repulsion of similarly charged particles, Fig. 5 (Hamaker 1937). The interaction energy between two particle surfaces is a function of the distance between particles. The apparent swelling of MNFC by the adsorption of interfibrillar immobilised water adds to the steric repulsion, acting similarly to swollen polymer (Israelachvili and Wennerström 1996). Different measurement methods, especially the surface force apparatus (SFA) and atomic force microscopy (AFM), have been widely used to study surface forces (Ducker *et al.* 1991, Hodges 2002, Milling *et al.* 1996).

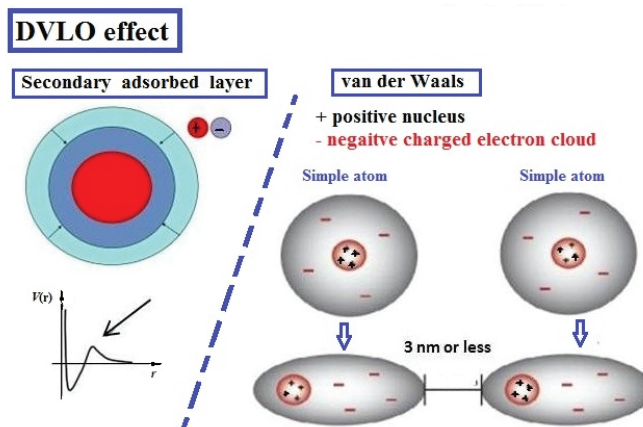


Figure 5 DLVO effect: combined electrostatic forces and steric repulsion in MNFC suspension acting versus van der Waals forces / Modified from Gane *et al.* 2009

2.1.4.2 Electrostatic double layer forces, zeta potential

In many paper making colloidal suspensions, a major contribution to the DLVO overall interaction potential comes from the electrostatic double layer forces, which are present between charged surfaces manifest in polar liquid (Israelachvili 2011). In the presence of an electrolyte at sufficient ionic concentration, the surface charge is balanced by

oppositely charged counter-ions leading to system electroneutrality. The region near the surface of the region of increased counter-ion concentration is called the electrical double layer, and ions close to the charged surface are strongly bound to the immobile, so-called Stern layer. The region adjacent to the Stern layer is called the diffuse layer and contains loosely associated ions that are relatively mobile, Fig.6.

MNFC surface charge, expressed as zeta potential (ζ), has an important effect, derived from carboxyl charge density distribution, in determining the amount of bound water on the particle expressed as the repulsion and interaction between MNFC and water molecules which is important to be discussed in relation to mobility within suspensions. Zeta potential (ζ) is frequently measured in respect to the electrokinetic potential of the colloid system defined as the potential difference between the dispersion medium and the stationary layer of surrounding liquid immobilised with the colloidal particulates, at the outer plane between the immobilised and free liquid phase of the bulk fluid. The level of ζ effects either, agglomeration if low or repulsion if high, between the particles in suspension, thus affecting their dispersion stability (Horwath and Lindström 2007). Differences in production route and different pre-treatments of the MNFC result in different amounts and availability of reactive carboxyl groups, which affect its surface charge (ψ), and thus zeta potential (ζ) of the particles or agglomerates in aqueous suspension (Wågberg *et al.* 2008, Fall *et al.* 2011), as presented in Fig. 6.

Various mathematical models using DVLO theory have been developed using parameters such as the number and density distribution of charged groups on the MNFC to predict surface charge density, and these models are used to predict aggregation as a function of surface charge and double layer thickness in response to pH (Wågberg *et al.* 2008, Tanaka and Fall 2011). In the case of MNFC, ζ is thus strongly related to the amount of bound water on the surface of the nanofibre, which additionally contributes to a steric barrier and thus lubrication between the MNFC particles.

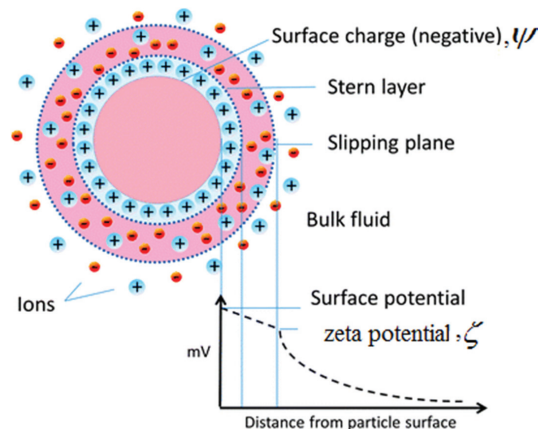


Figure 6 Zeta potential, ζ , and surface charge, ψ , of a particle or agglomerate as a function of distance from the surface / Adopted from reference (Liese and Hilterhaus 2013).

2.1.5 Bound water on surface of MNFC

In swelling, cellulose fibre and water molecules change position up to a limited value with an increase in fibre diameter (Lindström and Carlsson 1982, Maloney *et al.* 1990, Öztürk *et al.* 2009) while in dissolution this leads to breakage of intermolecular bonds (Hatakeyama *et al.* 2012, Mazza *et al.* 2009, Weise *et al.* 1996). The pre-treatment methods determine the swelling (water adsorption and interstitial uptake) and fractionation mechanisms of both macroscopic cellulose fibres and MNFC (Jaturapiree *et al.* 2008, Luukko and Maloney *et al.* 1999).

Exposure to water leads to a transformation of the higher order structure of cellulose fibres through diffusion of water into amorphous and intermediate regions of cellulose, as water molecules induce breakage of intra and inter cellulose hydrogen bonds acting between hydroxyl groups of cellulose molecules (Kimura *et al.* 1972, Nakamura *et al.* 1981, Hatakeyama *et al.* 2004, Hatakeyama *et al.* 2012). This process results in structural change in both cellulose and the orientation of water molecules, and the various different structures of water molecules within the cellulose fibres can be used for their identification via a variety of different experimental studies (Kimura *et al.* 1972, Hatakeyama *et al.* 1988, Nakagito 2004).

Similarly, using differential scanning calorimetry (DSC) different states of bound water with different phase transition properties can be categorised (Nakamura *et al.* 1981, Yoshida *et al.* 1992). Hatakeyama (Hatakeyama *et al.* 2012) defines three “types” of water that can be found with the DSC, used also by other researchers (Manninen *et al.* 2013, Luukkonen *et al.* 2001). These are, respectively, free water (W_f), which freezes at the same temperature as the bulk water, non-freezing water (W_{nf}), which can be detected only by thermal analysis, has no peak of freezing or melting, while less associated water fractions exhibit smaller melting enthalpy (ΔH_{ml}) than the bulk water and are referred to as freezing bound water (W_{fb}). Same authors define the water content fraction of an MNFC suspension (Hatakeyama *et al.* 2012) as

$$W_c = \frac{m_w}{m_c + m_w} \quad (1)$$

where m_c is the mass of dry cellulose sample and m_w the mass of water in the system. From above, the water content fraction (W_c) is given as

$$W_c = W_f + W_b \quad (2)$$

The bound fraction water content W_b on polymer, i.e. on the MNFC surface, is the sum of freezing bound water and non-freezing bound water fractions (Hatakeyama *et al.* 2012).

$$W_b = W_{nf} + W_{fb} \quad (3)$$

The non-freezing fraction W_{nf} is then calculated as

$$W_{nf} = \frac{m_w}{m_c + m_w} - W_f - W_b \quad (4)$$

and both non-freezing (W_{nf}) and freezing bound water (W_{fb}) for NFC are much larger than that for MFC, as presented in Fig. 7.

The same research showed that the fraction of non-freezing water W_{nf} is much higher for NFC than for MFC, explained as being related to the smaller size of NFC, and therefore the larger amount of hydroxyl groups coming in contact with individual water molecules.

The diameter of apparent swelling radius, therefore, is found to depend on the zeta potential of the nanocellulose, and includes all the forms of water present, with the increase in diameter being correlated to the initially high zeta potential. As a result of the amount of bound water, the zeta potential of the particle subsequently decreases, Fig. 7 (Israelachvili 2011, Uetani and Yano 2011).

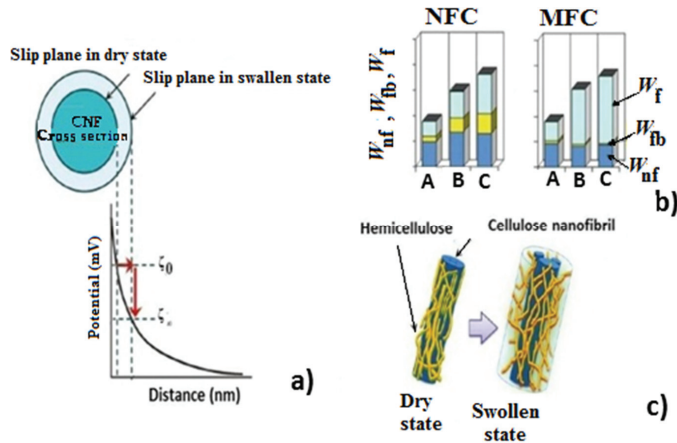


Figure 7 a) Swelling radius of MNFC, expressed as amount of bound water, depends on zeta potential, and can be determined through DSC /Adopted from reference (Uetani and Yano 2011)/, b) comparison of non-freezing water (W_{nf}), freezing bound water (W_{fb}) and free water (W_f) in the interaction with NFC and MFC at the three different water contents W_c (=mass of water/mass of dry sample) A, B, and C respectively ; $W_c(A) = 0.55$, $W_c(B) = 0.90$, and $W_c(C) = 1.10$, Eq.1 / Adopted from reference (Hatakeyama et al.2013) /, and c) schematic representation of cellulose nanofiber swelling model/ Adopted from reference (Uetani and Yano 2011)/.

2.2 Viscoelasticity

2.2.1 Microstructure affects viscoelastic behaviour of complex suspensions

Association of particles and/or interphase association, such as between particles or polymers and bound water, or strong repulsion at high solids content, related to particle-particle, particle-polymer and particle-water interactions induces formation of an internal structural three-dimensional network in aqueous suspension (Russel 1980). Solid particles and polymers dispersed into a liquid phase provide the largest component effects in materials that show deviation from a Newtonian behaviour and become non-Newtonian fluids. Paper making suspensions fall into the group of non-Newtonian materials, e.g. coating colour suspensions, fibre suspensions and, of main interest here, nanocellulosic colloids (Aidun and Triantafillopoulos 1997, Triantafillopoulos 1985).

Bulk rheological properties of complex suspensions depend on the net potential energy manifested by the many of secondary forces (electrostatic, van der Waals, steric or solvation) and mechanical effects due to hydrodynamic phenomena, forming complex flow “structure” behaviour (Kwong *et al.* 1993, Tsai and Zemmouri 1988).

An important parameter affecting bulk rheology is the state of the particle flocculation and aggregation in a flow. Internal structure breaking competes with structure forming due to increased frequency of collisions between particles under shear (Gane *et al.* 1992, McGenity *et al.* 1992, Zhang and Archer 2002).

2.2.1.1 Viscoelasticity of non-Newtonian fluids

Viscoelasticity expresses the combination of solid-like elastic behaviour together with viscous flow. These two components of material properties can be described using an orthogonal two dimensional parametric description, consisting of the elastic component which remains in phase with the any physical distortion and stores energy, and a viscous component which lags the distortion and acts to dissipate energy. The treatment of this 2D parameter space forms the equivalent of the vector components resulting in the total viscoelastic result. One way of expressing the manipulation of components acting out of phase is to represent the vector space defined above as an Argand diagram with each component plotted orthogonally (Mezger 2006), Fig.9. For purely viscous fluids under shear, the viscous stress (τ_v) expressed in the flowing liquid is dependent on the strain rate $\dot{\gamma}$ via the constant of proportionality, i.e. viscosity (η) (Astarita and Marrucci 1974, Mezger 2006)

$$\tau_v = \eta \frac{d\gamma}{dt} = \eta \dot{\gamma} \quad (5)$$

In contrast to purely viscous materials, viscoelastic substances exhibit a combination of viscous and elastic behaviour, for which Hooke’s law of linearity between strain γ applied and elastic stress τ_e experienced holds true, i.e. stress is proportional to strain,

$$\tau_e = k_e \gamma \quad (6)$$

where k_e refers to the elastic constant of the system.

Combining Eqs. 5 and 6 gives the expression

$$\tau = \tau_e + \tau_v = \left| \eta^* \right| \dot{\gamma} \quad (7)$$

where $\left| \eta^* \right|$ expresses the magnitude of the complex viscosity, on incorporating both the elastic and viscous effects, which will be discussed in more detail below.

2.2.1.2 Oscillatory Shear Rheology

In addition to deformation rate-dependent viscosity, shear history affects the expressed rheology of non-Newtonian fluids as they have the ability to “remember” previous flow history. Solubilised polymeric substances in dispersions, like natural or synthetic polymers in coating colours and colloids, such as nanocellulose, have a profound effect on bulk rheology, and this information can be obtained via designed viscoelastic measurements (Mezger 2006, Kugge 2003).

Deformation strain, γ , applied to a sample between two moving surfaces is a function of alignment or deformation between the layer of liquid suspension Δx and the gap between the plates y , Fig. 8, and expressed in Eq. 8 (Kugge 2003, Mezger 2006).

$$\gamma = \Delta x / y = \tan \delta \quad (8)$$

It is assumed that at phase angle $\delta = 45^\circ$, when $\Delta x = y$, strain γ is 100 %. A strain-controlled rheometer applies an oscillating strain $\gamma(t)$ and measures the produced stress $\tau(t)$.

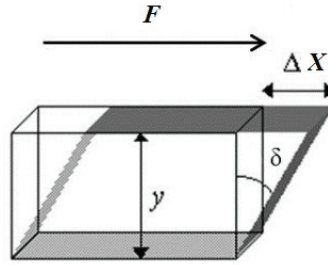


Figure 8 Deformation of a sample between two parallel boundaries

In oscillatory shear rheometry the moving part of the measuring geometry (plate or cone in this case of radius r), oscillates with respect to the stationary boundary (another opposing plate in this case) and creates small vibrations transferred throughout the parallel geometry gap. Thus, feedback from the sample deformation vibration to the rheometer gives information of the viscoelastic properties of the sample (Kugge 2003, Mezger 2006, Coussot 2005). In a controlled stress rheometer, the stress feedback is used to control the applied strain such that stress is maintained at the desired level. In contrast to continuous rotational tests, oscillatory measurement for the variable separable analysis of viscoelasticity is performed when the sample is within the linear viscoelastic range (LVE), and therefore the supramolecular structure, i.e. the elastically interacting structure between particles, polymers etc., is not destroyed during testing.

There are two main measuring technologies in oscillation measurements, the amplitude or strain sweep, and frequency sweep (Mezger 2006, Kugge 2003, Coussot 2005). The amplitude sweep applies increasing strain amplitude γ while angular frequency ω is kept constant, while a frequency sweep measurement applies increasing angular frequency (ω) while γ is held constant, as presented in Fig. 9. An oscillatory test simultaneously determines both the viscous and elastic nature of the material. As presented in Fig.9 the transmitted strain lags behind the induced stress by phase angle δ .

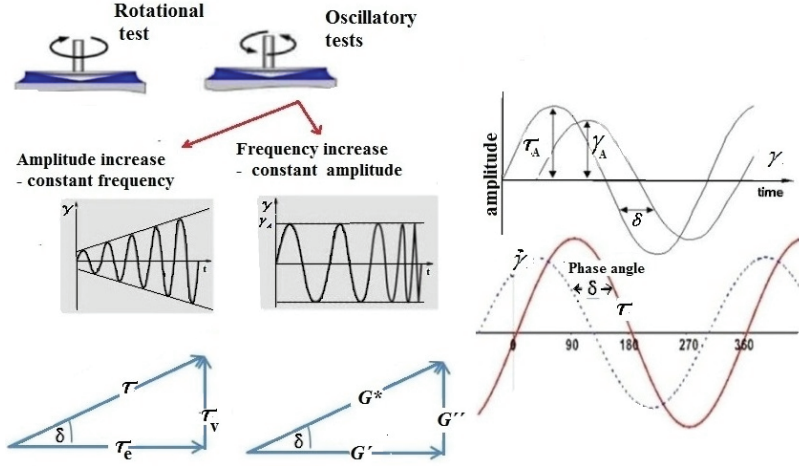


Figure 9 Oscillatory test and viscoelastic parameters / Modified from reference (Mezger 2006)

The complex shear modulus G^* presented in Fig. 9 is a sinusoidal function, and so can be broken down into its orthogonal components, the elastic storage shear modulus G' , given by Hooke's law, and the loss shear modulus G'' , representing the viscous behaviour

$$G^* = G' + iG'' \quad (9)$$

where $i = \sqrt{-1}$ and $|G^*| = \sqrt{(G'^2 + G''^2)}$, once again, indicates the absolute or scalar magnitude of the complex number. Therefore, G' and G'' can also be expressed as functions of the initial amplitude of stress τ_A and deformation γ_A and phase angle δ , as

$$G' = \frac{\tau_A}{\gamma_A} \cos \delta \quad (10)$$

and

$$G'' = \frac{\tau_A}{\gamma_A} \sin \delta \quad (11)$$

where G' is in phase with the transmitted strain amplitude and G'' is 90° out of phase (Astarita and Marrucci 1974, Mezger 2006).

The variable separable orthogonal elastic (G') and loss (G'') moduli and their proportion describe the viscoelastic nature of the material. For $G' > G''$ the material is predominantly elastic, and if $G' < G''$ the material is predominantly viscous. This is often expressed in terms of the phase angle δ , which expresses the lag between the transmitted strain and the suffered stress, given as loss factor:

$$\frac{G''}{G'} = \tan \delta \quad (12)$$

2.2.1.3 Oscillatory measurements – linear viscoelastic region

An amplitude sweep oscillatory measurement indicates the degree of stability of a material and it is a standard procedure to first perform an amplitude sweep to determine the location and extent of the linear viscoelastic region LVE in material, which ends at a critical strain γ_c . At this point G' decreases, while the change in G'' cannot be seen. Only after the determination of γ_c with amplitude sweep test, is the frequency sweep test performed.

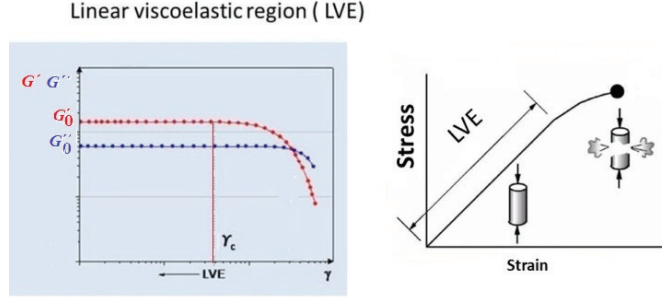


Figure 10 Oscillatory shear amplitude sweep measurement with elastic (G') and loss (G'') moduli as a function of strain (γ) in the linear viscoelastic region (LVE); critical strain (γ_c) as the point where $G' \approx 95\% G_0'$, where G_0' is the initial value of G' /Modified from WEE-Sollve GmbH.

2.2.1.4 Dynamic and complex viscosity

While for a Newtonian fluid, viscosity η is a function only of temperature T and stress τ , and depends linearly with the applied shear rate $\dot{\gamma}$ (Eq. 5), in the case of a shear-thinning non-Newtonian fluid η is also a function of shear rate $\dot{\gamma}$, as is described by

$$\eta(T, \dot{\gamma}) = \frac{\tau}{\dot{\gamma}} \quad (13)$$

In the oscillatory test, the viscosity is described as the complex viscosity η^* within LVE region from Eq. 7 as

$$|\eta^*| = \frac{\tau(t)}{\dot{\gamma}(t)} \quad (14)$$

where $|\eta^*|$ is the magnitude of the complex viscosity having the components of the real part of complex viscosity η' and the imaginary part of complex viscosity η''

$$|\eta^*| = \sqrt{\eta'^2 + \eta''^2} \quad (15)$$

where $\eta' = \frac{G''}{\omega}$ and the imaginary part of the complex viscosity $\eta'' = \frac{G'}{\omega}$ are out of phase, again yielding the loss factor (Astarita and Marrucci 1974, Mezger 2006)

$$\tan \delta = \frac{\eta'}{\eta''} \quad (16)$$

For the purpose of this thesis we will just define a few deformation models of viscoelastic materials which are irreversible processes in which the sample changes its form during the process.

2.2.1.5 Principle of Cox-Merz rule

The so-called Cox-Merz rule is an empirical relationship which has been found to be of great use in rheology, as it is an experimentally applied rule used for many polymeric systems, in which correspondence occurred between η plotted against $\dot{\gamma}$, (from controlled stress (CSR) measurements outside the LVE) and the magnitude of η^* plotted against ω (Cox and Merz 1958, Doraiswamy *et al.* 1991, Marrucci 1996). It is important for the rule to be applied that flow conditions are not in a transient mode, which is very difficult to avoid in the case of MNFC based suspensions, for the reason which will be explained further on. The Cox-Merz rule has its main use in polymer rheology, as it is valuable when $\eta(\dot{\gamma})$ can be predicted from oscillatory shear measurements when measurements of steady state viscosity are difficult at high shear rates, due to, for example, sample fracture or other unevenness of shear profile within the sample, which causes secondary flows. Also, the rule can be used to predict $\eta^*(\omega)$ from steady state viscosity data in circumstances in which the oscillatory operating mode is not available (Adams 1993, Al-Hadithi *et al.* 1992). In this thesis the Cox-Merz rule is used to test if the behaviour of coating colours that have MNFC as partial substitution of CMC is polymer-like or more similar to a suspension of hard particulates.

2.2.2 Flow phenomena of non-Newtonian fluids

As mentioned above, after critical strain, beyond the LVE when the elastic structure begins to be broke down as strain increases, the hydrocolloid suspensions exhibit non-Newtonian behaviour where their viscosity depends on the shear strain rate, Fig. 11. For such fluids, the slope of the shear stress against shear rate curve is therefore not constant as the shear rate changes. When the viscosity decreases with increasing shear rate, the fluid is termed *shear thinning* (defined as pseudoplastic), while in the opposite case, where the viscosity increases as the fluid is subjected to a higher shear rate, the fluid is called *shear thickening*. *Shear thickening-dilatancy* is isothermal and refers to viscosity increase as a function of shear rate. This behaviour can be induced by increase in particle concentration, during dewatering and shear induced aggregation, and also due to disorder of particle alignment due to the flow velocity gradient, giving effects such as the shear blocking characteristic of highly concentrated suspensions (Coussot 2005, Feng *et al.* 2007).

Many shear- thinning fluids exhibit Newtonian behaviour once very high shear rates are applied, Fig.11 a),

$$\eta_0 = \lim_{\dot{\gamma} \rightarrow 0} \eta(\dot{\gamma}) \quad \text{and} \quad \eta_\infty = \lim_{\dot{\gamma} \rightarrow \infty} \eta(\dot{\gamma}) \quad (17)$$

The regions where the apparent viscosity is approximately constant as a function of shear rate are known as Newtonian regions.

Frequently, shear thinning or shear thickening regions can be approximated by a straight line on a double logarithmic (log-log) plot, Fig.11, as follows

$$\log \eta = a + b \ln \dot{\gamma}, \quad \text{or} \quad \eta = k \dot{\gamma}^b \quad (18)$$

Flow coefficient is $k = e^a$, and instead of b can be used $(n-1)$ to express this form of power law exponent. Parameters k and n are then two empirical curve fitting parameters, known as fluid consistency coefficient, k , and the flow behaviour index, n , respectively (Chhabra and Richardson 2008, Mezger 2008). The power law is the simplest representation of shear thinning/thickening behaviour and applies only over a limited range of shear, and fails in predicting zero (η_0) and infinite shear viscosities (η_∞). From the power law part of the flow curve an expression of the following form is applicable (Chhabra and Richardson 2008):

$$\tau = k \dot{\gamma}^n, \quad \eta = k \dot{\gamma}^{n-1} \quad (19)$$

The exponent n in Eq. 19 gives the degree of thinning/thickening:

$n < 1$, the fluid is exhibiting shear –thinning properties

$n = 1$, the fluid shows Newtonian behaviour

$n > 1$, the fluid shows shear –thickening behaviour.

When there are significant deviations from the power law model at very high and very low shear rates, Fig.11, it is necessary to use the model which takes into account the values of the start and equilibrium end viscosities η_0 and η_∞ , respectively, and by the Carreau-model function (Carreau *et al.* 1979, Chhabra and Richardson 2011) one can represent the viscosity profile by:

$$\frac{\eta - \eta_\infty}{\eta_0 - \eta_\infty} = \left(1 + \left(c_c \dot{\gamma} \right)^2 \right)^{(n-1)/2} \quad (20)$$

where η_0 and η_∞ are the viscosities at zero and infinite shear rate, respectively, presented in Eq.17 and c_c is a shear-dependent time constant, named “cross exponent” that represents the reciprocal of the shear rate required to halve the viscosity η .

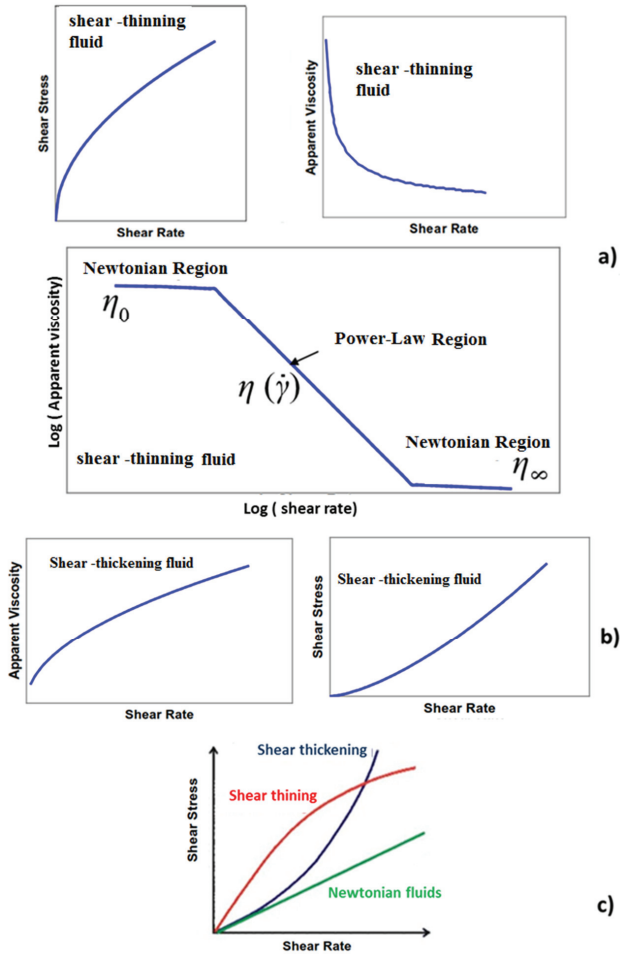


Figure 11 a) Shear thinning fluids: log-log diagram of dynamic viscosity (η) as a function of shear rate ($\dot{\gamma}$) according to non-Newtonian power-law b) shear-thickening fluid /Modified from Subramanian Shakar, Clarkson University/, c) compared with Newtonian and dilatant fluids /Modified from Prof. Martin Chaplin, London South Bank University/

2.2.2.1 Paper making suspensions as non-Newtonian liquids

Fibre suspensions have shear thinning behaviour, which depends on size and flocculation tendency of the fibres, (Barnes and Nguyen 2011, Bousfield 2008, Derakhshandeh *et al.* 2011) while coating colours have a static structure followed by shear thinning to a Newtonian or nearly Newtonian region at medium shear rates, followed by further shear thickening and finally a shear thinning region at high shear rates (10^6 s^{-1}) (Husband 1998, McGenity *et al.* 1992, Triantafillopoulos 1985). Similarly, MNFC suspensions are typically very prone to shear thinning behaviour, which is a result of their both fibrillar

and colloidal nature, and for these materials the simple shear thinning models are not fully applicable (Lotti *et al.* 2011, Ovarlez *et al.* 2009, Puisto *et al.* 2012).

Some of the rheological properties that are common for complex non-Newtonian fluids can be coexisting with shear thinning and shear thickening parts of the rheological curves of papermaking suspensions, depending on the consistency, shear rate and the interacting surface forces within the structure:

Thixotropy is a complex time dependent behaviour of fluids which have variable viscosity reversibly decreasing with time under constant shear stress or shear rate under high shear rates. Due to the time dependent reversibility, the viscosity of thixotropic fluids increases over time at low or zero shear rates, i.e. viscosity builds when stationary. When sheared, the structure is broken down and viscosity decreases under constant shear stress or shear rate, followed by a gradual recovery, while at rest the microstructure slowly rebuilds itself resulting in an increase of viscosity (Coussot 2002, Dullaert and Mewis 2006, Ragouilliaux *et al.* 2007). A relation between viscosity and microstructure of thixotropic fluids can be seen from “structural hysteresis” when, due to certain shear history, the very same thixotropic fluid can exhibit hysteresis during measurement, i.e. can have the same viscosity at a different shear rate, and so not the previously probed structure at the same shear rate (Coussot 2005, Dullaert and Mewis 2006, Møller *et al.* 2006).

Rheopexy is reversible viscosity increase as a function of time, under constant shear stress or shear rate and occurs commonly at low shear rate (Coussot 2005). It is a manifestation of internal structure forming due to increased collision frequency between particles under shear. Rheopexy is common in flow curves of suspensions like hydrocolloids, where dominant gel-structure resists flow at low shear rates, but viscosity decreases at higher shear rate, when structure is destroyed.

Aging is seen as an irreversible increase of viscosity with time for thixotropic fluids, as a result of build-up of colloidal gel, as, during the experiment, viscosity increase slowly progresses with time and at the end becomes too large to be measured by the rheometer (Møller *et al.* 2006). Aging is a dominating process only when the flow rate is small enough to prevent break down of a colloidal gel and therefore it is important to control the history of the sample by applying sufficient pre-shearing (Møller *et al.* 2006, Coussot 2005).

2.2.2.2 Transient effects, steady state viscosity and transient viscosity

Due to the complex behaviour of multi-component suspension systems, steady state viscosity (η), expressed as plateau (equilibrium) viscosity at given shear rate, is difficult to obtain due to the abovementioned phenomena, as the layers near the moving measuring boundary interface geometry are moving with the same speed as boundary, and it takes a certain period of time until all layers, right down to the immobile lower plate (or vessel cylinder in Couette geometry) also begin to move and reach the same viscosity. When shear rate becomes constant through the whole shear gap, it is then possible to determine $\eta(\dot{\gamma})$ (Barnes 1989, Divoux *et al.* 2013). Until this equilibrium point is reached only partly flowing material is measured, and this condition delivers a transient viscosity $\eta^+(\dot{\gamma}, t)$ (Ghosh *et al.* 1997). When measuring high viscosity samples, which are tested at very low shear rates ($\dot{\gamma} < 1 \text{ s}^{-1}$), it is important to ensure that the measuring duration is long

enough in order to observe time-dependent transition effects which occur at the start of the flow curves, if not, then $\eta^+(\dot{\gamma}, t)$ is recorded instead of $\eta(\dot{\gamma})$ (Coussot 2005).

2.2.2.3 Structure recovery measurements

A key characteristic of the response of a viscoelastic material to deformation is its ability to recover after cessation of the force which causes deformation. These measurements can be performed as *recovery of structure* prior to measurement (after pre-shearing) and during the measurements as the response to a shear ramp (Deka and Dey 2012, Mezger 2006).

Relaxation after a change of shear rate is related to memory effects, and is observable in experiments at which a complex fluid is subjected to a time dependent low shear rate. The stress relaxation time after shear cessation is identified as the time at which the suspension reaches its plateau/recovered equilibrium (Carreau *et al.* 1979, Coussot 2005, Mezger 2006).

Another type of structure recovery measurement is the Three Interval Time Test (3ITT) (Mezger 2006, Lauger *et al.* 2002, Deka and Dey 2012) which can be applied to both viscosity and elasticity recovery tests. In viscosity recovery, the 3ITT test measurement is divided into three different sections in order to examine the time dependent structure break and its recovery. The first section of the test simulates the state before a sample is processed, applying a low shear, and the second section simulates the high shear rate, thus representing, for example, the application process, and the last section, a low shear rate once again describing viscosity recovery after the application. In oscillatory 3ITT tests, the first section is performed as an oscillatory test with small deformations within LVE regions, and structure elasticity is observed through change of G' , while in the second section (load) a high shear dynamic rotation mode is used, as in the dynamic CSR test, applied outside the LVE where the structure breaks. In the last section (structure recovery) an oscillation is performed with the same oscillatory parameters as in the first section, giving information about the recovery of the elasticity as change of G' . Determination of structure regeneration as a measure of thixotropicity is expressed as the time period in the third phase over which the G' value, or η , has increased after the beginning of the regeneration phase to 75 % or 90 % of the reference start value (Mezger 2006, Deka and Dey 2012).

2.2.2.4 Determination of apparent yield point – yield stress

An ideal plastic material behaves like an elastic solid until a critical strain is applied, after which it flows and becomes fluid-like (Astarita and Marrucci 1974). The critical stress response is termed the yield stress (τ_0), and is defined as the minimum stress experienced by a material at the initiation of flow (Barnes and Nguyen 2001, Barnes *et al.* 1989, Shih *et al.* 1999, Walls *et al.* 2003). Many authors express difficulties in obtaining a standard definition of yield point using experimental methodology, due to differences in results obtained with different geometries (Barnes 2007, Møller *et al.* 2006). Basically, the issue is both mathematical and philosophical (Astarita 1990, Evans 1992). The “initiation” of flow is a discontinuity, and therefore the yield point is termed an apparent value (Mezger 2006, Coussot 2005) as for most materials, deformation below the τ_0 is a combination of elastic stress and viscous flow. Most materials with an apparent yield stress have infinite viscosity if measured at low stress (Barnes 2007, Møller *et al.* 2006). The traditional method for determining the apparent yield stress on a rotational rheometer or viscometer is to fit models to the measured rheograms, and extrapolate fitted curves to zero shear rates. There are just a few frequently used yield stress models, which can fit such types of complex suspension rheograms.

2.2.2.5 Models for yield stress determination by extrapolation

Experimentally, the yield point in steady shear mode can be obtained from rheograms collected by constantly increasing applied shear to generate stress as a function of $\dot{\gamma}$, Fig. 12a). Conversely, a stress growth test involves determination of the yield point first by application of a constantly increasing strain ($\gamma = \dot{\gamma}t$ for $\dot{\gamma} = \text{constant}$) and monitoring the stress build-up with time Fig. 12a) (Barnes *et al.* 1989, Baslingappa Swami *et al.* 2004, Coussot 2005, Mezger 2006).

There are different ways of interpreting a yield point from oscillatory measurements, specifically amplitude sweep, which are within the LVE region, as shown in Fig. 12b). One of the methods is applying an increasing oscillatory stress or strain and monitoring the responding changes in the G' , τ^s and η^* with the increasing amplitude, as presented by Derakhshandeh *et al.* (Derakhshandeh *et al.* 2011). Another is tangent analysis, with a single tangent applied to the linear region of the G' , τ^s or η^* curve, or the two tangents cross point. Corresponding strain value of that point is taken as critical strain γ_c . Static yield stress, τ_0^s can be obtained by calculating the product of the G' in the LVE and the γ_c

$$\tau_0^s = G' \gamma_c \quad (21)$$

The *Bingham* model (Bingham 1922) describes the behaviour of concentrated suspensions of solid particles outside the LVE region, assuming a transition to Newtonian behaviour, and is expressed as

$$\tau^d = \tau_{0(B)}^d + \eta_B \dot{\gamma} \quad (22)$$

where η_B is the Bingham viscosity (or plastic viscosity) representing the Newtonian part of the curve.

The Casson-model (Dzuy and Boger 1983) is an alternative model to the Bingham, with the same components raised to the power of 0.5, and has a more gradual relation to shear rate after the yield point

$$\sqrt{\tau^d} = \sqrt{\tau_{0(C)}^d} + \sqrt{\eta_C \dot{\gamma}} \quad (23)$$

where η_C is the Casson viscosity, which relates to the high shear rate viscosity.

The *Herschel-Bulkley* model describes non-Newtonian behaviour after yielding as a power law, similar to Eq. 20, presented previously for the shear thinning case, but now with a yield stress term

$$\tau^d = \tau_{0(H)}^d + K \dot{\gamma}^n \quad (24)$$

There are additional models, not used in this thesis, which can be applied to estimate yield stress or the critical shear stress for materials that have a zero shear viscosity, such as that of Ellis (or Cross) (Mezger 2006)

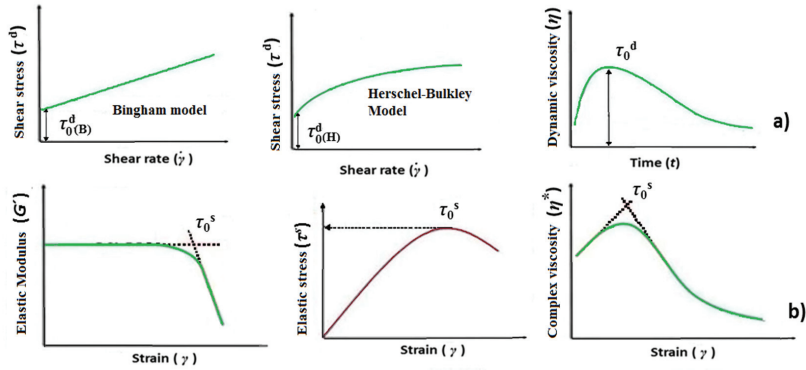


Figure 12 Determination of yield point: a) dynamic yield point determination from rotational measurements (outside LVE)(τ_0^d) and b) static yield point determination from oscillation measurements(τ_0^s) / Modified from Malvern.com/.

2.2.2.6 The practical problems with the yield stress

The various test methods for determining apparent yield stress (τ_0^d, τ_0^s) by curve fitting are dependent on the measurement geometry and the detailed experimental protocol (Barnes 2007, Coussot 2005). It is usual practice in complex yield fluids to compare both static yield point (τ_0^s), within the LVE region (Horwath and Lindström 2007, Swerin *et al.* 1992) and the dynamic yield point (τ_0^d), from the steady state dynamic shear measurements (Eq. 29) (Doraiswamy *et al.* 1991, Derakhshandeh *et al.* 2011).

One of the fundamental problems in yield stress determination is shear localisation, as below a critical shear rate $\dot{\gamma}_c$, flow is often localised in a region close to the shearing

geometry boundary and only after increase in shear rate, to that of $\dot{\gamma} > \dot{\gamma}_c$, does the sheared region transmit through the whole sample. For thixotropic material, after reaching $\dot{\gamma}_c$ the whole material is flowing, and thixotropy leads to a decrease in $\eta(\dot{\gamma})$ with an avalanche effect (Coussot 2005, Dullaert and Mewis 2006, Møller *et al.* 2006).

2.2.3 Fibre suspensions

The large aspect ratio of cellulose wood fibres (40 to 100), its flexibility and irregular shape strongly impact the behaviour of single fibre in suspension. Fibre suspensions exhibit a multitude of interactional properties, including fibre-fibre flocculation, entanglement, swelling, as well as the permutations of interactions with additive polymers and fillers. Normal forces that are built into the fibre network arise from mechanical surface linking and elastic fibre banding, and act to promote the generation of frictional forces arising from the relative movement of the fibre sides (Shmid *et al.* 2000, Zaucher and Klingberg 2001). Forces influencing the network strength, in addition to friction forces, arise from the action of chemical flocculants, hooking of curved fibres, and surface tension forces as usually there is air present in fibre suspensions (Björkman 2003, Kerekes *et al.* 1985). Hence, the change in bulk charge on the cell wall affect swelling properties on the cell wall, and thus fibre flexibility, related to the rate of beating, fibre network strength, and finally strength properties of paper sheet (Beghella and Lindström 1998, Beghella and Eklund 1999, Hubbe 2007, Laine *et al.* 2000).

Flocculation of fibre suspensions is frequently enumerated via the model of coagulation of colloidal systems (Lindström 1985, Horwath and Lindström 2007) which was first explained by Smoluchowski (Smoluchowski 1912), and later connected with other forces, although flocculation is frequently also present as a result of polymer bridging, especially in the presence of filler retention aid (Ovender and Xiao 2002, Wågberg and Lindström 1987). A more detailed history of fibre flow research can be found in the works of Björkman (Björkman 2008a, Björkman 2008b).

As discussed, increase in solids content (consistency) of fibre suspension changes the nature of contacts from occasional collisions to that of forced contacts, and further to continuous contact, described by a crowding number, N , defined as the number of fibres in a given volume in relation to the dimensions of a single fibre (Kerekes and Schell 1992)

$$N = \frac{2}{3} C_v \left(\frac{L}{d} \right)^2 \approx 5 C_m \frac{L^2}{w} \quad (25)$$

This parameter is expressed in terms of a volumetric concentration C_v , fibre length L , and diameter d . C_m is the mass consistency (w/w %), and w is the fibre coarseness. For $N > 60$ the suspension is considered to be highly networked (each fibre having at least three contact point per fibre), while the fibre network starts to fall apart for $N < 16$, as suspension are diluted (Kerekes 1985, Kerekes and Schell 1992). Therefore, in commercial papermaking, pulp suspensions are formed into paper by filtration in the range $16 < N < 60$, to minimise both water usage and formation damaging flocculation (Celzard *et al.* 2009, Derakhshandeh *et al.* 2011).

2.2.3.1 Rheology of fibre suspensions

Different approaches have been proposed to describe the dependence of viscosity on fibre flows (Bobkowicz and Gauvin 1965, Boger *et al.* 1990, Brecht and Heller 1950, Pabst *et al.* 2006, Petrie 1999, Björkman 2008a), and primarily attempting to resolve the observations applying Navier-Stokes equations and sedimentation in dynamic equilibrium with Brownian motion. Flocculation and friction forces affect yield stress and plug flow of fibre suspensions, as understood already in 1922 (Smith 1922). Extensive experimental and modelling studies of the effects of flocculation, aspect ratio, fibre orientation and swelling chemistry on the complex fluid dynamics of fibre suspensions have been made by many researchers (Norman *et al.* 1977, Yan *et al.* 2005, Dalpke and Kerekes 2005, Horvath and Lindström 2007, Lindström 1986, Laine *et al.* 2000, Schmid *et al.* 2000). Rheological studies of fibre suspensions show an increase in network strength through the increase in elastic modulus and critical strain, with yield stress related to a power law of the consistency, for consistencies having $N > 16$ (Kerekes *et al.* 1985, Swerin *et al.* 1992), though the non-coherent fibre suspension does not actually have a true yield stress, but depends on many interactions and states displaying many individually contributing mechanistically related yield stresses (Barnes and Nguyen 2001, Barnes *et al.* 1989, Nguyen and Boger 1992).

In research made by Landman *et al.* (Landman *et al.* 1991, Landman and Russel 1993, Landman *et al.* 1995) the concept of the network possessing a compressive yield stress $\tau_0^y(\phi)$ is introduced as a function of suspension strength of the particle network, and is in turn described as a function of local volume fraction ϕ , as presented in Fig. 13. As seen from this figure, $\tau_0^y(\phi)$ increases with increasing ϕ , as more particles per unit volume indicate more interconnections and stronger network structure, and at the gel point ϕ_g , the suspension consists of isolated disconnected flocks, which are themselves fully networked (Landman *et al.* 1995). The same authors use a power law expression to fit experimental data

$$\tau_0^y(\phi) = k \left[\left(\frac{\phi}{\phi_g} \right)^n - 1 \right] \quad (26)$$

with suitable fitted values for the coefficients k and n .

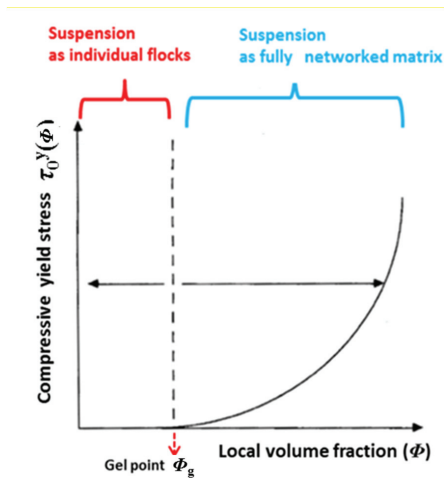


Figure 13 Form of the compressive yield stress. Scale-up procedures and test methods in filtration: a test case on kaolin plant data scale up procedures/ Adopted from references (Landman *et al.* 1995)/.

As the disconnected flocs have a higher concentration than the suspension average, they have a greater cohesive strength than the other parts of the suspension, resulting in an increase in local viscosity and yield stress. On the other hand, large flocs in contrast (large in relation to the dimension of flow) are explained by some authors as hydrodynamic points, which permit breakage of the fluid matrix structure (Bousfield 2008, Cui and Crace 2007, Hubbe 2007, Tatsumi *et al.* 2002).

Different authors prefer different ways of fitting experimental data to the variety of yield stress models, as discussed above (Derakhshandeh *et al.* 2011, Cheng 1986, Coussot 2005) and as is shown in Fig. 14. A review made by Derakhshandeh *et al.* (Derakhshandeh *et al.* 2011) summarises the various ways of fitting fibre suspension experimental data to the different yield stress models, within and outside LVE, as discussed above (Fig. 14). A summary of terms associated with these approaches is hereby provided. *Maximum viscosity yield stress* is defined as the value of shear stress at which the instantaneous viscosity exhibits a sudden significant decrease from a maximum as shear is increased. *Apparent yield stress* required to initiate flow is obtained as the intercept by extrapolating shear stress to zero shear rate, usually from the linear portion of the stress-shear curve. *Ultimate shear strength*, (apparent yield stress) is the maximum stress reached when strain is increased to initiate flow after which the stress decreases. *Oscillatory shear* is another approach to the measurement of apparent yield stress with oscillatory measurements using tangent method explained above.

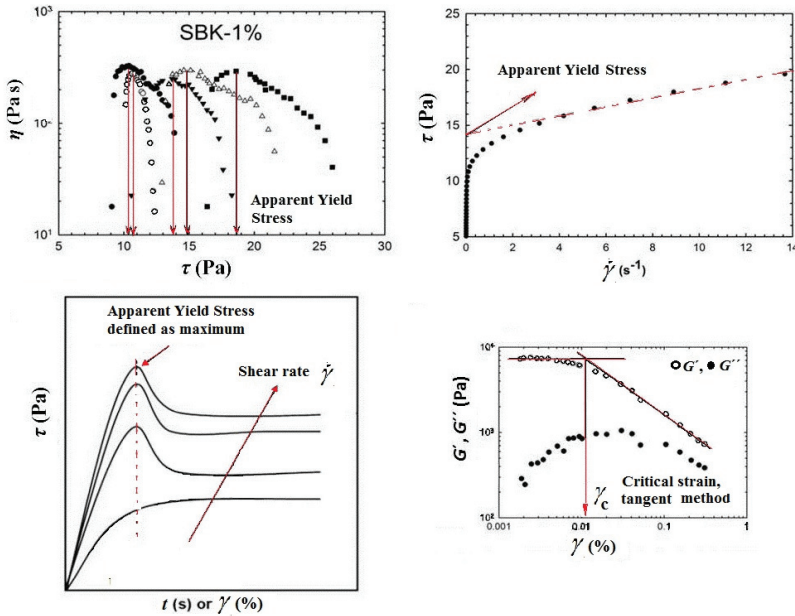


Figure 14 Different determination methods for apparent yield stress of pulp suspensions: application of a linear shear stress ramp and determining yield stress as the maximum of the instantaneous viscosity; extrapolating stress values at higher shear rate to zero shear to define the apparent rest value of stress; critical shear strain as the initiation of the breakdown of storage modulus under shear / Modified from reference (Derakhshandeh *et al.* 2011)/.

2.2.4 Viscoelasticity and flow properties of MNFC

The rheology of particle gels is related mainly to the mechanical aspects, such as the bending and breaking of the bonds in the structure (Gisler *et al.* 1999, Kavanagh and Ross-Murphy 1998, Van Hecke 2005). The gel formed from MNFC particles incorporates flexible surface-surface bonds of aggregates interspersed with bound water, which results in a stable network structure (Aulin *et al.* 2009, Hult *et al.* 2010). Typically, for MNFC suspensions η^* is much higher than the steady shear viscosity η at equivalent shear rates, with G' being significantly greater than G'' and with both elastic moduli being independent of ω . These properties are typical of gels (Iotti *et al.* 2011, Richmond 2012, Saito and Isogai 2005). Under flow conditions, increase of shear rate ($\dot{\gamma}$) enhances both the aggregation and fragmentation of MNFC (Saarikoski *et al.* 2012, Saarinen *et al.* 2014) and deformation of the predominantly gel-like structure, resulting in flow curves showing hysteresis and thixotropic behaviour as presented in Fig. 15 (Illa *et al.* 2013, Puisto *et al.* 2012a, Puisto *et al.* 2012b). In complex colloid systems, as MNFC suspensions are, the final equilibrium state is governed by a number of parameters describing hydrodynamic shear stress that distorts or pulls structures apart, which are often incorporated into modelling thixotropy (Coussot *et al.* 2002, Divoux *et al.* 2013, Dullaert and Mewis 2006, Mewis and Wagner 2009).

One important rheological property of these fluids is the so-called stress overshoot – a phenomenon typical of colloidal suspensions (Dickinson and Chen 1999, Gisler *et al.* 1999, Klein *et al.* 2007). The overshoot is dependent on MNFC suspension consistency, applied shear rate and shear (pre-shearing) history of the colloidal suspension, as these complex fluids are capable of storing elastic energy in aggregate cohesion (flocs) or within the gel matrix (Keshtkar *et al.* 2009, Mobuchon *et al.* 2007, Puisto *et al.* 2012a, Puisto *et al.* 2012b).

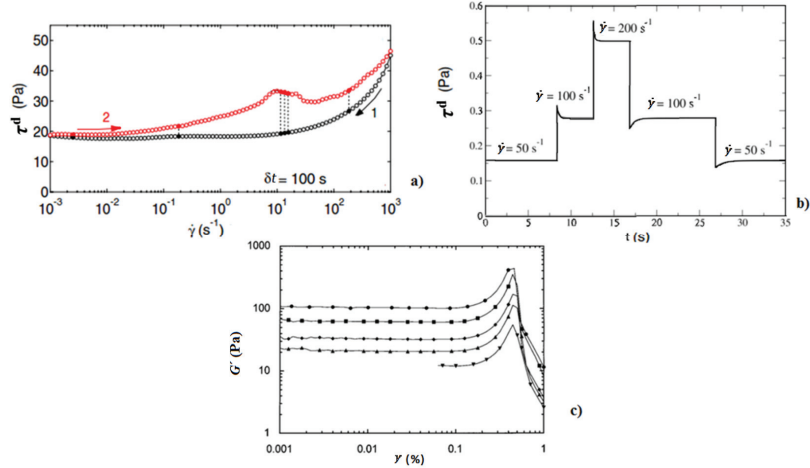


Figure 15 Nonlinear rheological curves of complex soft glassy materials, similar to MNFC suspensions, showing thixotropic transient and gel hardening behaviour/Modified from referencias as mentioned / a) shear stress (τ) hysteresis of 3 % laponite suspension with 0.3 % glass spheres for 100 s interval step, over wide shear range (Divoux *et al.* 2013), b) transient shear stress (τ^+) response for different shear rates with overshoots for modelled 0.01 % NFC suspension (Puisto *et al.* 2012), and c) elastic modulus (G') as a function of the strain amplitude (γ) in an oscillatory shear experiment for different volume fractions of polystyrene latex gel (Gisler *et al.* 1999).

2.2.5 Wall slip and shear banding

Accurate rheological characterisation using rheometric flows assumes that the velocity of the sample at the sample boundary must be equal to the velocity of the adjacent measuring plate so that the deformation rate of the sample is known as presented in Fig. 16 (Ovarlez *et al.* 2009, Weber *et al.* 2012). However, in suspensions, emulsions and colloids a thin “depletion” layer can form as particles/droplets migrate away from the boundary layer of the measuring geometry/spindle, thus forming a region with reduced local viscosity which results in inhomogeneous deformation through the sample (Aradian and Cates 2006, Divoux *et al.* 2010, Møller *et al.* 2006). Polymers in solution are driven entropically away from boundary layers, i.e. avoiding ordered alignment at the boundary, and thus forming depletion layers with absence of flow and slip in the liquid suspending phase remaining at the boundary (Weber *et al.* 2012). As a consequence of wall slipping, rheograms exhibit unstable flow curves which are characterised by a “zig-zag” rise and fall patterns, which have large amplitudes of oscillation above a certain rotation speed (Klein *et al.* 2007, Pal 2000, Yeow *et al.* 2006, Yeow *et al.* 2007, Coussot 2005).

However, wall slip may also be mistaken in rheograms for another effect due to the strong nonlinearity of the rheological behaviour of thixotropic materials (Ovarlez *et al.* 2009). The phase separable nature of MNFC can be considered to act similarly, and they regularly display wall slip (Jin *et al.* 2011, Saarinen *et al.* 2013, Puisto *et al.* 2012b).

There are several typically used approaches to overcome wall-slip. Mathematically these include correction of parameters in flow models, while experimental methods include different means of modifying the surfaces of the standard rheological tools, Fig.16. This is usually accomplished by either roughening the surfaces or by attaching a rough material such as sandpaper or using geometry with serrated surfaces, i.e. cleats, although chemical modifications of the surfaces have also been used (Seth *et al.* 2008, Valencia *et al.* 2003, Walls *et al.* 2003). In vane bucket geometry, wall slip is partially overcome by use of vane spindles (Barnes and Nguyen 2001, Barnes 1995, Dalpke and Kerekes 2005, Coussot 2005). Unfortunately, slip can still persist even with surface modified tools, especially for gels and elastomers (Hu *et al.* 2002, Russel and Grant 2000).

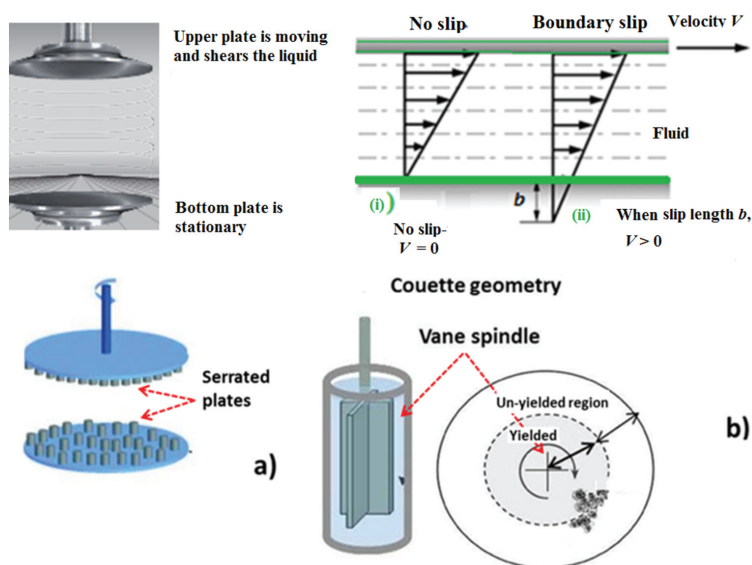


Figure 16 Different geometries used to reduce wall slip a) serrated surface in plate-plate geometry b) vane spindle in wide gap vane bucket geometry / Modified from courtesy of Anton Paar USA and reference (Weber *et al.* 2012).

Presence of wall slip in oscillatory plate-plate measurements performed with smooth plate geometry is seen at rheograms as a lowering of the values of τ_0^s , with a typical hump or secondary plateau appearing in the plot of G' against τ^s , as presented in Fig. 17 (Klein *et al.* 2007, Walls *et al.* 2003).

Yield properties of thixotropic materials reflect a continuous parallel process between aging and shear-induced rejuvenation, which leads to a so-called shear banding phenomenon (Coussot 2005, Divoux *et al.* 2010, Divoux *et al.* 2013, Moler 2010, Ovarlez *et al.* 2009, Møller *et al.* 2010, Bertile *et al.* 2003).

The same authors observed shear banding profiles with magnetic resonance imaging (MRI) and ultrasonic Doppler velocimetry (UDV), within both plate-plate and Couette geometry, as presented in Fig. 17.

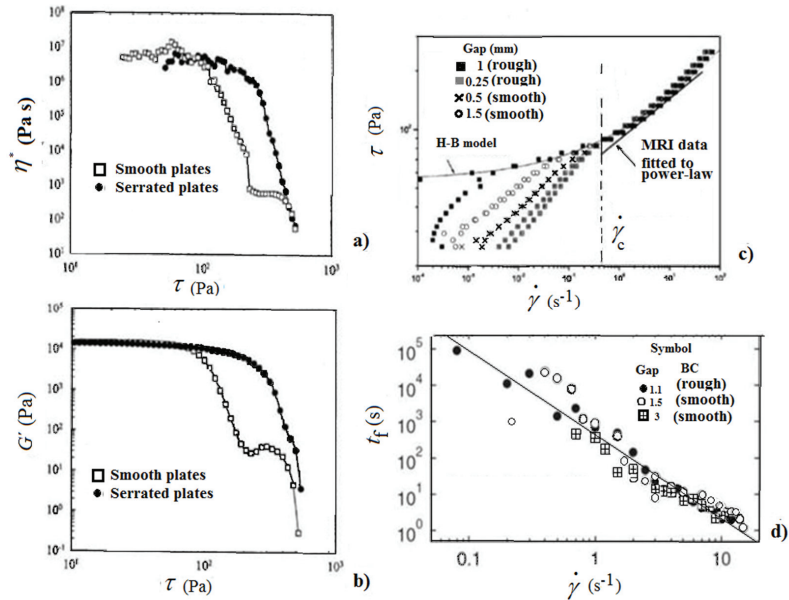


Figure 17 Wall slip seen in rheograms as a function of geometry/Modified from references / a) lower yield point due to wall slip in plate-plate geometry (Walls *et al.* 2003), b) lowered elastic yield stress due to wall slip in plate-plate geometry (Walls *et al.* 2003), c) stress ramp within Couette geometry measured with MRI (Bertola *et al.* 2003), and d) fluidisation time within Couette geometry measured with UDV (Divoux *et al.* 2010).

2.2.6 Coating colours

Coating colours used to apply pigmented coatings on paper surfaces are composed of a mixture of components containing colloidal particles and dissolved polymers (Triantafillopoulos 1985, Bousfield 1999, Gane *et al.* 1992, Moan *et al.* 2002). To obtain a uniform coating layer with good printability characteristics, it is necessary that high solids accompanied with sufficient water retention properties be controlled through the application and levelling process, to avoid problems in the coating transfer such as deposits on the blade and coating marks (Gane *et al.* 1996, Iyer and Bousfield 1996, Laudone *et al.* 2006).

2.2.6.1 Pigments and their interaction in the dispersed medium

Kaolin and calcium carbonate are the pigments most generally used in coating formulations, having differences in their morphological properties, chemical composition and surface charge (Gane *et al.* 2009 Lehtinen 2000).

Simplified shapes of pigment particles are spherical, rod-like or platy, but in reality true particle shapes are quite complicated depending on the crystalline structure related to the mineral chemical composition. The aspect ratio expresses the degree of flatness and is calculated by dividing the particle diameter by the particle thickness, Fig.18. The properties of coating colours and the final coating depend on the particle shape and particle size distribution (PSD), as packing density decreases when PSD becomes narrow (Lehtinen 2000). The particle size of coating pigments is in the micrometre and finer range, and when evaluating the particle size of pigment it is customary in many cases to express the percentage by weight of those particles with a particle size less than 2 μm . Usually for coating colours, for “fine” pigment grades this number is over 90 wt%, and for “coarse” pigment grades, less than 70 wt% (Lehtinen 2000).

Surface charge plays an important role for colloidal stability and dispersion in the coating colour matrix, being the medium where the other formulation components are added. Concentration of electrolytes and pH of the medium affects the dispersion, but specific characteristics of the pigment particles are also important as the packing density affects alignment and particle orientation in flow conditions (Husband 1998, Sandås *et al.* 1989, Sjöberg *et al.* 1999), Fig. 18. The surface charge of calcium carbonate is negative and not dependent on pH, while the kaolin surface charge has different polarities between the face and the lateral edges of the particles, being negative at the faces and positive in the lateral edges at lower pH (Gane *et al.* 2009). The edge charge is dependent on pH, changing to negative in alkaline medium. In industrial applications pigment dispersions are typically kept at pH 8.0-8.5, and a polyelectrolyte is used as a dispersing agent, being adsorbed at the particle surface and functioning as a protective agent. The usual final charge in the dispersed state is anionic, and this is the case in coating colours designed for typical offset, flexographic and rotogravure end-use printing processes.

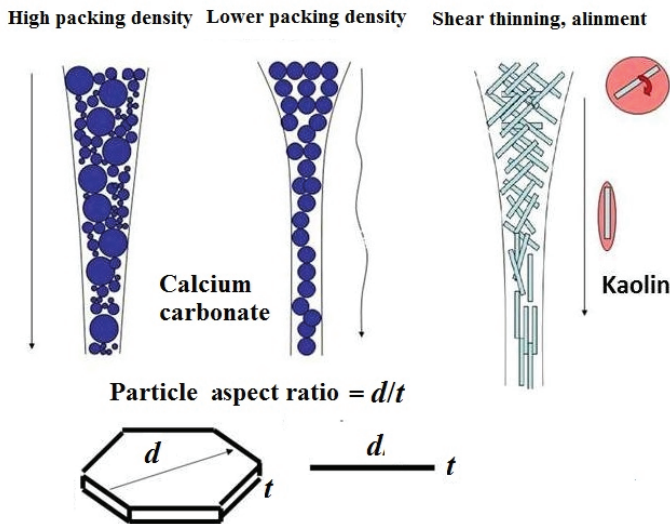


Figure 18 Pigments used in coating colours and the effect of aspect ratio on their orientation in extensional shear flow / Adopted from reference (Gane *et al.* 2009)/.

2.2.6.2 Binder – synthetic latex

The main reason for adding latex in the coating colour is to bind the pigments together and to anchor the coating to the base paper (Schmidt-Thümmes *et al.* 2009). They can be defined in the context of paper coating abinders as aqueous dispersions of colloidal polymer particles whose particle sizes range from 50 nm to 300 nm, affecting the colour of their water dispersions (Lehtinen 2000). The viscoelastic properties of paper coating colours are directly dependent on the structure of the pigment-pigment, pigment-binder interactions (Barbesta *et al.* 2001, Husband 1998, Kugge 2003, McGenity *et al.* 1992, Ridgway *et al.* 2011, Gane *et al.* 1992).

There are three major types of paper coating latices, styrene-butadiene (SB), styrene-n-butyl acrylate (SA) and poly (vinyl acetate) (PVAc). SB lattices of modified copolymers of styrene (hard monomer) and butadiene (soft monomer) at varying ratios ranging from 40/60 to 80/20, with glass transition temperature (T_{gs}) ranging from -25 to 50°C. SA lattices contain modified styrene and n-butyl acrylate (soft monomer), at varying ratios ranging from 40/60 to 60/40 with T_{gs} ranging typically from -10 to 40°C, while PVAc is a homopolymer latex with T_{gs} about 13°C, being film-forming at room temperature (Barbesta *et al.* 2001). Commercial SB and SA lattices can have low, medium and high levels of carboxylation for unique paper strength properties, as high binding strength and high mechanical stability. The carboxylated SB and SA lattices are compatible with various pigments and natural binders, and improve the colloidal stability of coating formulations, while PVAc interacts strongly with kaolin in coating formulations via hydrogen bonding between alcohol groups latex particle surface and silanol groups on clay particle faces, resulting in very high viscosity of the suspension (Triantafillopoulos 1985, Gane *et al.* 1992, Bousfield 1999, Barbesta *et al.* 2001).

2.2.6.3 Co-binders and thickeners – depletion flocculation

The main function of thickeners is to adjust viscosity of the coating colour to the desired level and impart the necessary degree of water retention (Kloow *et al.* 2009, Dahlvik *et al.* 1996, Gane *et al.* 1992). The thickeners and co-binders most commonly used are water-soluble natural polymers such as starch (also frequently used as natural binder instead of, or to complement, latex) or polyelectrolytes such as CMC. Synthetic products include PVAc, acrylic copolymers and associative thickeners (John Roper *et al.* 2009, Kloow *et al.* 2009). The binding power of PVAc exceeds that of all other binders used in paper coatings; nevertheless, it is usually used only in relatively small fractions in coating colours to carry optical brightening agents (OBA) or in inkjet formulations (Buri *et al.* 2012, John Roper *et al.* 2009, Triantafillopoulos 1985).

Thickeners need to be able to interact strongly both with water molecules, by hydrodynamic mechanism or flocculation to restrict mobility of the aqueous phase, and interact with other ingredients of coating formulations, especially pigments, in order to display a thickening effect (Hanciogullari 2000). Stiffness and extension of individual polymer chains at their anionic charge range, and their crosslinking reduces mobility of aqueous phase. The nature and strength of those interactions depends on the chemical composition of the polymer, Fig. 19. Acrylic and cellulosic thickeners have high affinity for pigments because the polar functional groups of the thickener molecule are attracted by the polar surface of the pigment, which increases degree of crosslinking within the system and adds to the thickening effect (Hanciogullari 2000, Kloow *et al.* 2009).

Co-binders have shorter monomer chains and lower average molar mass, being less anionic they adsorb more readily on the surface of clay pigments. Since they have lower thickening effect than thickeners, they can be added to coating colours in larger quantities. One of the most important side effects of co-binders is that they boost the performance of optical brightening agents (OBA), who absorb UV light and reemit in the blue part of the visible spectrum, masking the yellowish shade of the base paper and coating (Hanciogullari 2000, Kloow *et al.* 2009). Depletion flocculation induced by the high charge density of CMC, for example, together with Ca^{2+} bridging are the two main causes for static structure development (Husband 1998, Ridgway and Gane 2007, Sosa *et al.* 2006, Kloow *et al.* 2009).

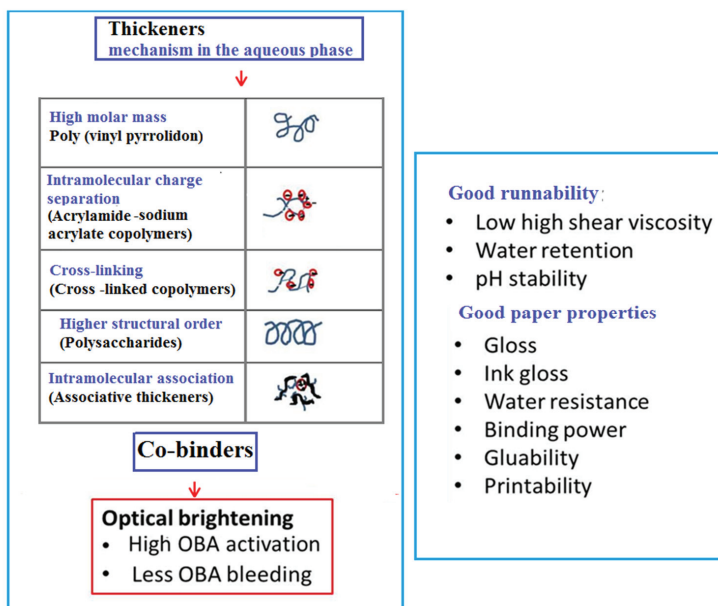


Figure 19 Co-binders and thickeners used in coating colour suspensions / Modified from reference (Hanciogullari 2009)/.

In formulations with kaolin clay the differences in water retention between different CMC grades are much smaller than in colours based on calcium carbonate, as CMC quickly builds up a network structure with clay particles resulting in flocculated structure that increases water retention (Gane *et al.* 1992, Larsson *et al.* 2000). Thickeners have influence on the water retention by inducing an osmotic pressure within the coating colour, which prevents excessive excessively fast water loss from freshly applied coating colour onto the base paper, which resists the capillary pressure of the base paper and the hydrodynamic pressure upon metering, Fig. 20.

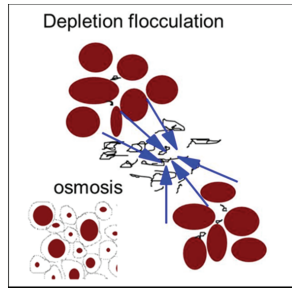


Figure 20 Effect of depletion flocculation by CMC on pigments and water molecules / Adopted from reference (Gane et al. 2009)/.

2.2.6.4 Importance of Viscoelasticity in Coating

The importance of viscoelasticity in blade coating of paper and paper board can be expressed theoretically via the Deborah number (De), which is the ratio between a characteristic relaxation time of the fluid λ , defined as the characteristic half time (or sometimes e-folding time) taken for elasticity to recover after high shear, and the characteristic residence time, t , under shear strain, for example near and under the tip of blade (Triantafillopoulos 1985, Bousfield 1999).

The Deborah number in the LVE region is defined as

$$De = \frac{\lambda}{\Delta t_{\text{deformation}}} = \lambda \dot{\gamma} \quad (27)$$

describing a deformation timescale of $\Delta t_{\text{deformation}}$. When $De > 1$, the fluid behaviour is predominantly elastic, and when $De < 1$ it is predominantly viscous. For a coating colour, this number represents the ratio between the characteristic time it takes for the coating to relax after deformation, and the characteristic time of the process flow. Considering that the characteristic process times at the blade nip are of magnitude 10^{-5} s, the De number is much greater than 1, suggesting that coatings behave more as elastic solids rather than mobile fluids (Triantafillopoulos 1985, Aidun et al. 1997). Coatings can exhibit unique flow behaviour in the blade nip and they may not have enough time to relax after the large deformation due to induced high elasticity (Gane et al. 1992). Under these conditions, the coating colour surface is affected by elasticity, as delay of elastic recovery of coating structure results in the coating layer retaining flow non-uniformities.

2.2.6.5 Relation of rheology to dewatering of coating colours

Application of the coating colour to the paper leads instantaneously to the onset of liquid drainage from the coating colour to the base paper (Kugge 2003, Willenbacher et al. 1998, Lehtinen 2000, Jäder and Järnström 2001). This results in an increasing particle concentration (solid content) in the coating layer and increasing surface roughness of the base paper resulting in breaking of bonds in the base paper which can further result in losses in productivity (Gane and Hooper 1989, Jäder and Järnström 2001, Dahlvik et al. 1997, Kugge 2003).

If the water-retaining properties of the coating colour are low, the solid content of the coating colour rapidly increases, and the dynamic viscosity (η) rapidly increases and the critical shear rate at which dilatancy appears decreases to within the application shear rate. Therefore the rheology of the coating colour has to be tuned in order that, during the application to the base paper, the right viscosity and elasticity enable optimal runnability and water retention (Toivakka *et al.* 2001, Sand *et al.* 2011), Fig. 21. In blade coating, excessive dewatering of the coating layer is linked to coating scratches, blade deposits and high blade forces (Eklund and Letzelter 1993), while in metered size press application too little dewatering is related to misting and film split quality issues (Gane *et al.* 1997, Roper *et al.* 1997). Also for spray coating operations, rapid dewatering limits droplet levelling and merging, and so reducing the final coating layer uniformity (Toivakka *et al.* 2001).

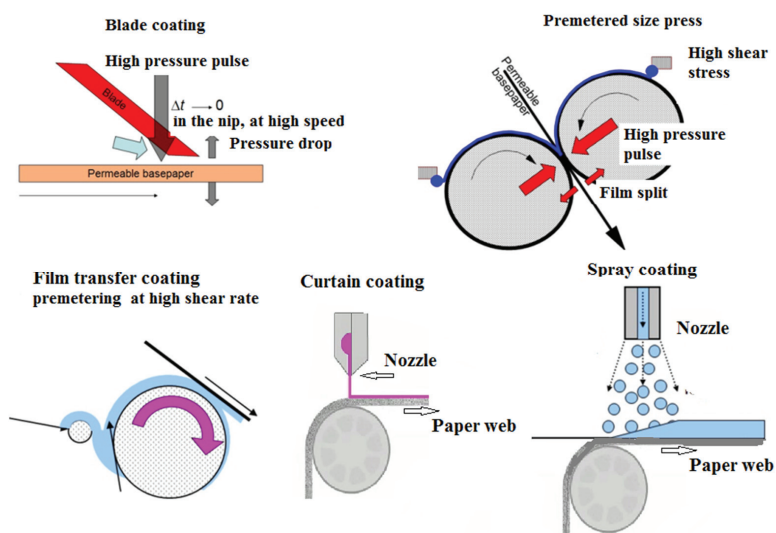


Figure 21 Different coating processes / Modified from reference (Gane *et al.* 2009)/.

The application and metering phases in a coater can be divided between three parts, the application itself and the dwell time between application and metering, which has been studied and modelled by (Letzelter and Eklund 1993, Forsström 2009). If the coating is applied with a method that induces a significant hydrodynamic pressure upon application, such as with applicator roll, the pressure dewatering will cause a partial immobilisation of the coating colour. During the subsequent dwell time, second stage prior to metering, additional dewatering will take place by capillary absorption (Aidun and Triantafillopoulos 1997, Sandås *et al.* 1989). Longer dwell time allows a thicker filter cake to be formed next to the substrate (Berg *et al.* 2011).

In the third stage, under the blade and final coat weight metering, there is again a pressure pulse under the blade, which delivers a rapid rate of change of strain with related induced elasticity and pressure pulse dewatering (Gane 1997, Forsström 2009), as presented in Fig. 22. Between application and immobilisation, and after metering, the coating colour is again dewatered by means of capillary forces and diffusion.

The rate of water penetration is dependent on the paper surface properties, pore size and surface energy relation between liquid phase and base paper. Hydrophobic sizing of the paper substrate reduces the amount of water transported into the base paper through capillary suction (Toivakka *et al.* 2001, Salminen 1988, Bristow 1971). The presence of a filter cake protects against penetration of fine particles into the basepaper pores, and filter cake thickness is important as it increases flow resistance through the immobilised layer due to smaller pore radius within the layer and a more tortuous structure (Grön *et al.* 2009, Letzelter and Eklund 1993). The size and range of particles in suspension plays an important role in defining the total net hydrodynamic forces and torques between particles during filter cake consolidation (Sand *et al.* 2009, Lohmander 2000, Toivakka and Bousfield 2009). Platy (high aspect ratio) pigments such as kaolin and talc give layers with higher tortuosity than do isometric pigments such as ground calcium carbonate (Grön *et al.* 2009, Forsström 2009).

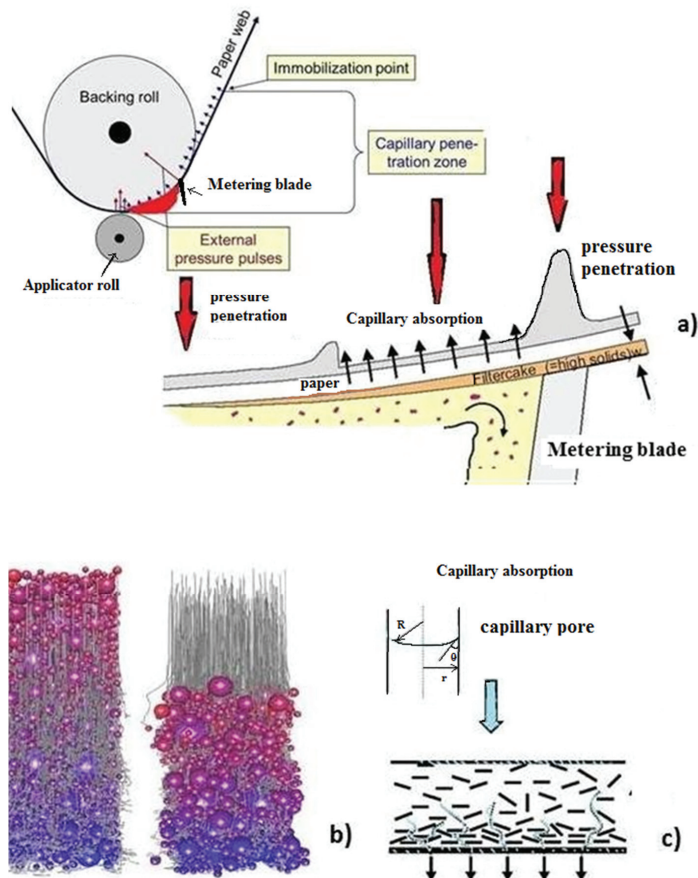


Figure 22 Difference in dwell time in different coating colour application methods, pressure vs. capillary penetration: a) coating colour application (Grön *et al.* 2009), b) consolidation trajectories of particles with different velocities, red= high velocity and blue = low velocity (Toivakka *et al.* 2008), and c) coating consolidation of liquid into base paper through clay pigments filter cake, capillary penetration (Grön *et al.* 2009).

2.3 Filtration

The bulk of coating colour penetration under pressure can be explained as coating colour flow into the base paper structure, the rate of which is proportional to the pressure gradient. Filtration is a mechanical physical separation process in which solid particles suspended in a fluid are mechanically removed via porous media, forming a cake. In the paper industry, filtration theory has been applied to such processes as pulping and refining as a method of evaluating pulp processing, dewatering and fibre mat formation in the forming section of a paper machine, as well as filter cake formation on the surface of paper during coating dewatering (Lepoutre 1989, Sand *et al.* 2009, Kugge 2003, Sandås *et al.* 1989, Toivakka *et al.* 1992, Wildfong *et al.* 1998).

2.3.1 Modelling the filter cake formation

In the first stage of the filtration process there forms a compact bed that builds up on the filter medium as individual flocs and particles are delivered to the membrane by the fluid flux through membrane (Landman *et al.* 1991).

A filter cake is formed if $\phi(z,t) > \phi_g$ inferring $\tau_y(\phi(z,t)) > 0$, with the compact bed volume fraction being uneven in the z -direction, as explained by Landman *et al.* (Landman *et al.* 1991, Landman and Russel 1993, Wakeman *et al.* 1991). The same authors (Landman *et al.* 1995) introduce the parameter $r(\phi)$ as a factor that represents hydrodynamic interaction between near neighbour particles as a function of concentration and flocculation, affecting the drag on any other given particle, given as (Theis-Weesie and Philipse 1994)

$$r(\phi) = (1 - b\phi)^m \quad (28)$$

where b and m are fitting constants.

If laminar flow is assumed, the flow of filtrate $V(t)$ of viscosity η , through a rigid packed bed can be presented by Darcy's Law (Wildfong *et al.* 1998), given as

$$\frac{\Delta P}{\eta L} = \frac{v}{k_D} \quad (29)$$

where k_D is Darcy permeability constant, ΔP is pressure drop across the medium of thickness L , and v is the liquid volumetric flux per unit sample area A , given as

$$v = \frac{dV(t)}{dt} \frac{1}{A}, \text{ where } V(t) \text{ is volume of filtrate.}$$

Darcy's law is a phenomenological description of laminar incompressible flow through porous permeable materials. It states that the flow rate through the porous material is proportional to the applied pressure gradient, where the coefficient of proportionality can be expressed as a ratio of two further coefficients, namely the permeability, which is the property of the porous material only, and the dynamic viscosity, which is the property of the fluid only.

A more accepted model for furnish filtration is the Carman-Kozeny (Wildfong *et al.* 1998). The Carman-Kozeny expression for Darcy permeability constant is given as

$$k_D = \frac{\varepsilon^2}{k_1 \eta S_v^2 (1 - \varepsilon)^2} \quad (30)$$

where k_1 is the Kozeny shape factor ($= 4.17$ for randomly packed beds (Geankoplis 1983)), S_v the specific volume surface area, and ε the porosity or void volume.

The Carman-Kozeny relation correlates the Darcy permeability coefficient with the material porosity and specific surface area. The expression of the Carman-Kozeny relation contains the Kozeny constant (shape factor), which depends on the pore geometry and is *a priori* unknown. In both cases the models employed assume fully developed Poissueille flow, which ultimately can be described as flow through a set of parallel capillaries matching the permeable flow capacity. Both Darcy and Carman-Kozeny by inference require that the structural scale of the porous material is small compared with the length of the flow path. The Carman-Kozeny relation might also be applied together with Darcy's law, for example, in cases where the permeability of the material changes during the flow process, due to changes in porosity and specific surface by compression or accumulation of fine particles passing through the structure. Also, Eq. 30 can be put in Eq. 29 to give the Carman-Kozeny equation for the specialised case for the defined material to obtain Darcy's expression, which relates the pressure drop to specific properties of the porous bed, as discussed previously, (Irmay 1958).

$$\frac{\Delta P}{L} = \frac{\eta k_1 (1 - \varepsilon)^2 S_v^2}{\varepsilon^3} v \quad (31)$$

2.3.2 Filtration in paper forming

The drainage rate during sheet forming is a critical issue in the operation and design of the wet-end of a paper machine (McGregor and Knight 1996). This drainage process occurs on top of a forming fabric, which can travel at surface speeds up to 1 900 m.min⁻¹. The paper web forming process is essentially based on the removal of water from flocculated pulp suspension (mixture of fibres, suspended particles and additives) through the pores of the fabric while a fibrous network is being formed. A variety of methods have been developed to predict how rapidly water will be removed during the formation of the wet paper web (Kerekes and Harvey 1980, Hubbe and Wang 2002, Roschy *et al.* 2002, Paradis *et al.* 2002). These methods include the application of vacuum, or pressure pulsations, intended to simulate the environment of a modern paper machine, (Räisanen *et al.* 1995) and model parameters describing pressure filtration of the flocculated suspension (Landman 1995, Parry 2006, Chen *et al.* 2002).

Recently, various strategies have been developed to increase the release of water using chemical additives, enhancing the flocculation of cellulosic fibre fines (Roschy 2002). Fines fractions in papermaking furnish play a predominant role relative to retarding dewatering rates (Przybysz 1973, Patel and Trivedi 1994, Liu 2001). Fines are termed both cellulosic fines, which may consist of ray parenchyma cells (primary fines) or of

fibril fragments removed from cell walls during refining (secondary fines), and fillers (Wildfong *et al.* 1998, Hubbe 2007). Colloidal matter, emulsion droplets, polyelectrolytes and polyelectrolyte complexes can be also considered as fines, also affecting filtration of the paper furnish (Allen 1979, Hubbe and Panczyk 2007, Zhang *et al.* 2000). In the Shirato-Wakeman model (Shirato *et al.* 1985) of the compact bed formation with applied external pressure ΔP , the pressure drop in the fluid phase is taken as the sum of the pressure drop acting across the growing compact bed and the pressure drop across the filtration membrane

$$\Delta P = \eta \alpha c V \frac{dV(t)/A}{dt} + \eta R \frac{dV(t)/A}{dt} \quad (32)$$

where R is the membrane hydraulic resistance and c is effective solids mass concentration of the growing compact bed, α is the flow resistance through the compact bed, and $cV(t)$ is thus the mass of the compact bed at time t . The time varying specific volume flux of filtrate per unit cross section area A is $\frac{dV(t)/A}{dt}$, Eq. 29, such that, for unit area, $V(t)/A = h_0 - h(t)$, where h_0 is the height of the un-networked suspension (before filtration), and $h(t)$ is the compact bed height. The water flux as a function the height loss of the sample as water is expelled is therefore given as (Landman *et al.* 1995)

$$\frac{dV(t)/A}{dt} = - \frac{dh(t)}{dt} \quad (33)$$

2.3.3 Formation of filter cake in coating colours

We can conclude that Darcy permeability is also a suitable description for fine pigmented coating colours forming a filtercake. Darcy's Law governing the volume flow rate, dV/dt , per unit cross-sectional area of the sample is given by (Bousfield *et al.* 2008)

$$v = \frac{dV}{dt} / A = \frac{k_D \Delta P}{\eta L} \quad (34)$$

where ΔP is the pressure difference across the distance in the flow direction for sample length L , η is the viscosity of the fluid phase of volume V passing through the filter cake and A the area of sample perpendicular to the flow.

By applying the physically imposed boundary condition of volume/mass balance in respect to the particles, the volume of particles in the filter cake must be equal to the volume of particles that was originally in the fluid that has gone through the filter (Bousfield *et al.* 2008) then

$$Al_t \phi_m = \frac{V\phi}{(1-\phi)} \quad (35)$$

where φ_m and φ are the volume fractions of particles in the filter cake and the suspension, respectively, and l_f is the filter cake thickness. The distance of the flow L from Eq. 34 is the same as the filtercake thickness l_f in Eq. 35, i.e. from the generalised sample length L we consider the filter cake thickness l_f as a specific case.

When Eqs. 29 and 34, and Eq. 35, are therefore combined, the volume of the filtrate V removed per unit area A , as a function of time t can be written as

$$\left(\frac{V}{A}\right)^2 = \frac{2k_D \Delta P (1-\varphi) \varphi_m t}{\eta \varphi} \quad (36)$$

which is the basic filtration equation when the resistance of the filter medium is considered constant in respect to permeability (Bousfield *et al.* 2008).

According to Bousfield (Bousfield *et al.* 2008) the Darcy coefficient can be estimated also in respect to the filter cake void volume and particle size applying the Blake-Kozeny equation as

$$k_D = D_p^2 \frac{\varepsilon^3}{150(1-\varepsilon)^2} \quad (37)$$

where D_p is the particle diameter and ε the pore void volume.

2.3.4 Gel water retention

Gels are soft solid-like systems, being highly non-linear, transient and non-equilibrium in nature, being able to support high stress due to their spanning network of particle chains (Gisler *et al.* 1999, Teece *et al.* 2011). In general, the behaviour of gels follows their osmotic behaviour in respect to swelling. Examples of gel-like materials studied in detail rheologically are included in the work of many authors (Flory 1953, Jones *et al.* 1997, Katchalsky *et al.* 1951, Kavanagh and Ross-Murphy 1998, Ricka and Tanaka 1984). The swelling for common gels depends on solvent quality and crosslink density, and large swelling by water trapping is typical for charged particle gels, such as NFC in water. The swelling of gel may be characterised by a swelling ratio (at equilibrium) (Ratner *et al.* 2004)

$$Q = \frac{V_{\text{swollen}}}{V_0} = \frac{1}{\varphi_p} \quad (38)$$

where V_0 is the volume of gel in the initial dry state, V_{swollen} the swollen volume and φ_p the volume fraction of polymer/NFC in the swollen state.

The swelling ratio is determined by the equalising of two pressures: the osmotic pressure acting towards expansion and the reaction by the contracting stress of the gel network. Gel network swelling pressure is dependent on charged groups attached to the network and electrostatic interactions with solvent defined in Donnan theory (Ricka and Tanaka 1984).

Under equilibrium conditions within gel and solvent, the Gibbs free energy of the gel (G_G) is dependent on its many constituents (Flory 1953, Ricka and Tanaka 1984)

$$G_G = G_{\text{net}} + G_{\text{sol}} + G_{\text{dis}} + G_{\text{Coul}} \quad (39)$$

where G_{net} is the free energy of the neutral network defined by interactions of gel and solvent, G_{sol} represents the free energy for a dilute solution of ions or neutral molecules within the gel, G_{dis} is introduced to account for the dissociation of the acid groups on the available sites of the network and G_{Coul} is a parameter associated with Coulombic interactions within the gel and other system, such as cations being attracted to negative groups of the gel resulting in respect to Donnan potential (Hirokaawa and Tanaka 1984, Ricka and Tanaka 1984).

Therefore, when considering the properties of materials containing a proportion of NFC, we must take into account that the water holding capacity of the inter-nanocellulose regions dominates to such an extent that there exist regions of gel-like material. These regions can either behave as an isolated structure or incorporate other materials depending on their respective polarity and sorption potential for water. Therefore, in a non-interacting system, the rheological properties will display either a sum of the two components or a phase-separated behaviour, as observed in pilot coating of MFC furnishes by Richmond *et al.* (Richmond *et al.* 2012).

When studying dewatering of nanocellulose based suspensions, it is this gel-like behaviour that determines the dewatering and water retention properties. These properties can be changed by any agent that alters the osmotic pressure, e.g. pH (Curves *et al.* 2009), salt concentration (due to the charge relationship) (Legrand *et al.* 1998), temperature (Ercili-Cura *et al.* 2012, Hirokawa and Tanaka 1984), addition of non-gellant material, such as fibres, and inert particles, such as mineral fillers.

2.4 Coating layer structure

2.4.1 Porosity of dry coating layer structure

The resulting pore structure of coating affects a wide range of properties, including light scattering and printability (Kloow *et al.* 2009, Gerstner 2010, Ridgway and Gane 2007, Gane and Kovunen 2010). For light scattering optimisation the pore size distribution should be narrow and monodisperse (Gane and Koivunen 2010), with the pore size and particle size defined in relation to the wavelength of light ($\sim\lambda/2$), and for optimal printability, depending on the print method, there needs to be a controlled distribution of fine pores ($< 0.1 \mu\text{m}$) for capillarity and high chromatographically active surface area, and larger connected pores for required permeability (Gane *et al.* 2006, Preston *et al.* 2002, Ridgway *et al.* 2006). Additionally, the surface chemistry must be chosen to deliver the correct balance of surface energy for print component wettability.

Due to the difficulty in studying thin layers, and per se small volumes, of liquids undergoing absorption and permeation into coating structures, tablet forming methods were developed by Ridgway (Ridgway *et al.* 2003), and used as a surrogate for the paper coating layer allowing both liquid contact and equilibrium absorption and permeation to be studied (Gane *et al.* 2006, Ridgway *et al.* 2001).

Tablets are formed in a pressure vessel by dewatering the coating colour through a membrane, with the resultant compact showing closely similar pore structure and pore size distribution to real coatings.

Porosity and pore size distribution based on the model of parallel capillaries can be determined by measuring the non-wetting intrusion permeation of the structure using the technique of mercury porosimetry (Androusoopoulos and Mann 1979, Gane *et al.* 1996, Mayer and Stowe 1965). Mercury, being non-wetting, only enters pores under the action of external pressure (Gane *et al.* 2004). The diameter of capillary pores is calculated according to the Young-Laplace equation (Gane *et al.* 1996)

$$\Delta P = -\frac{4\gamma_{LV}\cos\theta}{d} \quad (40)$$

relating the pressure of intrusion ΔP to the capillary of diameter d , where γ_{LV} is the liquid-vapour surface tension, and θ the contact angle at the liquid-solid contact line.

2.4.1.1 Liquid absorption

The absorption of liquid to porous coating structure depends on the surface energy interaction parameter $l\gamma_{LV}\cos\theta$ which describes the Wilhelmy wetting line force, where l is the length of contact between the wetting liquid and the solid surface (Patnaik *et al.* 2006, Schoelkopf *et al.* 2000).

Traditionally, the rate of absorption into a model capillary of diameter d is derived from the balance of the wetting force and the Hagen-Poiseuille viscous drag (Schoelkopf *et al.* 2000) to give

$$x_p^2 = t\left(\frac{d}{4\eta}\right)\gamma_{LV}\cos\theta \quad (41)$$

where x_p is the distance of penetrated liquid, with viscosity η , and known as the Lucas-Washburn equation.

A problem arises with this description as the absorption in real fine pore systems is frequently observed to be linear with time. On the other hand, the inertial flow model, based on the Bosanquet equation (Bosanquet 1923), suggests that a pore size selection occurs on the short timescale. This is related to the volume of liquid being accelerated, and the larger the pore, the greater is the inertial retardation of the liquid entering it. As a result, there is a delay in a large pore compared with a finer pore. Under the highest acceleration, the liquid front is predicted to move independently of viscosity, i.e. it undergoes plug flow until the viscous drag eventually establishes itself (Schoelkopf *et al.* 2002, Ridgway *et al.* 2006) according to the Bosanquet equation

$$\frac{d}{dt}\left(\frac{\pi d^2}{4}\rho x\frac{dx}{dt}\right) + 8\pi\eta x\frac{dx}{dt} = P_{\text{ext}}\pi\frac{d^2}{4} + \pi d\gamma_{LV}\cos\theta \quad (42)$$

where ρ is the liquid density, and P_{ext} is an external pressure if applied.

According to this model, wicked distance x is expressed as

$$x^2 = t^2 \frac{\gamma_{LV} \cos \theta}{d\rho} \quad (43)$$

on condition that the regime at each stage is short lived, i.e. prior to viscous flow (Schoelkopf *et al.* 2000, Ridgway *et al.* 2006, Kettle *et al.* 2010).

Conveniently, water (polar) and hexadecane (non-polar) liquids can be used to establish the relationship between the solid phase surface energy and that of the liquid and to determine their relative absorption rates as a function of time using self-constructed apparatus to capture the changes in absorption volume uptake of samples (Gane *et al.* 1996, Schoelkopf *et al.* 2000, Schoelkopf *et al.* 2002, Ridgway *et al.* 2006).

2.4.1.2 Liquid permeation

Darcy permeability of the coating structure can also be probed using liquid under pressure to permeate the pre-saturated tablet structure. The permeability is seen to be related to pore volume, pore size distribution and, importantly, pore connectivity. Once again, the Darcy Law is applied to determine the permeability constant of the structure. The methodology to enable the convenient study of liquid permeability of coatings (and papers) has also been developed by the same group of workers (Ridgway *et al.* 2011, Wallqvist *et al.* 2006, Schoelkopf *et al.* 2000).

3 Materials and methods

In this study the materials are presented first and thereafter the methods used for their rheological and suspension characteristics.

3.1 Materials sourcing

The materials are described under each categories below.

3.1.1 Pigments

The terminology used to describe the pigments follows the convention: f = fine size distribution, c = coarse size distribution, as determined by Sedigraph, GCC = ground calcium carbonate (Publication III-V).

A commercial precipitated calcium carbonate with scalenohedral morphology (SPCC) (Publications I and II), a coarse Hydrocarb 60 (cGCC) and a finer Hydrocarb 90 (fGCC) were supplied by Omya AG, Switzerland (Publications III and V), together with a narrow particle size distribution fine ground calcium carbonate nFGCC (Covercarb 75 ME, Omya AG, Switzerland) (Publication IV) .

Clay was represented by a low aspect ratio secondary deposit U.S.-sourced fine glossing kaolin fclay (Hydragloss 90, KaMin LLC, Georgia, United States), which has 96 w/w% of particles < 2 μm and $\zeta_z = -45.33$ mV at pH 8.5 and an ISO brightness of 90 % (Publications III and V). High aspect ratio Brazilian rotogravure kaolin clay, CapimTM RG (supplied by Imerys, St. Austell, Cornwall, UK) in slurry form (66 w/w% solids content) (Publication IV) provides a comparison with the low aspect ratio secondary deposit fine glossing kaolin fclay.

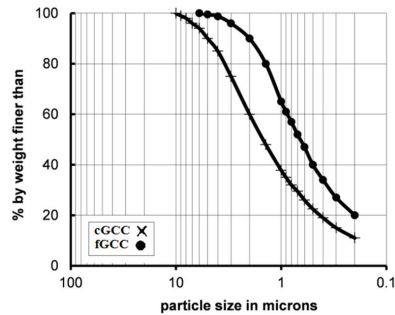


Figure 23 Sedimentation particle size distributions of the two calcium carbonate pigments cGCC and fGCC used to form compacted porous tablet structures (Publications III and V).

3.1.2 MFC and NFC

Microfibrillated (MFC) and nanofibrillated (NFC) celluloses were prepared at the Department of Forest Products Technology in Aalto University. The MFC was prepared by grinding Birch Kraft pulp with an ultra-fine friction grinder (Masuko Supermasscolloider, MKZA 10-15 J) equipped with SiC grinding stones (MKE10-46). Light transmittance for 0.1 % consistency at a wavelength of 800 nm was 34.3 %. The average particle size of MFC agglomerates at conductivity 8 μS was 6.7 μm , and at conductivity 56.1 μS , to that of NFC¹ and NFC² was 3.7 μm , as measured by dynamic light scattering (DLS). The samples NFC¹ and NFC² were produced in a pilot process by oxidising, then fibrillating. TEMPO catalyst was used in the oxidation of the Birch Kraft pulp (Saito *et al.* 2007, Saito and Isogai 2005). The average size of agglomerates, measured with dynamic light scattering (DLS), with measurements performed in triplicate, is presented in Table 1. Carboxylic acid content on the NFC¹ and NFC² as 1.0 $\text{mmol}\cdot\text{g}^{-1}$ and for NFC² was 1.1 $\text{mmol}\cdot\text{g}^{-1}$ determined by conductometric titration. Both NFC¹ and NFC² had a degree of substitution (DS) of 0.2. The reference pulp was a commercial bleached pine Kraft bale pulp which was refined to a Shopper-Riegler SR number of 24 with a Valley Beater.

3.1.3 Binders and co-binders used in coating colours

Thickeners used in this work were a CMC (Finnfix 10, CP Kelco, Finland), with molecular weight 66 kgmol^{-1} and a degree of substitution (DS) of 0.78. A SA-Latex, Styron XZ 96 767.00, was used as binder, having a T_g of 24 °C, a minimum film forming temperature (MFFT) of 20 °C, particle size 105 nm, dry solids content 50 %, pH 8.0 and a viscosity of 320 mPas (Styron Suomi Oy, Palokankaantie 1, FI- 49460 Hamina, Finland), as reported by the supplier. Detailed description of materials and their properties is presented in Table 1.

Table 1 Description of materials used in thesis and Publications.

Particle	pH	Particle/ Agglomerate size	Zeta potential ζ (mV)	Suspension	Publication
SPCC	9	4.3 μm	-9.8	Furnishes	I, II
eGCC	9.2	60 w/w % < 2 μm	-27.13	Coating colours	III, V
fGCC	8.9	90 w/w % < 2 μm	-25.4	Coating colours	III, V
nfCGCC	9.0	75 w/w % < 2 μm	-25.2	Coating colours	IV
clay	8.5	55 w/w % < 2 μm	-45.33	Coating colours	III, V
fclay	8.5	96 w/w % < 2 μm	-45.23	Coating colours	IV
SA Latex	8.1	105 nm	N.A.	Coating colours	III, IV, V
CMC Finifix 10	8.0	molecular weight 66 kgmol ⁻¹	N.A.	Coating colours	III, IV, V
MFC 3 pass Birch kraft pulp	9.5	6.6 μm	-24.3	MFC suspensions Coating colours Furnishes	I, II, III, IV, V, VI
NFC ¹ TEMPO - oxidation	8.9	977 nm	-57.0	NFC suspensions Coating colours Furnishes	I, II, III, V, VI
NFC ² TEMPO - oxidation	8.9	965 nm	-54.0	Suspensions Coating colours Furnishes	IV
pw bleached softwood pine pulp	8.8	(SR 24)	-15.0	Suspensions Furnishes	I, II

3.1.4 MFC/NFC suspensions (Publications I, II, III, VI and VI)

Different consistency MFC and NFC (NFC¹ and NFC²) suspensions were obtained by diluting the initial stock concentrations, as presented in Table 2. Pulp fibre suspensions were prepared from the initial fibre suspension of consistency 1.45 %. Dilutions were made using de-ionised water. The suspensions were labelled according to their consistency and type in respect to material content (MFC/NFC/ pulp).

Table 2 MNFC suspensions used in thesis.

MNFC/Pulp	Initial stock concentration (%)	Suspension consistency (%)	Publication
MFC	3.0	1.0/ 1.5/ 2.0/ 2.3	I, II, III, V, VI
MFC	3.0	1.5/ 2.0/2.3/ 2.5	IV
NFC ¹	2.3	1.0/ 1.5/ 2.0/ 2.3	I, II, III, V, VI
NFC ²	2.5	1.5/ 2.0/ 2.3/ 2.5	IV
Cellulose pulp	1.5	1.0/ 1.5/ 2.0/ 2.3	I, II

3.1.5 High consistency MNFC furnishes (Publication I, II)

High consistency furnishes containing MNFC were made in three consistencies 5/10/15 %. They consisted of 70 % filler pigment, 20/30 % MNFC and 0/10 % pulp fibres. The use of such high fillers loadings was directed toward the opportunity of increasing filler content due to the strength properties imparted by MNFC. The recipes are presented in Table 3.

Table 3 High consistency MNFC furnish formulations.

Furnish label (consistency/MNFC content/ type of MNFC)	SPCC (%)	Furnish consistency (%)	MFC (%)	NFC ¹ (%)	Pulp (%)
5%20%MFC	70	5	20	0	10
5%30%MFC	70	5	30	0	0
5%20%NFC	70	5	0	20	10
5%30%NFC	70	5	0	30	0
10%20%MFC	70	10	20	0	10
10%30%MFC	70	10	30	0	0
10%20%MFC	70	10	0	20	10
10%30%MFC	70	10	0	30	0
15%20%MFC	70	15	20	0	10
15%30%MFC	70	15	30	0	0
15%20%NFC	70	15	0	20	10
15%30%NFC	70	15	0	30	0

3.1.6 Coating colours (Publications III, IV and V)

Coating colours were formulated according to the recipes shown in Table 4 and Table 5.

Table 4 Coating colours formulations; partial substitution with MNFC

(Publications III, V).

Coating colour	eGCC/ ref	eGCC/ MFC	eGCC/ ref	fGCC/ CMC	fGCC/ MFC	fGCC/ NFC	75 eGCC/ ref	75 eGCC/ MFC	75 eGCC/ CMC	50 eGCC/ ref	50 eGCC/ ref	50 eGCC/ NFC	100 fclay/ ref	100 fclay/ MFC	100 fclay/ NFC
Solids content/ w/w(%)	63	63	63	63	63	63	63	63	63	63	63	63	63	63	63
eGCC	100	100	100	0	0	0	75	75	75	50	50	50	100	100	100
fGCC	0	0	0	100	100	100	0	0	0	0	0	0	0	0	0
fclay	0	0	0	0	0	0	25	25	25	50	50	50	100	100	100
SA-latex	15	15	15	15	15	15	15	15	15	15	15	15	15	15	15
CMC	0.4	0.1	0.1	0.4	0.1	0.1	0.4	0.1	0.1	0.4	0.1	0.1	0.4	0.1	0.1
MFC	0	0.3	0	0	0.3	0	0	0.3	0	0	0.3	0	0	0.3	0
NFC ¹	0	0	0.3	0	0	0.3	0	0	0.3	0	0	0.3	0	0	0.3

Table 5 Coating colour formulations; partial/total substitution with MNFC

(Publication IV).

Coating colour	Ref/noCMC	Ref/CMC	MFC/noCMC	NFC/noCMC	MFC/CMC	NFC/CMC
Consistency (%)	62	62	62	62	62	62
nfGCC	50	50	50	50	50	50
fclay	50	50	50	50	50	50
SA-latex	10	10	10	10	10	10
CMC, FinnFix 10	0	4	0	0	0.1	0.1
MFC	0	0	0.5	0	0	0.5
NFC ²	0	0	0	0.5	0.5	0

3.2 Methods applied in the study

3.2.1 Specific surface area and agglomerate size measurements

The zeta potential (ζ) was determined by measuring electrophoretic mobility of pigments and MNFC, by a Zetasizer Nano ZS series (Malvern Instruments Ltd., Worcestershire, UK), by measuring the velocity of the particles using laser Doppler velocimetry. The average particle size of the pigments, MFC and NFC was measured with DSL, using the photon correlation spectroscopic technique (Malvern Instruments Ltd., Worcestershire, UK) (Greenwood 1997). Prior to measuring ζ and ensemble average particle size, the samples were diluted with de-ionised water to a solid content of 0.01 w/w%.

The filler particle size is defined by sedimentation (Sedigraph®, a product of Micromeritics, Norcross, Georgia, USA). The specific surface area of the pigments, shown in Table 1, was determined using a Micromeritics TriStar II (Micromeritics N.V./S.A., Eugène Plaskylaan 140B, 1030 Brussels, Belgium) adopting the BET nitrogen adsorption method (Brauner *et al.* 1938, Pierotti and Rouquerol 1985).

3.2.2 Viscometry

The quasi-static apparent viscosities of MNFC suspensions at 1 - 2.3 % consistency were measured with a Brookfield viscometer (Brookfield DV-II+, ISO 9001) with the recorded torque of the spindle given as % of maximum torque (0.7187 mN.m), as provided by the instrument manual. The geometry employed was the four bladed vane viscosity units V-73 for MFC at 1.0, 1.5 % consistency, and NFC at 1.0 %, and V-74 for the remaining measurements of suspensions and MNFC furnishes, to avoid possible wall slip at the spindle. The geometrical parameters (length/height h and diameter d) are $h = 2.535$ cm, $d = 1.267$ cm and $h = 1.176$ cm, $d = 0.589$ cm, for Spindle V-73 and V-74, respectively.

Apparent low shear (stirring) viscosity of the coating colours was measured with standard spindle #4, with $h = 3.10$ cm and $d = 0.32$ cm, Table.6. The measurement protocol was defined with the computer software Lab Weg connected to the viscometer. The rotation rate and torque were recorded throughout the experiments. MNFC suspensions were placed in a 200 cm³ glass beaker with diameter 6 cm, and coating colours in a 250 cm³ glass cylinder with diameter 8 cm. The distance between the end of the spindle and the glass container bottom was adjusted to be larger than the spindle diameter, according to the Brookfield manual. Samples were pre-sheared at 200 min⁻¹ for 60 s.

For the coating colours and MNFC suspension measurements (Publications III, IV and V) the Brookfield viscometer operated, respectively, at three rotation speeds 10, 50 and 100 min⁻¹ each, with interval duration of 120 s. For each measurement, a new sample was used, and the mean values of the last ten data points at a given rotation speed were used for calculation of the experimental data.

To measure the dynamic flow curves for MNFC suspension measurements (Publication V), the rotation rate was decreased and increased in eight step intervals with 5 min waiting time at each step. The measuring points chosen spread the shear rates logarithmically, leading to a sequence 200, 45, 20, 10, 2, 0.2, and 0.1 min⁻¹, the number of steps was limited by the viscometer's software. The shear stress inside a concentric cylinder rheometer is given by

$$\tau_v = \frac{M}{2\pi h R_c^2} \quad (44)$$

where h is the height of the cylinder and R_c the radius of cylinder, and M is the applied torque .

From Eq. 44 it is easy to realise that in the used geometry due to shear banding, the shear stress at the outer cylinder (at the glass cell) is only around 1 % and 4 % of the values directly at the vane for the V-74 and V-73 vanes, respectively. The normal narrow gap assumption usually used for calculating the shear rate in vane bucket geometry is not sufficient when complex fluids are in question (Heirman *et al.* 2008, Coussot 2005).

The correct shear rate at the rotor is calculated using infinite summation proposed by Coussot (Coussot 2005) and referred to as *corrected protocol* in later analysis

$$\dot{\gamma}(M) = \sum_{p=0}^{\infty} \left[2M \left(\frac{R_v}{R_c} \right)^p \frac{\partial \Omega}{\partial M} \right] \left(M \left(\frac{R_v^2}{R_c^2} \right)^p \right) \quad (45)$$

where M is the torque, Ω is the rotational frequency (revolutions per minute), R_c the radius of cylinder and R_v the inner radius (at vane edge). In the limit of an infinite gap, the summation reduces to the first term, as presented in the results. We further compare the shear rate from Eq. 45, referred to as *protocol from device* in later analysis, with the value for $\dot{\gamma}$ obtained from

$$\dot{\gamma} = \frac{\tau_v(R)}{\eta_v} \quad (46)$$

where $\eta_v = \frac{MS}{\Omega}$, and where Ω is in min^{-1} (rpm) and S a constant defined by separately Brookfield instrument, for V-73 and V-74, respectively. In order to obtain an estimate from the raw data available from the viscometer for $\frac{\partial \Omega}{\partial M}$, which is needed for obtaining the shear rate in Eq. 45, the Herschel-Bulkley type function fit was used

$$M = M_0 + k_v \Omega^{\lambda_H} \quad (47)$$

3.2.3 Water retention WRV

The swelling of MFC and NFC was evaluated with a modified water retention test WRV ISO/DIS 23714: Pulps measurement where

$$WRV = \frac{m_2}{m_1} - 1 \quad (48)$$

where m_1 is the mass of centrifuged wet test pad and m_2 is the mass of the dry test pad. For softwood pulp, WRV is usually between 1.5-1.9 g g^{-1} .

Modification of this test was made to isolate the effect of the MNFC, in that different mixed contents of nanocellulose and Kraft pulp were formed in pads and the WRV measured for each Fig. 24. The incremental change in the water retention value (WRV) of the pads with different MNFC content was used with nanocellulose content in the pads being 0 %, 2 %, 4 % and 6 %, respectively. Plotted curves of apparent WRV against MNFC content in the absorbent pad showed nonlinear behaviour due to saturation of the pad and the incremental contribution of nanocellulose, which was the most obvious in the case of NFC. For this reason, low nanocellulose content of 2 % MNFC was used to establish the best estimate of the water holding capacity of the nanocellulose fraction, and the resulting value later referred to as apparent WRV (Publication II).

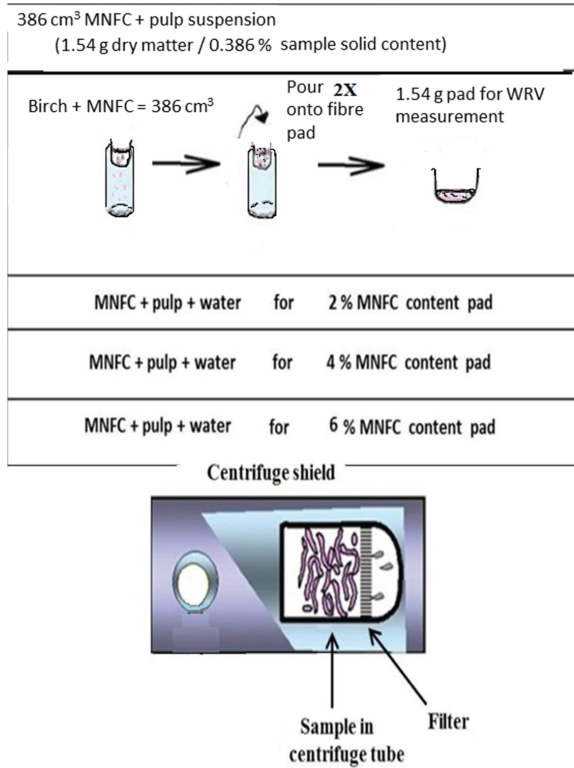


Figure 24 Schematic figure of preparation of MNFC/Kraft pulp pad for WRV measurement/ Modified from NCSU Hubbe/.

3.2.4 Particle level swelling

In order to investigate the effect of molecular level fibre structure, the water fraction in states W_f and W_{fb} in respect to MFC and NFC were measured using a thermoporimetry method developed by Thaddeus Maloney, and explained in Manninen *et al.* (Manninen *et al.* 2013). Thermoporimetry measurements were made on a Mettler 821e Differential Scanning Calorimeter (DSC). It is assumed the melting enthalpy of all freezable water in the MNFC samples is the same as the enthalpy of bulk water, 334 Jg^{-1} (Manninen *et al.* 2013). MNFC samples were exposed to a wide temperature range ($-50 \text{ }^\circ\text{C}$ to $-0.2 \text{ }^\circ\text{C}$ and $-50 \text{ }^\circ\text{C}$ to $+20 \text{ }^\circ\text{C}$) and integration of resulting melting enthalpies (ΔH_m) from different freezing–melting temperatures allowed calculation of the water-state fractions W_f and W_{fb} . The difference between sample moisture content W_c and the total amount of freezable water was used to calculate W_{nf} using Eq.2 and Eq.3.

3.2.5 Rate of dewatering: static and dynamic measurements

The most frequently used experimental methods for determination of coating colour water retention are gravimetric dewatering device (ÅA-GWR) (Sandås *et al.* 1989) and dynamic dewatering with use of a rheometer (Anton Paar 300 Rheometer, GmbH, Austria) equipped with immobilisation cell (IMC) (Willenbacher *et al.* 1998), which can also be accompanied in some methods with optical devices detecting changes in gloss and light scattering during immobilisation, seen as the transition through the first critical concentration (FCC) to the second critical concentration (SCC) (Lepoutre 1989, Watanabe and Lepoutre 1982, Jäder and Järnström 2001, Laudone *et al.* 2004, Pajari and Koskela 2010).

Both ÅA-GWR and IMC tests are long timescale tests, lasting from 30 -100 s, and their drawback is that during the measurement a dense filter cake is formed, affecting results by compounding the measurement of water loss with a continuous decrease in permeation controlling the progressive dewatered amount from sample as a function of time, as explained by Bousfield *et al.* (Bousfield *et al.* 2008).

As the contact time between paper and coating colour in practical high speed coating operations is less than 10 ms (Bousfield *et al.* 2008), and the resulting levelling time is subsequently less than 5 s (Al-Turaif *et al.* 2002, Paradis *et al.* 2002), it would require novel dewatering devices resembling pressure pulse dewatering to become more relevant (Gane 19997), but these will not be discussed in this thesis. Rather, for the purpose of this thesis, whereby we want to determine the effect of MNFC structure and surface properties on immobilisation of papermaking suspensions, long duration dewatering measurement is favourable as it enables one to establish equilibrium and so probe the steady state structure relations.

3.2.6 Gravimetric dewatering measurement with the ÅA-GWR

The static gravimetric dewatering of the pulp suspensions, MNFC containing suspensions and coating colours were measured using the ÅA-GWR, shown in Fig. 25. For MFC, NFC and pulp suspensions, a volume of 10 cm³, and for furnishes, 5 cm³, while for coating colours 10 cm³ were inserted into the cylindrical vessel above a polycarbonate membrane (Nucleopore Track-Etch membrane 5 µm, Whatman) below which is housed an absorbent blotter paper. Several blotter papers were used in each measurement to avoid saturation. The absorbent receiving layer, i.e. blotter papers, is first covered with a membrane and subsequently exposed to the sample for a known amount of time at known pressure.

The dewatering is determined by the amount of water uptake into the absorbent layer gravimetrically. The pressure difference is known and the amount of filtrated water through membrane is measured directly. The cylinder was closed and the sample held under an overpressure of 0.5 bar. After 1 min and 45 s, during which dewatering through the membrane occurred, the pressure was released. The blotter papers were weighed before and after the measurement. The weight difference was multiplied by 15 091 m⁻², which is the inverse of the cylinder cross-sectional area. An average of five determinations was computed.

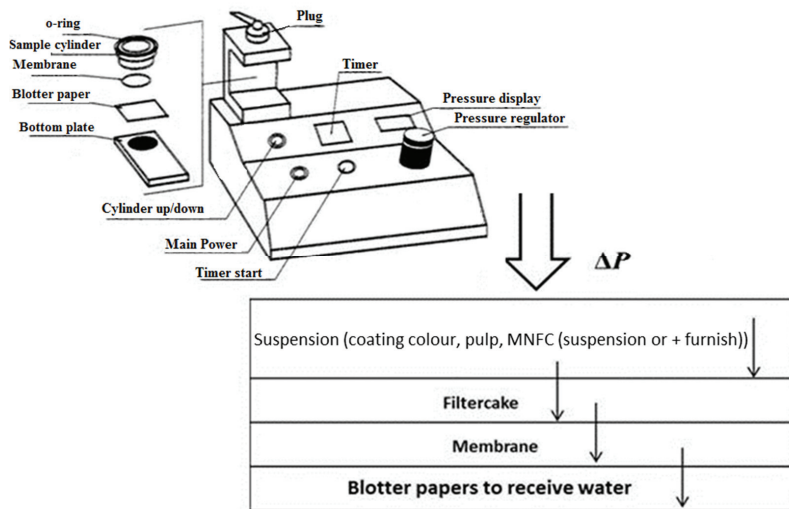


Figure 25 Gravimetric water retention device *AA-GWR* / Modified from reference (Bousfield *et al.* 2008)/.

3.2.7 Rheometry

The viscoelastic rheological investigations were performed at 23°C by means of an Anton Paar 300 Rheometer with oscillatory constant stress/strain and variable shear device using plate-plate geometry. For MNFC measurements, a serrated plate geometry was used, with a plate-plate gap of 2.3 mm, while for coating colours a smooth plate geometry was employed, and the gap between upper and bottom plate was 1 mm. The upper plate diameter for both smooth and serrated geometry was 25 mm. In order to obtain reproducible results, since viscoelastic behaviour in these materials is subject to the memory of shear history imposed upon them, a specifically defined pre-shearing protocol was set each for both MNFC suspensions, furnishes and coating colours.

The MNFC samples were pre-sheared at $\omega = 10 \text{ s}^{-1}$ and $\gamma = 0.1 \%$ for 10 min, followed by a rest stationary state time of 15 min. The coating colours were pre-sheared at a shear rate $\dot{\gamma} = 300 \text{ s}^{-1}$, for 10 s, and equilibrated for 200 s.

To prevent evaporation of the water medium, a thin layer of silicone oil was spread over the surface of the sample (Barbesta *et al.* 2001, Moan *et al.* 2003). Different types of rheological measurements were performed on the same rheometer, preserving the geometry: viscoelastic measurements, stability and recovery tests constant shear rate measurements, steady state flow with increasing shear rate.

3.2.8 Dynamic dewatering with the Immobilisation Cell (IMC)

Rheological observation of a sample during filter cake formation is very important, as continual removal of water alters the material flow properties.

Due to the complexity of the phenomenon, increasingly realistic laboratory tests are proposed to simulate and optimise dewatering processes (Willenbacher *et al.* 1999) IMC allows determination of rheological properties of sample while the sample goes through the liquid to solid phase transition (Jäder and Järnström 2001, Jäder and Järnström 2003, Pajari and Koskela 2010, Bousfield *et al.* 2008). In this thesis we are observing immobilisation of two different coating colour systems, traditional coating colours including mechanical interlocking under the influence of flocculation, and gel-like novel coating colours and furnishes.

Termed an immobilisation cell (IMC), it is used as an accessory to a stress controlled rotational type of rheometer. The IMC, Fig. 26 provides a horizontal porous surface through which a sample is filtered. The IMC consists of a stainless steel cylindrical metal tube with a punched metal plate that allows drainage of water through the filter by vacuum suction (Willenbacher 2011, Wollny 2001). The filter medium used in these experiments was a hydrophobic Whatman Nucleopore membrane, with a pore size of 0.2 μm . A filter is fastened on the top of the punched metal plate and the sample to be investigated is applied on the top of the filter. The dynamic dewatering measurement was conducted using the Physica MCR 300 rheometer with IMC accessory as licensed from BASF-AG. Varying the gap width, applied vacuum and shear stress can simulate different processing conditions. During the process, the rheological properties of the accumulating solids layer of the sample are determined with a plate–plate geometry sensor which is adjusted vertically for constant normal force. The parallel smooth plate diameter of 50 mm (PP-50) was adopted in all immobilisation tests, as standard procedure the initial gap was set to 1 mm. In the experiments, the temperature was kept at 23°C and the pre-set shear rate was 100 s^{-1} applied for 40 s. The upper plate is then lowered into contact with the sample, which is then pre-sheared. The normal force from the sample tends to act to push the upper rotating plate away from the lower plate. The axial force acting on the upper plate is set to a constant value (here to 0) (Jäder and Järnström 2003), the upper plate moves down, thus decreasing the gap between the plates, i.e. compensating for the dewatered volume of the filtrate.

Two testing approaches can be applied with the IMC: the controlled shear rate (CSR) (Willenbacher *et al.* 1998) and the direct strain-controlled oscillatory (DSO) (Wollny 2001) method. The $\tan \delta$ marks the transition of liquid-like to solid-like behaviour during dewatering (Wollny 2001). However, during the CSR tests, the viscoelastic properties cannot be determined, instead only the change in η is able to be monitored (Ayol *et al.* 2010). The outer part of the sample within the gap is always at lower solids than the centre part due to the growth of a solids content gradient within the gap, as was determined in previous work with optical fibres (Wollny 2001). Therefore, due to this inhomogeneity, the measured viscosities (η and η^*) are apparent values that display an increase with time.

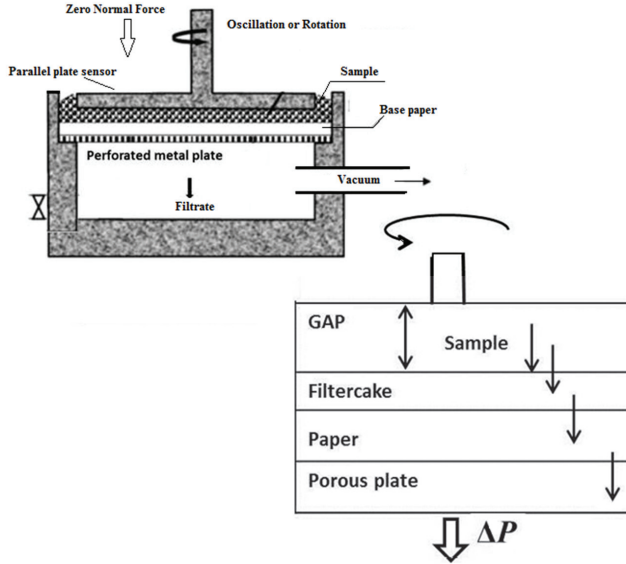


Figure 26 Immobilisation cell IMC at MCR 300 rheometer/ Modified from reference (Bousfield *et al.* 2008)/.

3.2.9 IMC measurement

3.2.9.1 Oscillation mode (DSO)

The oscillatory measurements have an advantage over rotational measurements (CSR) in that the sample structure is not affected while performing the measurement at the immobile condition. Wollny (Wollny 2001) defined in DSO tests three mechanistic ranges which can be observed in the immobilisation process. When a difference in pressure is applied (vacuum dewatering), the liquid volume decreases and the concentration gradient build within the sample can be seen through the increase of elastic modulus (G') in relation to the viscous modulus (G'') (Laudone *et al.* 2006, Waalström and Järnström 2007). In respect to this Wollny (Wollny 2001) described immobilisation through the three distinct ranges by monitoring the development of $\tan \delta$. As the filter cake is already forming on the filter medium, below the rotating measuring system, elasticity increases thus decreasing $\tan \delta$. Therefore time of onset of immobilisation t_{ip} is at maximum $\tan \delta$. The point of immobilisation is marked as time t_i , where $\tan \delta \rightarrow 0$, with $G' \gg G''$, being the indication of the filter cake being in its immobilised but saturated condition, Fig. 27a). Wollny (Wollny 2001) defines degree of immobilisation, Fig. 27b) as

$$X_i = \frac{l_0 - l_e}{l_0 - l_t} \quad (49)$$

where l_0 is the initial measuring gap, l_e is the effective measuring gap, and l_t is the measuring gap when the immobilisation time is reached Fig. 27b).

3.2.9.2 Rotation mode (CSR)

Semi-log plots of dynamic viscosity-time curves exhibit a characteristic shape with a linear increase in η at short time span and a sharp upward curvature when reaching the immobilisation point t_i . With CSR dewatering mode using the IMC, Willenbacher *et al.* (Willenbacher 1999) defined t_i from semi-log viscosity-time rheograms as the intersection of the tangents to the two branches of the viscosity against time curve Fig. 27c). Later on the same approach was used by Ayol *et al.* (Ayol *et al.* 2010) for immobilisation of sludge.

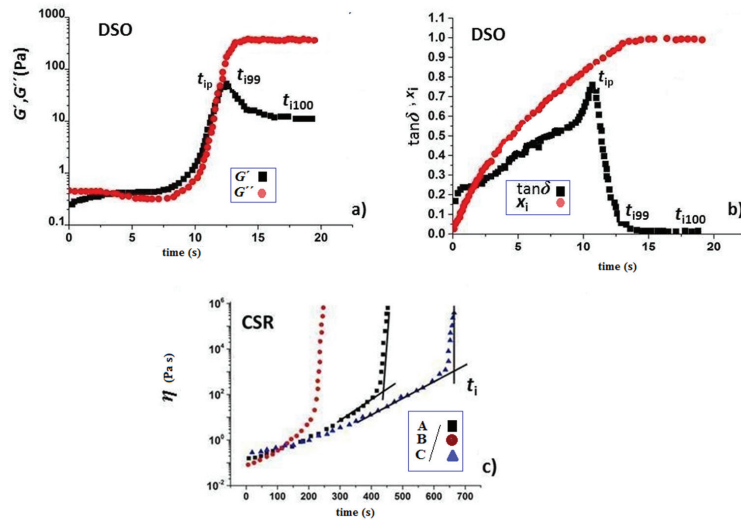


Figure 27 Typical change of rheological parameters on the IMC device, and methods for determination of immobilisation time of paper coating colour t_i /Modified from references/ a) immobilisation in DSO as change of viscoelastic moduli (G' and G'') (Wollny 2001), b) transition from supersaturated suspension to the immobilised condition (Wollny 2001), and c) increase in dynamic viscosity during immobilisation and determination of immobilisation time t_i with the tangent method, presented for three different coating colours A, B and C (Willenbacher 1999).

3.2.9.3 Theory behind the IMC measurement

In the IMC dewatering measured with CSR, the decrease of liquid volume of the sample can be measured by monitoring the gap height and thereby through the change in η the immobilised and non-immobilised volume of the sample within the geometry.

In dewatering experimental conditions, when the coating colour is dewatered, the results include the resistance of the immobilised layer to flow and display the concept of delayed cake build-up, which subsequently was defined by Jäder (Jäder and Järnström 2001) in terms of the normalised apparent cake thickness l_{FC}^* , defined as the filtercake length per unit volume of filtrate extracted, having units of m^{-2} , given by

$$l_{FC}^* = \frac{l_{FC}}{V_{IMC}} = \frac{v_{FC}}{A_{IMC}} \quad (50)$$

where v_{FC} again denotes the apparent volume of cake deposited over the cross sectional area of the IMC, A_{IMC} . The filtrate volume is V_{IMC} and the filter cake length is l_{FC} .

Without delayed cake build-up, l_{FC} is equal to $(V_{IMC}v_{FC}/A_{IMC})$, and using the assumption that l_{FC} can be approximated as permeation sample length L , and k_{FC} permeability coefficient of the filter cake Eqs. 34 and 37, then Eq. 51 can be re-expressed (Jäder and Järnström 2001, Pajari and Koskela 2010, Usher *et al.* 2001) to obtain the connection between filtration rate $d(V_{IMC}/A_{IMC})/dt$, to give ϕ_{cc} the solids volume fraction in the coating colour and ϕ_{FC} the solids volume fraction of the filter cake at a given t , the time toward forming the filter cake (FC) as follows

$$\left(\frac{V_{IMC}}{A_{IMC}} \right) = \sqrt{2 \left(\frac{k_{FC}}{\eta_{FC}} \right) \left(\frac{\phi_{FC} - \phi_{CC}}{\phi_{CC}} \right) t \Delta P} \quad (51)$$

This method can give experimental correlation with gravimetric dewatering results, if it is assumed that the same ΔP is applied for both measurements as both tests are long time dewatering methods with formed filter cake affecting dewatering results, such that $V_{IMC}/A_{IMC} \approx V_{AA-GWR}/A_{AA-GWR}$, (Jäder and Järnström 2001, Pajari and Koskela 2010, Bousfield *et al.* 2008).

Based on the modified differential equation which models the filtration behaviour of compressed networked suspensions, it has been proposed in other work on coating colour dewatering and immobilisation that the following relation holds between gravimetric dewatering obtained from the static AA-GWR dewatering device, and immobilisation interval ($t_i - t_{ip}$) obtained from the dynamic IMC dewatering device

$$(V_{AA-GWR}/A_{AA-GWR}) \sim \frac{1}{\sqrt{t_i - t_{ip}}} \quad (52)$$

3.2.10 Tablet forming (Publication V)

In order to obtain macroscopic liquid flow for ease of measurement, tablet structures of the coating pigments and formulated colours were formed by applying a constant pressure to the suspension/colour for up to 24 h such that water was released by filtration through a fine 0.025 μm filter membrane resulting in a compacted tablet, in a method developed by Ridgway (Ridgway *et al.* 2003) and shown as applied by Gerstner (Gerstner 2010) in Fig. 28, (Publication V).

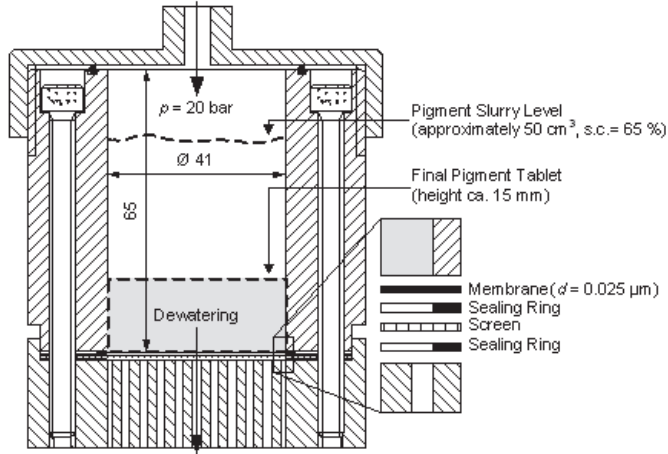


Figure 28 Tablet forming apparatus / Adopted from reference (Gerstner 2010)/

3.2.11 Mercury intrusion

Mercury intrusion measurements on the tablet structures were made using an Autopore IV mercury porosimeter (Micromeritics Instrument Corporation, Norcross, GA, U.S.A.) (Publication V). The maximum applied pressure of mercury is 414 MPa, equivalent to a Laplace throat diameter of 4 nm. The equilibration time at each of the increasing applied pressures of mercury is set to 60 seconds. It is vital that the mercury intrusion measurements be corrected for the compression of mercury, expansion of the penetrometer and compressibility of the solid phase of the sample. This is performed conveniently using the software Pore-Comp (a software program developed by and obtainable from the Environmental and Fluids Modelling Group, University of Plymouth, U.K.), in which the following equation (Gane *et al.* 1996) is applied

$$V_{\text{int}} = V_{\text{obs}} - \delta V_{\text{blank}} + \left[0.175(V_{\text{bulk}}^1) \log_{10} \left(1 + \frac{P}{1820} \right) \right] - V_{\text{bulk}}^1 (1 - \Phi^1) \left(1 - \exp \left[\frac{(P^1 - P)}{M_{\text{ss}}} \right] \right) \quad (53)$$

where V_{int} is the volume of intrusion into the sample, V_{obs} the intruded mercury volume reading, δV_{blank} the change in the blank run volume reading, V_{bulk}^1 the sample bulk volume at atmospheric pressure, P the applied pressure, Φ^1 the porosity at atmospheric pressure, P^1 the atmospheric pressure and M_{ss} the bulk modulus of the solid sample

Since the application of high pressure is required to force the intrusion of mercury several instrumental corrections are required to account for the compression of mercury and the expansion of the penetrometer vessel. In the case of coating colours, there are compressible materials comprising the skeletal structure, such as latex binder and polymers (Gane *et al.* 1996).

3.2.12 Liquid absorption apparatus

The accessible porous volume of the tablet structures can be measured by absorbing chemically non-interacting liquid, hexadecane, using the apparatus used to determine absorption dynamic was described previously in more detail in Schoelkopf *et al.* (Schoelkopf *et al.* 2000) and is shown schematically in Fig. 29. In the case of evaporative liquids, such as water and solvent, the evaporation rate within the enclosed vapour saturated cabinet is recorded over time, and the linear function used to correct the experimental absorption data by subtraction.

To reduce artefacts caused by the wetting of their outer surfaces, samples were coated with a thin barrier line of silicone around the base of the vertical edges arising from the basal plane. The remainder of the outer planes were not coated, to allow for the free movement of displaced air or liquid during absorption, and to minimise any interaction between the silicone and the absorbed liquid. A liquid supersource reservoir is provided by the liquid held in a dish which is placed on the weighing area of the balance. Once the sample is lowered to contact the absorbing fluid source, the weight loss from the dish is continually recorded using an automated microbalance, namely a PC-linked Mettler Toledo AT460 balance with a precision of 0.1 mg, capable of 10 measurements per second. When the recorded weight is constant, indicative of absorption-saturation, the measurement is complete. Knowing the sample weight before and after the absorption measurement allows the intruded volume per gram of sample to be calculated (dividing the weight difference by the density of the liquid gives the volume intruded into the sample, and hence the volume per gram of sample) (Publication V).

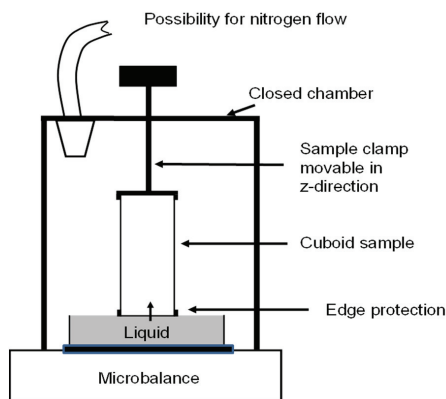


Figure 29 Liquid absorption experimental apparatus /Adopted from reference (Schoelkopf *et al.* 2000)/.

The distance of the visible wetting front from the sample base, l , in relation to the total sample height, L , was recorded, and weight differences, before and after the uptake, used to define the specific pore volume filled up to the wetting line (Ridgway *et al.* 2006, Schoelkopf *et al.* 2000) Fig. 30.

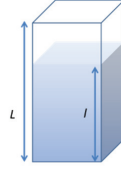


Figure 30 Schematic of partially filled tablet after 48 hours absorption - observed absorption length, l , shown.

The absorption experiments with water were run twice, with a drying step in between. After the water absorption was initially measured for 48 hours ($n = 1$, first absorption experiment), the samples were dried in an oven at 60 °C overnight and measured for absorption a second time for a further 24 hours ($n = 2$, repeated absorption experiment). The ratio of pores filled by the absorbing liquid (liq(n), where n describes the wetting order – 1st versus 2nd absorption experiment) into the tablet within the wetting distance, $V_{\text{liq}(n)}$, compared with the available pores in that same portion of the original unwetted sample, determined by mercury porosimetry, $V_{\text{Hg}(l)}$, is calculated by

$$\frac{V_{\text{liq}(n)}}{V_{\text{Hg}(l)}} = \frac{(m_{\text{after absorption}(n)} - m_{\text{dry}}) / \rho_{\text{liq}}}{V_{\text{Hg}(L)} l / L} \quad (54)$$

where

$$V_{\text{Hg}(L)} = \varphi_{\text{Hg}} m_{\text{dry}} \quad (55)$$

is the total pore volume of the sample, φ_{Hg} is the specific pore volume of the sample as determined by porosimetry, m_{dry} is the mass of the tablet before absorption and parameter $m_{\text{after absorption}(n)}$ is the weight after the respective absorption experiment. In the first absorption ($n=1$), the experiment time lasted 48 h, and the second absorption ($n=2$) absorption time, after intermediate drying, was 24 h. The liquid density is ρ_{liq} (water in this case, and the same for the first and second absorption), l is the observed absorption length of the given absorption into the tablet sample, and L is the total length of the tablet sample.

3.2.13 Permeability measurement cell

The cell design used for the pressurised permeability experiments has been fully described elsewhere (Ridgway and Gane 2003) and was used in this thesis for the determination of the permeability of the tablet samples (Publication V). A cuboidal piece of the tablet structure similar to that used for the absorption measurements into a mould (Prüfmaschinen AG, Giessenstr. 15, CH-8953 Dietikon, Switzerland), having an inner diameter of 30 mm. Resin (EpoThin Epoxy, Buehler, CH-8952 Schlieren, Switzerland) is then poured around it, Fig. 32, to form a rigidly held mounted sample in cylindrical form (Schoelkopf *et al.* 2000, Ridgway *et al.* 2006). The sample is then saturated with the chosen liquid. The resin-mounted sample is then placed in the pressure vessel, and a liquid reservoir head is added above the sample. Over-pressure is then supplied from a nitrogen bottle. The pressure cell is fixed over a microbalance and a PC samples the balance data using specially-developed software developed within Omya AG. A drop

captor device is placed at the base of the cell to collect the permeated liquid drops directing them by surface tension to the outlet. The embedded blocks of tablets were left to absorb water and hexadecane for three days, a time well sufficient for tablet structures to reach saturation.

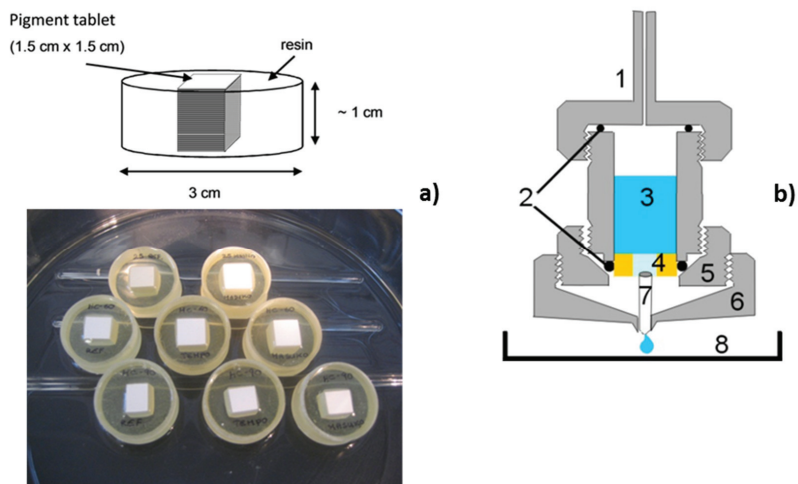


Figure 31 Permeability measurement: a) preparation of the sample and liquid saturation, b) permeability measurement cell 1) lid with pressure inlet, 2) sealing O-rings, 3) liquid cell; outer diameter = 40 mm, 4) porous sample embedded in resin disc of diameter = 30 mm as presented in Fig. 31a, 5) fixing ring compresses the O-ring which seals the resin disc, 6) security shroud and drop collector, 7) drop captor (Teflon tubelet), 8) dish on micro-balance. / Modified from reference (Ridgway *et al.* 2003)/.

3.2.14 Additional measurements

Fourier-transform infrared (FTIR) spectroscopy in the attenuated total reflection mode (Perkin Elmer Spectrum One, Perkin Elmer, CH-8603 Schwerzenbach, Switzerland) is used for determination of extracted material from pigment structures containing MNFC (Nuopponen *et al.* 2003, Pandey 1999) (Publication V).

Scanning electron microscopy (SEM) (Philips SEM 515, Type PW6703, Philips Optical Electronics, Eindhoven, Netherlands) images were taken of a clean broken surface of the tablets (Gane *et al.* 2004, Poehler *et al.* 2006) (Publication V).

Table 6 summarises the descriptions of all the measurements applied in the thesis.

Table 6 Schematic description of all measurements and methods used in this thesis.

Measurement device	Suspension	Parameters of measurement	Properties of material learned
ÅA-GWR gravimetric dewatering device	MNFC suspensions coating colours furnishes	Gravimetric dewatering at $\Delta P = \text{constant}$ As filtrated water ($\text{g water} \cdot \text{m}^{-2}$) on blotter paper (Publications I-V)	Water retention value at static dewatering conditions
WRV test ISO/DIS 23 714	MNFC/pulp suspensions coating colours	WRV value of furnish cake with (0- 6%) content of MNFC ($\frac{\text{g water}}{\text{g MNFC}}$) (Publications I-VI)	Swelling of MFC and NFC
DSC Differential Scanning Calorimeter	MNFC suspensions	Difference between ΔH_{ml} of MFC/NFC samples and bulk water from $-50^{\circ}\text{C}/-0.2^{\circ}\text{C}$ and $-50^{\circ}\text{C}/+20^{\circ}\text{C}$ to obtain W_f, W_b (Publications I-VI)	Quantity of bound and free water
Brookfield viscometer (Brookfield DV-II+)	MNFC suspensions coating colours furnishes	Apparent viscosity η_v spindle #4 (coating colours) spindle V-73 and V-74 (MNFC) At 0.1, 0.2, 2, 10, 20, 45, 50, 100, 200 min^{-1} (Publications I, III, IV, V, VI) $\eta_v, \lambda_{\text{H}}, \tau_{0(\text{H})}^v$ (Publication VI)	Small shear rate apparent viscosity
Zeta sizer Malvern Instruments Ltd. Zeta potential	Pigments, latex, CMC; pulp MNFC suspensions	Zeta potential ζ (mV) (Publications I-VI)	Electrokinetic potential of colloidal systems; Stability of MNFC
Zeta sizer Malvern Instruments Ltd. Dynamic Light Scattering	pigments, latex, CMC, MNFC suspensions	Dynamic light scattering (DSL) (Publications I-VI)	Average: particle size /agglomerate size
Micromeritics TriStar II Micromeritics N.V./ S.A	Pigments	Specific surface area of the pigments with nitrogen adsorption methods, as surface area / unit weight of sample (Publications III-V)	Specific surface area of pigments
Sedigraph Macromeritics, Georgia	Pigments	Sedimentation of pigments (Publications III-V)	Pigments particle size
pH meter	Pigments, latex, CMC, MNFC suspensions coating colours, pulp furnishes	Fillers, MFC/NFC suspensions, coating colours, CMC, latex furnishes (Publications I-VI)	Acidity - alkalinity of samples
Amplitude sweep : Direct oscillation mode DSO	MNFC suspensions, coating colours furnishes	$G', G'', \eta^*, \tan \delta, \tau_0^s, \tau_0^s$ $\gamma = 0.01-500 \%$ (Publications I, II, III, IV)	Rheological properties of suspensions within and outside LVE
Frequency sweep : Direct oscillation mode DSO	MNFC suspensions coating colours	$G', G'', \eta^*, \tan \delta_1$ $\omega = 0.01-100 \text{ s}^{-1}$ (Publications I, II, III, IV)	

3ITT (viscosity) Shear mode CSR/CSR/CSR	Coating colours	$\dot{\gamma}, \eta$ $\dot{\gamma} / \dot{\gamma} / \dot{\gamma} = 0,1 \text{ s}^{-1} / 500 \text{ s}^{-1} / 0,1 \text{ s}^{-1}$ (Publication III, IV)	Time that structure recover 90% of first interval viscosity
3ITT (elasticity) Direct oscillation mode DSO /CSR/DSO	Coating colours	G' $\dot{\gamma} / \dot{\gamma} / \dot{\gamma} = 0.01 \% / 500 \text{ s}^{-1} / 0.01 \%$ (Publications III, IV)	Time that structure recover 90% of first interval elasticity
IMC Direct oscillation mode DSO Rotation mode CSR	MFC/NFC suspensions coating colours paper making furnishes	$G', G'', \eta^*, \tan \delta$; $\omega = 10 \text{ s}^{-1}, \dot{\gamma} = 0.01 \%$ or η for $\dot{\gamma} = (0/40/200) \text{ s}^{-1}$ (Publications I, II, III, IV)	Change of viscoelastic parameters as a function of solid content increase
Pressure vessel	Coating colours	Coating slurry dewatering through a membrane $D = 0.025 \text{ mm}$ by applying pressure $P = 20 \text{ bar}$ (Publication V)	Formation of coating colour tablets
Absorption Dynamics Measurement	Tablets made from coating colours	Absorption rate of water/hexadecane (Publication V)	Absorption curves during liquid uptake (long/short)
Scanning Electron Microscop SEM	Tablets made from coating colours	The SEM images from tablets which had MNFC as co-binder (Publication V)	Images of aggregation and orientation of fillers with presence of MNFC
Mercury Intrusion Autopore IV (Micrometrics Instrument Corporation, Norcross)	Tablets made from coating colours	Porosity distribution with mercury penetration with applied pressure $P = 414 \text{ MPa}$ for $t = 60 \text{ s}$ (Publication V)	Pore volume of coating colour tablets as a function of effect of MNFC
Tablet Permeability Measurement (Onya)	Tablets made from coating colours	Permeability of the tablet samples after saturation with water/ hexadecane (Publication V)	Permeability of coating colour tablets as a function of effect of presence of MNFC as co-binder

4 Experimental

In **Part I** of the following experimental discussion, the rheological and dewatering behaviour of nanocellulose containing MNFC and pulp suspensions are considered, with particular attention to the use of MNFC as additive in papermaking suspensions. **Part II** then describes studies made on two types of papermaking suspensions, (i) wet end furnish, and (ii) coating suspensions. In each case the material interactions when MNFC is used progressively to replace fibre in case (i), and traditional water retention aids in coating colours in case (ii), act to highlight the contrasting effects of soluble polymers, such as CMC, and the nanocellulose gelation properties manifest by MNFC.

4.1. Part I: Rheological analysis of MNFC suspensions

4.1.1 Viscometry, oscillatory rheometry and gravimetric dewatering

As presented in Table 1 and Table 2, one single type of MFC and two types of NFC were used for the purpose of study in this thesis. Apparent low shear viscosity results from Brookfield viscometry are presented in Table 7 show that shear viscosity under the vane geometry is higher for MFC than for NFC suspensions over a range of low three shear rates (Publication III and IV).

Table 7 Results of low-shear apparent viscosity (Brookfield) for MFC/NFC (Publication III and IV).

MNFC suspensions	MFC	NFC ¹	NFC ²
Consistency (%)	1.5	1.5	1.5
$\eta_v @ 10 \text{ min}^{-1}$ (mPas)	151 768	74 334	76 563
$\eta_v @ 50 \text{ min}^{-1}$ (mPas)	53 268	16 345	19 548
$\eta_v @ 100 \text{ min}^{-1}$ (mPas)	33 666	9 987	10 615

Data obtained from the oscillation measurements of MNFC suspensions are presented in Figs. 31a-c). Storage (G') and loss (G'') moduli were measured for MFC and NFC¹ suspensions as 1.5, 2 and 2.3 % concentrations. Both the G' and G'' increase with increasing concentration, confirming the viscoelastic character of the suspensions (Iotti *et al.* 2011, Saito *et al.* 2006). Fig. 31a) shows that for fibrillar material containing MFC suspensions, G' within the linear viscoelastic region (LVE) is higher than that of NFC¹ suspensions, the latter having effectively higher swelling in respect to the adsorbed water properties, Table 1.

The critical strain (γ_c) for NFC¹ is further extended to a higher value (critical strain for MFC suspensions being $\gamma_c \sim 0.015$ %, while for NFC¹ suspensions $\gamma_c \sim 0.8$ %), due to a stronger gel-like structure typical for NFC suspensions at concentration levels higher than 1 % (Iotti *et al.* 2011, Saito *et al.* 2007) (Publication III). Similarly, gel-like behaviour is observed from frequency sweep measurement Figs. 30b) and c), and the difference between G' and G'' is held quite similar in absolute terms across the different concentrations, for both MFC and NFC¹. We also see that G' shows little to no dependence on frequency throughout the measured frequency range (even more pronounced for NFC¹), but the viscous moduli G'' show a slight increase toward higher frequency, with the loss factor ($\tan \delta$) being around 0.2 with G' being an order of magnitude higher than G'' , indicating gel-like structure (Gisler *et al.* 1999, Persello *et al.* 1994, Corrêa *et al.* 2010).

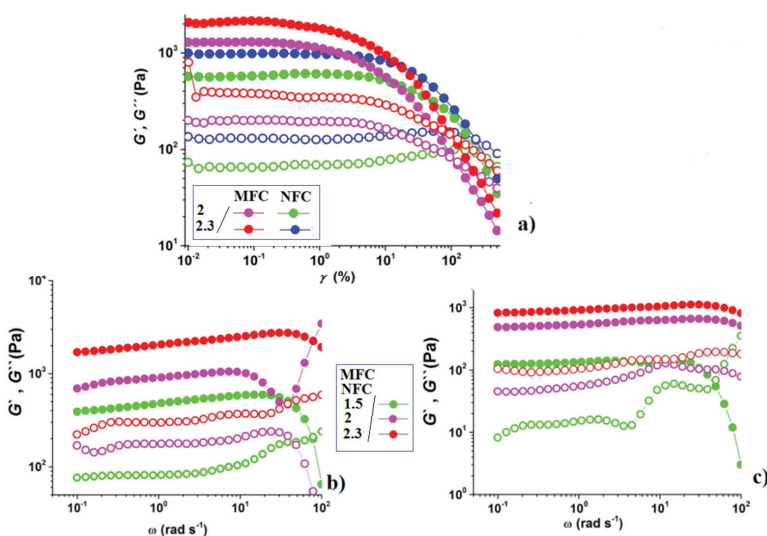


Figure 30 Viscoelastic measurements for MFC and NFC¹ suspensions at 1.5 %, 2 % and 2.3 % consistency: a) amplitude sweep for a range of strain ($\gamma = 0.01$ -500 %) at constant angular frequency of 1 (rad)s⁻¹, (Publication III), b) frequency sweep (0.1-100 (rad)s⁻¹) at constant strain of 0.1 %. Elastic modulus (G') closed symbols, loss modulus (G'') open symbols (Publication I).

The WRV curves, used to describe the effective water retaining properties, at different MNFC content show non-linear behaviour, which is most obvious in the case of NFC, as the pad formed during dewatering becomes too impermeable and can no longer be effectively dewatered in a centrifuge. This reduced permeability is traditionally interpreted as increased tortuosity due to fines content (Chen *et al.* 2009, Hubbe 2007). As we shall see in later analyses, the situation is different in the case of MNFC containing suspensions as the nanocellulose fraction forms a gel which then retains water and establishes a non-permeable structure (Klemm *et al.* 2009, Manninen *et al.* 2013, Taipale *et al.* 2010). Therefore, the best estimate of the water holding capacity of the MNFC in non-gel form can be obtained at low solids content. For this, the WRV at 2 % MNFC content was used. The apparent WRV for 0 % MNFC can be estimated from Fig. 31a), giving a value of 24 g_{water} g⁻¹ for NFC and 9 g_{water} g⁻¹ for MFC (Publication II).

Fig. 31b) presents G' at $\omega = 16 \text{ rad s}^{-1}$ obtained from the frequency sweep data for MNFC suspensions as an average value derived by conducting five measurements (Publication I), together with the measured value of ζ . Lower G' and G'' for NFC suspensions, which have higher ζ , reflect the effect of bound water, i.e. seen as effective swelling, on the mobility by reducing friction between the nanocellulose particulates, and so supporting the WRV results (Hatakeyama *et al.* 2012, Uetani and Yano 2011). Gravimetric dewatering results presented at Fig. 31c) show that smaller NFC with its higher amount of bound water, and three times higher WRV, has much greater water retention properties than the longer more flocculated and lower surface charge MFC. Pulp suspensions used as reference comparisons show naturally the lowest surface charge, Table 1, and exhibit the lowest water retention due to flocculation induced by long pulp fibres, which in turn induces phase separation.

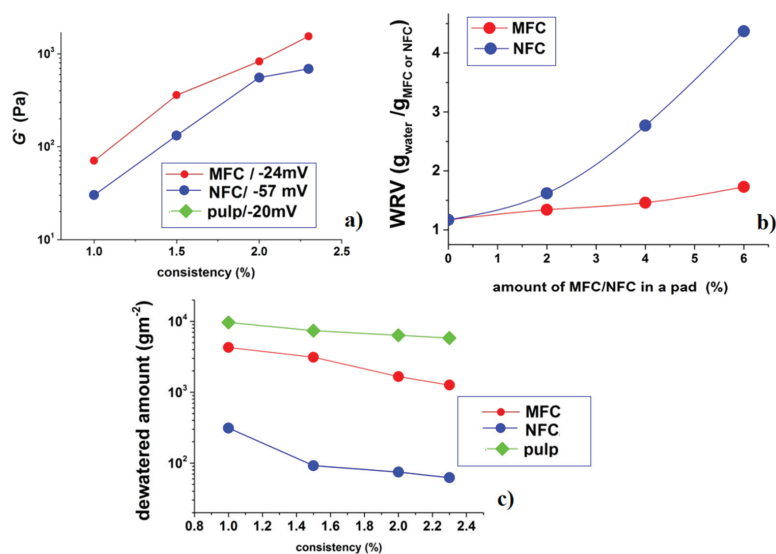


Figure 31 a) WRV curves of Kraft pulp pads with varying MFC and NFC¹ content (Publication II), b) MFC and NFC¹ (pulp fibres G' not presented due to difficulties in measurement with profiled geometry) suspensions at 1 %, 1.5 %, 2 % and 2.3 % consistency G' at $\omega = 16 \text{ rad s}^{-1}$ obtained from frequency sweep measurements together the respective material ζ (Publication I), c) gravimetric dewatering results for MNFC and pulp suspensions at 1 %, 1.5 %, 2 % and 2.3 % consistency (Publication I).

Similar rheological curves in oscillation measurements for different nanocellulose types, namely MFC and NFC², are also seen to be a function of suspension consistency and relative MNFC swelling/water binding efficiency, as concluded previously, which is observable in Figs. 32a-d) (Publication IV).

As presented earlier, G' and G'' at fixed strain ($\gamma = 0.2\%$) for the MFC suspensions are higher than for the NFC² suspensions, Fig. 32d), due to the likelihood of MFC fibril entanglement, Table 1.

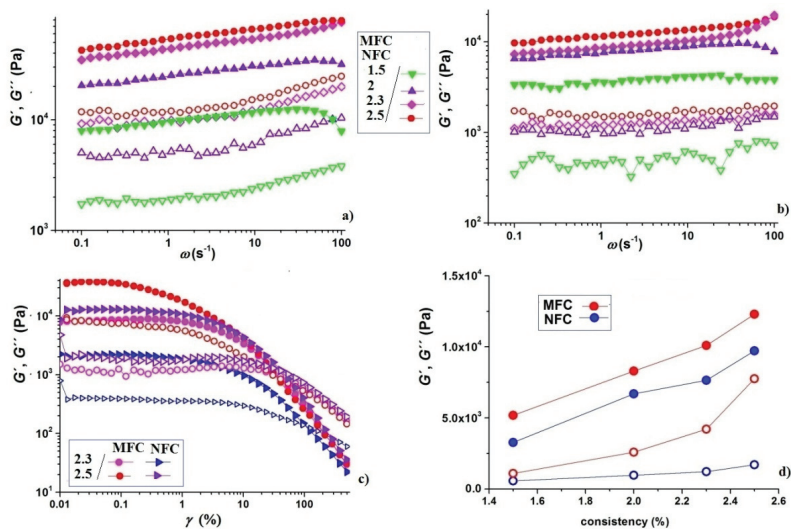


Figure 32 G' (filled symbols) and G'' (unfilled symbols) of MFC and NFC² suspensions as a function of angular frequency ($\omega = 0.01-100\text{ s}^{-1}$) and strain ($\gamma = 0.01-500\%$): a) frequency sweep MFC suspensions, b) frequency sweep NFC¹ suspensions, c) strain sweep MFC and NFC¹ suspensions, d) viscoelastic moduli G' and G'' at $\gamma = 0.2\%$. All samples are labelled with their respective consistencies (Publication IV).

MNFC suspensions have complex thixotropic behaviour, which can be observed as dependence of rheometer torque (M) at constant low shear rate $\dot{\gamma} = 0.01\text{ s}^{-1}$ evolving over a long measurement time ($> 7\,000\text{ s}$), Fig. 34 (Publication IV). Torque (M) is seen to fail to settle to a steady equilibrium value even after very long measuring times due to the rheological time dependency related to wall slip and phase separation, causing shear banding profiles at low shear rates (Divoux *et al.* 2013, Puisto *et al.* 2012, Saarinen *et al.* 2010).

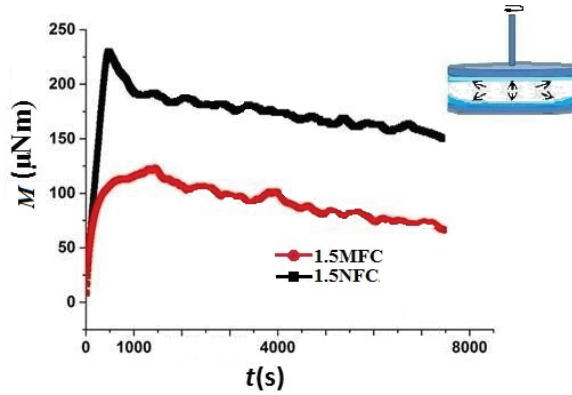


Figure 33 Torque against time t for a shear rate of $\dot{\gamma} = 0.01 \text{ s}^{-1}$. Despite the profiled boundary, we can observe a fluctuating close to oscillatory shear condition linked to the consequences of periodic wall slip for both MFC and NFC² (schematic) (Publication IV).

The Herschel-Bulkley equation does not apply very well across the whole shear stress profile due to the elastic overshoots Figs. 34 a)-c) (Divoux *et al.* 2010, Iotti *et al.* 2011, Puisto *et al.* 2012a, Puisto *et al.* 2012b). Elastic overshoots observed in Fig. 34c) for higher consistencies are due to the elasticity of the gel-like network of NFC¹, which also causes the phase separable wall slip effect at the plate-plate geometry.

Therefore, for Herschel-Bulkley fitting at steady state flow curves only the data within the shear rate region between 20 and 500 s^{-1} are used, Fig. 34b), following the procedure described by Karppinen *et al.* (Karppinen *et al.* 2011) as presented in Fig. 34c). As expected, for all solids, the yield stress increases with increase in suspension consistency, as also observed before by other authors (Richmond 2012).

At lower consistency, the yield stress is almost the same for MFC and NFC¹ suspensions, for consistencies greater than 1.5 %, increasing drastically for NFC¹, due to the inhibited hydrogen bonding of higher specific surface area NFC¹ which gives rise to gel-like structures, Fig. 34a).

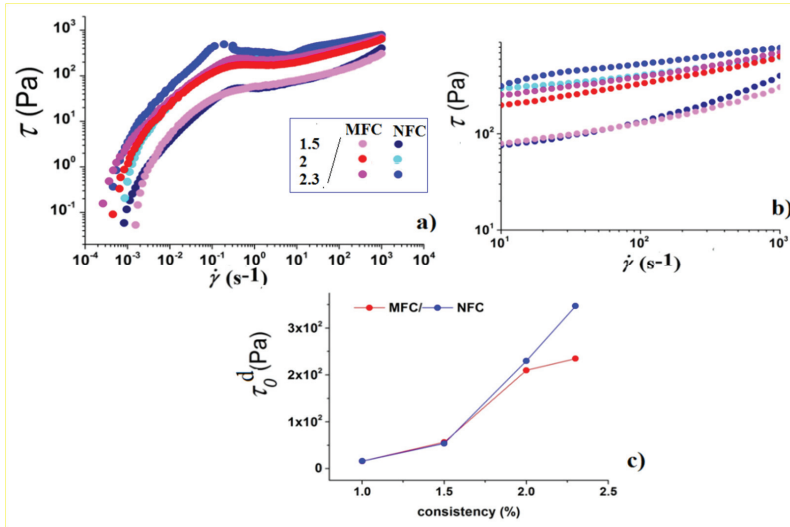


Figure 34 Steady state flow curves for MNFC suspensions for shear rate ($\dot{\gamma} = 0.001 - 1000 \text{ s}^{-1}$), time between points 10 s: a) shear stress (τ^d) against shear rate ($\dot{\gamma}$) over the whole shear rate range, b) shear rate region for determination used for data fitting into Herschel-Bulkley model, and c) apparent yield stress (τ_0^d) for MFC and NFC¹ suspensions as a function of consistency (Publication III).

In Figs. 35a-d) is shown the dependence of stress of MFC and NFC² on strain, for both oscillatory and steady state measurements. The span of the static and dynamic stress values for the MFC is greater than that of the NFC² as a function of consistency, as presented through apparent static yield point values (τ_0^s) at the crossing point of the tangents from the elastic strain (τ^s) curves Figs. 35a-b), and apparent dynamic yield point τ_0^d determined by the Herschel-Bulkley fit Fig. 35c). Scatter in data between yield stress obtained by oscillation and steady shear measurements, Fig. 35e), has been observed before, where apparent yield stress obtained by quasi-static methods tend to be larger than those measured using dynamic methods ($\tau_0^s > \tau_0^d$) (Derakhshandeh *et al.* 2011, Walls *et al.* 2003). Increase of yield stress with consistency (Horvath and Lindström 2007), more pronounced for NFC² than for MFC, is observed as illustrated in Fig. 34.

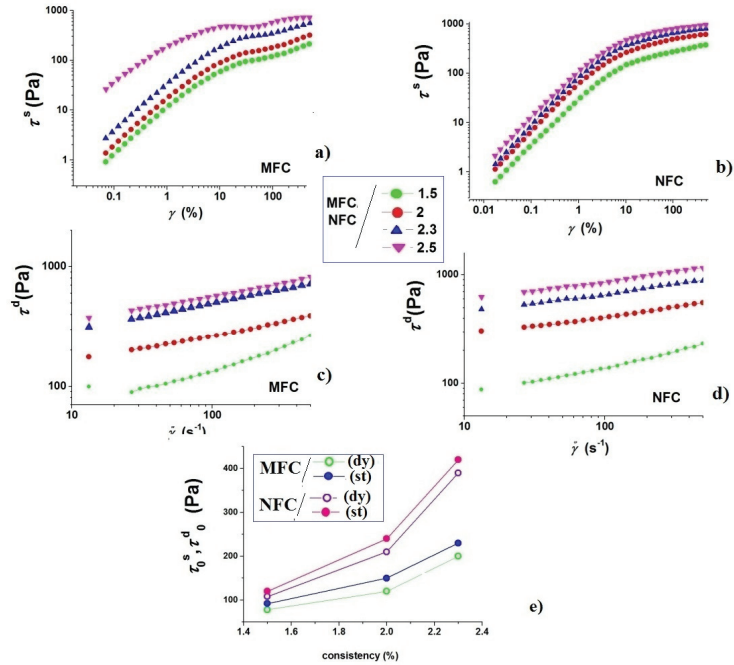


Figure 35 Determination of stress using oscillatory and steady shear flow: elastic stress-strain dependence for a) MFC suspensions, and b) for NFC² suspensions. Herschel-Bulkley model (Eq. 24) fitted to flow curves for c) MFC suspensions, and d) NFC² suspensions, to determine e) the static yield stress (τ_0^s) and the dynamic yield stress (τ_0^d) as a function of consistency and type of nanocellulose; the labels (dy) stand for the dynamic viscosity condition, and (st) for static viscosity condition (Publication IV).

Application of correction method for the determination of $\dot{\gamma}$ from Eq. 46 with wide gap vane bucket geometry compared to that given by Eq. 45 is proposed in Publication VI. Here are reported the flow curves for both the MFC and NFC¹ in Figs. 36a) and b). Comparison of the standard reported flow curves using a narrow gap approximation (protocol obtained from the device, Eq.46) with those of the corrected ones (corrected protocol, Eq.45) display a similar shape, but the quantitative difference in the stress at the same shear rate can be considerable (even more than 40%), i.e. being significantly larger than the error estimates.

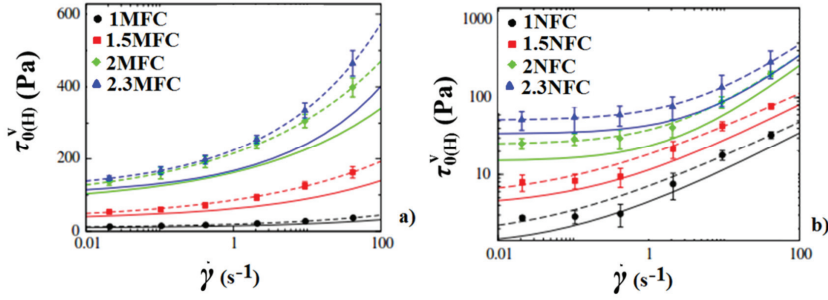


Figure 36 The points denote the shear rate stress values obtained from Eq.46 (protocol from device) and the dotted lines the Herschel-Bulkley fits to these. The solid lines denote the Herschel-Bulkley fits to the shear rates obtained with Eq.45 (corrected protocol) a) MFC suspensions and b) NFC¹ suspensions. (Publication VI).

The Herschel-Bulkley parameters obtained when fitting to the shear rate stress values obtained using the two different methods are compiled in Table 8. For this type of geometry, Herschel-Bulkley parameters is higher for NFC¹ suspensions to that of MFC suspensions for all consistencies, contrary from plate-plate geometry data where difference was observed for consistencies higher than 1 % Fig. 34c) and Fig. 35e).

In most cases, $\tau_{0(H)}^v$ has a higher value when the narrow gap approximation is used, i.e. obtained from the protocol obtained from device device, Eq. 46. Similarly, the flow index obtained using vane spindle (k_v) is smaller and the exponent in the Herschel-Bulkley function (λ_H), which is systematically larger for data without the correction for non-linearity, i.e. *protocol from device* (uncorrected flow curves). The conclusion is that, using the narrow gap approximation the non-linear effects of the complex fluid are suppressed compared to the real fluid behaviour (corrected flow curves). This emphasises the fact that this correction should be made whenever the material shows non-linear torque-angular velocity behaviour.

Table 8 Herschel-Bulkley parameters for the corrected and non-corrected flow curves of NFC¹ and MFC. Protocol 1 refers to the Herschel-Bulkley parameters ($\tau_{0(H)}^v, k_v, \lambda_H$) fitted against shear rate value from Eq. 45 and corrected protocol to one fitted against shear rate values obtained from device, Eq. 46 (Publication VI).

NFC					MFC				
Consistency (%)	protocol	τ_c (Pa)	k_v	λ_H	Consistency (%)	protocol	τ_c (Pa)	k_v	λ_H
1.0	Device	9.62	9.93	0.274	1.0	Device	1.55	5.58	0.461
	Corrected	8.64	6.26	0.285		Corrected	1.15	3.30	0.504
1.5	Device	30.1	55.9	0.232	1.5	Device	5.03	13.3	0.454
	Corrected	31.7	30.9	0.272		Corrected	3.83	7.67	0.501
2.0	Device	81.9	134	0.232	2.0	Device	24.7	13.4	0.694
	Corrected	73.9	88.8	0.239		Corrected	15.0	8.46	0.729
2.3	Device	111	114	0.305	2.3	Device	50.8	18.0	0.690
	Corrected	98.9	68.6	0.323		Corrected	33.9	9.83	0.753

4.2 Part II: Application of MNFC in papermaking suspensions

4.2.1 Viscometry, oscillatory and gravimetric dewatering of high consistency MFNC furnishes

The high consistency MNFC containing furnishes, presented in Table 3, consist of flocculated suspensions of MFC or NFC¹, cellulose fibres and fillers, with a complex network matrix formed due to attractive interaction forces between its components (Mörseburg and Chinga-Carrasco 2009, Saarinen *et al.* 2010, Subramanian *et al.* 2011). Data obtained from the amplitude sweep measurement on the plate-plate rheometer are presented in Figs. 37a)-b), and show that MFC based furnishes have higher G' than the ones based on NFC¹, the latter having higher WRV (and higher zeta potential) as presented earlier (Fig. 32). Furthermore, we see that G' is higher for furnishes containing pulp fibres, increasing with consistency for all furnishes (Horvath and Lindström 2007).

As seen in Fig. 37a), G' for NFC¹ containing furnishes are generally lower than those of MFC containing furnishes, as the less entangled and more mobile NFC¹ (greater adsorbed water layer) displays less flocculation within the furnish matrix (Horvath and Lindström 2007). The same is observed for their sole component suspensions, Fig. 32. Response of G' and G'' of 15 % consistency furnishes is shown as a function of the frequency in Fig. 37b). As seen from MFC and NFC² suspensions (Fig. 30) the G' is virtually independent of the frequency, while the G'' is constant at low frequency and increases slightly at higher frequencies, Fig. 37b), G' being an order of magnitude higher than G'' , indicating gel-like structure (Gisler *et al.* 1999, Persello *et al.* 1994).

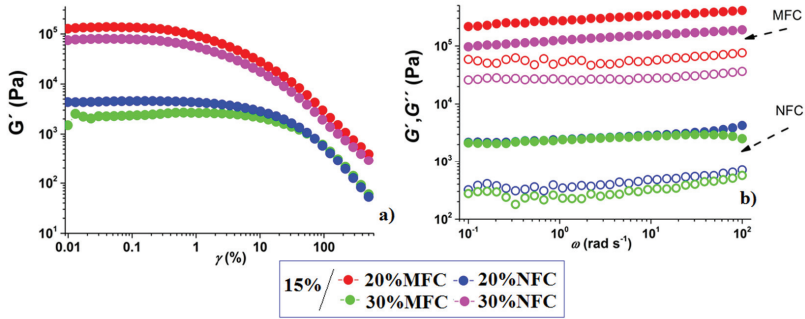


Figure 37 Oscillatory measurements for 15 % consistency MFC and NFC¹ containing furnishes: a) viscoelastic shear moduli (G' and G'') under amplitude sweep measurement, b) G' and G'' of MFC and NFC¹ containing furnishes as a function of angular frequency (ω). Open symbols G' and closed symbols G'' (Publication II).

Nanocellulose type, with its associated ζ , naturally influences the furnishes due to the various friction and mobility properties within the furnish-filler pigment matrix, which is seen as high G' taken from frequency sweep measurement at fixed angular frequency $\omega = 16 \text{ rad s}^{-1}$ for reference furnish without nanocellulose (30 % pulp, 70 % filler) and lower G' for MFC and NFC containing furnishes, Fig. 38a). The results of $\text{\AA}\text{\AA}$ -GWR static dewatering, presented in Fig. 38b), show that water retention for both reference furnish and MNFC containing furnishes decreases with consistency, being lowest for the reference furnish and highest for NFC¹ containing furnishes, having the similar trend as observed for sole component suspensions, Fig. 31c). The presence of pulp fibres in both MFC and NFC¹ containing furnishes decreases water retention, due to induced flocculation and phase separation between of long pulp fibres and gel-like MNFC.

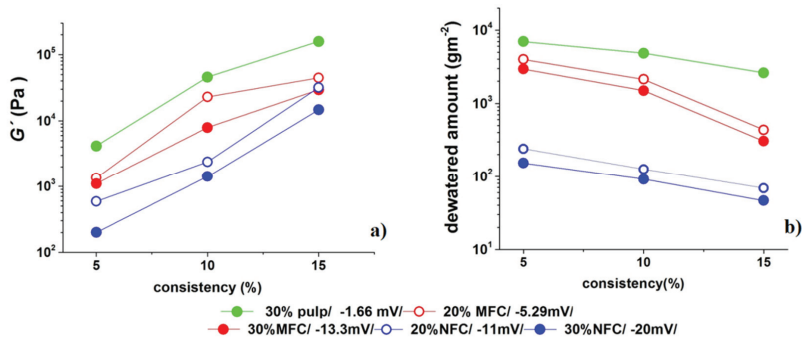


Figure 38 a) Elastic shear modulus (G') at $\omega=16 \text{ rad s}^{-1}$ obtained from frequency sweep measurements, as a function of consistency, with their zeta potential (ζ), for pulp furnish, MFC and NFC furnishes, and b) Dewatered amount in the $\text{\AA}\text{\AA}$ -GWR under static pressure conditions as a function of consistency; a) pulp fibres, MFC and NFC¹ suspensions, b) pulp furnish, and MFC and NFC¹ containing furnishes (Publication I).

4.2.2 Immobilisation measurements (IMC) for high consistency MFNC furnishes

Gap decrease curves from the IMC in DSO mode (Jäder and Järnström 2003, Wollny 2001) Figs. 39a) and c), show very similar behaviour for both the MFC suspensions and MFC containing furnishes. Likewise, the behaviour for NFC suspensions and furnishes is also similar, and presented in Figs. 39b)-d). In the case of MFC suspensions and MFC containing furnishes, initial dewatering is taking place immediately after the onset of vacuum, and the gap decreases rapidly, while for NFC¹ suspensions and furnishes the gap decrease development is very slow. There is no distinct rapid volume loss due to initial dewatering as was seen for MFC, but rather a gradual decrease in gap, which can be explained in terms of a loss of pore connectivity and effective partial sealing of the sample bottom layer due to ultrafines, including immobilised gel-content water. The gap decrease in the initial stage (after application of vacuum) is steeper for furnishes containing cellulose fibres, which is more obvious in case of NFC¹ furnishes supporting the gravimetric dewatering results from Fig. 38b), indicating that the presence of pulp fibres also influences positively the rate of dynamic dewatering through the flocculation mechanism, creating flow channels through the furnish cake/mat.

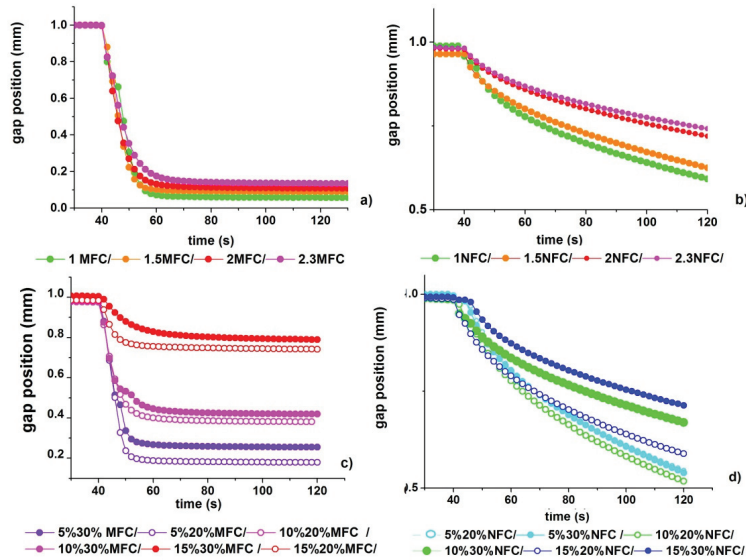


Figure 39 The gap decrease over time after onset of vacuum: a) MFC suspensions, b) NFC¹ suspensions, c) MFC furnishes, d) NFC¹ furnishes. Open symbols for furnishes with pulp cellulose fibres, closed symbols for furnishes without pulp fibres (Publication I).

Rheograms in Figs. 40a)-d) present the development of η^* and $\tan \delta$ due to the increase of solid content over the dewatering period (Publication I). After a rather quick initial increase, related to rapid dewatering, the η^* of MFC suspensions and furnishes reaches a plateau, the value of which depends in a complex way on the dewatering efficiency. The plateau value is highest for furnishes containing pulp fibres due to increased/improved dewatering Fig. 40 and Fig. 41.

The origins of the overshoots in η^* for MFC furnishes can possibly be related to wall-slip (phase separation typical of gels), or to an elastic stress overshoot, which is falsely interpreted by the rheometer as a viscous response (Ovarlez *et al.* 2009, Puisto *et al.* 2012). For NFC¹ furnishes, the increase in η^* follows the inverse of the behaviour indicated by the gap position reduction values (Fig. 39b)), i.e. increasing very slowly, the plateau hardly being reached even after the 800 s measuring period Figs. 41b)-d).

Rheograms depicted in Figs. 40a)-d) show a continuous increase of $\tan \delta$ and η^* for both MNFC suspensions and furnishes, with different scales in the time axis for MFC and NFC¹ suspensions and furnishes in Figs. 40a)-c) and Figs. 40b)-d). The overall conclusion drawn from Fig. 40 is that η^* and $\tan \delta$ of NFC¹ suspensions and furnishes have a maximum which develops much later than in the case of MFC suspensions and furnishes, due to the highly swollen (adsorbed water layer) NFC¹ making water removal difficult due to the sealed (gel-like) bottom layer of the filter cake.

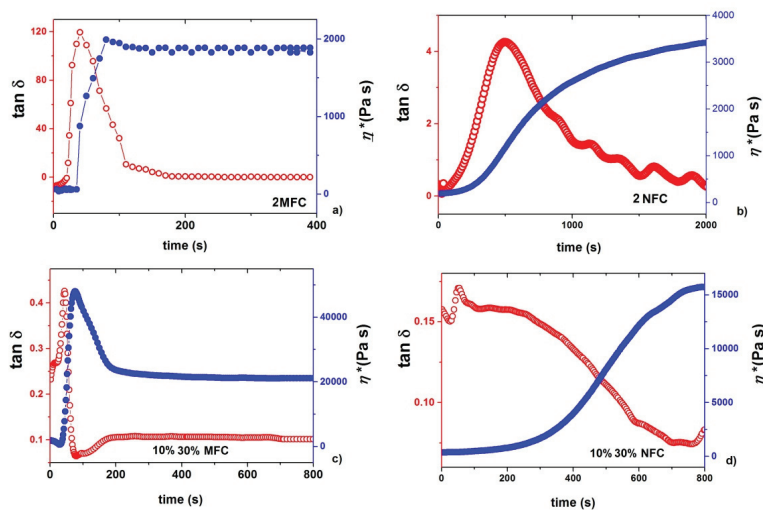


Figure 40 Rheograms of complex viscosity (η^*) and loss factor ($\tan \delta$) for MFC and NFC¹ suspensions and furnishes: a) 2 % MFC suspension, b) 2 % NFC suspension, c) 10 % MFC furnish without pulp fibres, d) 10 % NFC furnish without pulp fibres (Publication J).

As mentioned earlier NFC and MFC contain a significant amount of water inside and around the fibrillar particles (MFC), and also trap an even greater amount of water within the inter-fibrillar gel network (NFC¹).

As observed in Figs. 41b) and d) for NFC based suspensions and furnishes it is not possible to determine t_i as the fixed point at which the $\tan \delta$ reaches a plateau, as the NFC introduces a separate and independent effect on the t_i value. Instead of defining t_i using $\tan \delta$, which indicates a change in viscoelastic properties of the sample, it is necessary to use the rate of change $d(\tan \delta)/dt$ to define the t_{ip} and t_s , as presented in Figs. 41a)-d). This procedure allows determination of the turning points of $\tan \delta$ accurately, even for the NFC¹ suspensions and furnishes during dewatering.

The first zero of $d(\tan \delta)/dt$ is defined as the first immobilisation point t_{ip} , which marks the beginning of a rapid increase in the sample elasticity following the initial η^* rise. The second zero of $d(\tan \delta)/dt$ marks the complete immobilisation for the MFC suspensions and furnishes, and is defined as t_i , Figs. 41a)-d). Similar curves of $d(\tan \delta)/dt$ are observed between MFC suspensions and furnishes, Figs. 42a)-c), and between NFC¹ suspensions and furnishes, Fig. 42 b)-d), and their comparison shows the nature of increase of elasticity depending on the type of nanocellulose.

The interval between the t_{ip} and t_i is defined as the *immobilisation interval* (Publication I). Figs. 41e)-f) show that immobilisation interval is much longer for the gel-like NFC¹ for both suspensions and furnishes, where for NFC¹ furnishes without pulp fibres there is a slight time dependence on consistency, supporting both the WRV values and gravimetric dewatering results.

Therefore, immobilisation of water is present both as an inter-particulate and intra-particulate medium. In NFC¹, most of the water is in the form of an inter-particulate, gel matrix medium, whereas in MFC it is both an intra and inter-particulate medium.

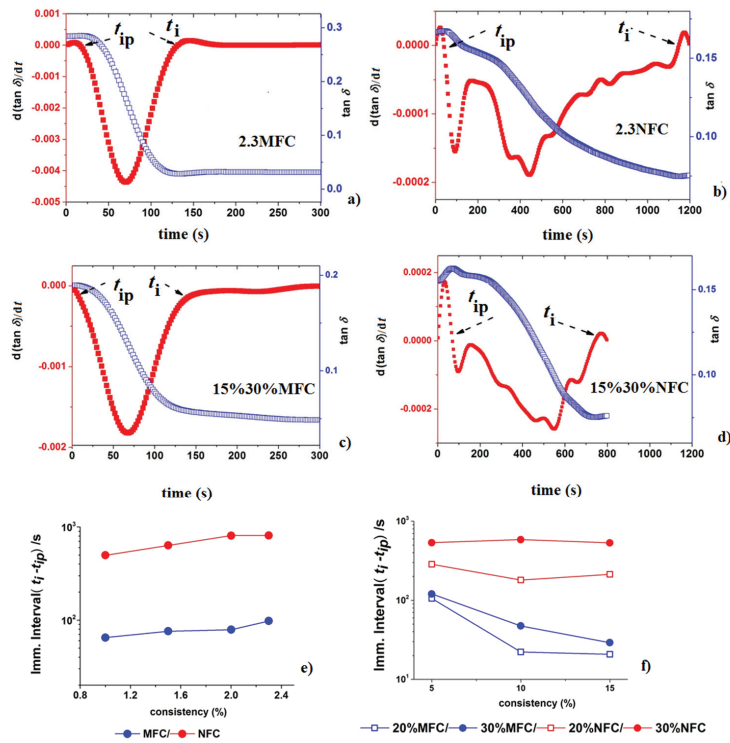


Figure 41 Determination of immobilisation interval, $\tan \delta$ and the $d(\tan \delta)/dt$; a) 2.3 MFC suspension, b) 2.3 NFC suspension, c) 15 % MFC furnish without pulp fibres, d) 15 % NFC¹ furnish without pulp fibres (open symbols $\tan \delta$, closed symbols $d(\tan \delta)/dt$); immobilisation interval calculated as $t_i - t_{ip}$, e) MFC and NFC¹ suspensions, and f) MFC and NFC¹ containing furnishes (Publication I).

4.2.3 Behaviour under shear rates conditions and implementation in shear-induced dewatering of high consistency MNFC containing furnishes

The steady state flow curves of MFC/NFC¹ furnishes over three decades of shear rate ($\dot{\gamma} = 0.1 - 1\ 000\ \text{s}^{-1}$) are presented in Fig. 42a). All four types of furnish are shear thinning, indicating the rupture of the flocculated network as the shear rate increases, and typical for nanocellulose behaviour (Iotti *et al.* 2011, Lasseguette *et al.* 2008, Saarinen *et al.* 2010, Richmond *et al.* 2010). All furnishes show power law behaviour where $n \approx -1$, when fitted in Eq. 25, with actual fitted exponents $-1.02 \leq n \leq -0.94$ in agreement with some examples of earlier work (Lasseguette *et al.* 2008, Puisto *et al.* 2012, Richmond 2012).

The static yield stress (τ_0^s) of all furnishes increases with consistency, Fig. 42b), and for higher consistencies is greater for furnishes without pulp fibres. Here we see that the τ_0^s of MFC furnishes is higher than that of NFC¹ furnishes, contrary to results for suspensions, which could be related to the difference in yield point determinations, wall slip effect and shear banding profile at higher consistencies. When considering dynamic dewatering conditions, it is important to recognise how the structure of the sample evolves as the solid content increases. For a set value of $n = -1$ for all furnishes, fitted data according to the power law are presented with the corresponding flow coefficients (k) in Fig. 42c).

Greater flocculation tendency for fibrillar material MFC containing furnishes is seen as higher k , when compared with the more swollen, water adsorbing gel-like NFC¹ furnishes, displaying their earlier onset of mobility within the overall matrix.

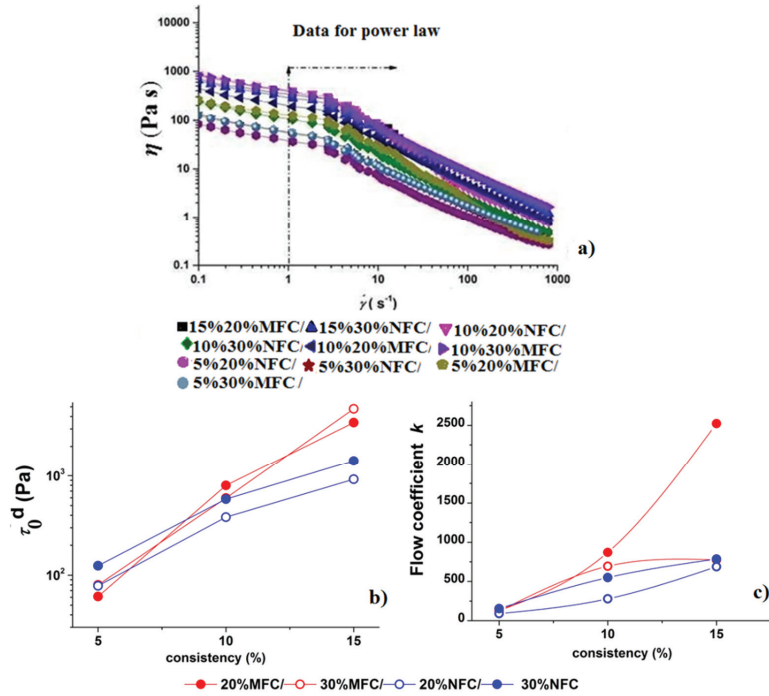
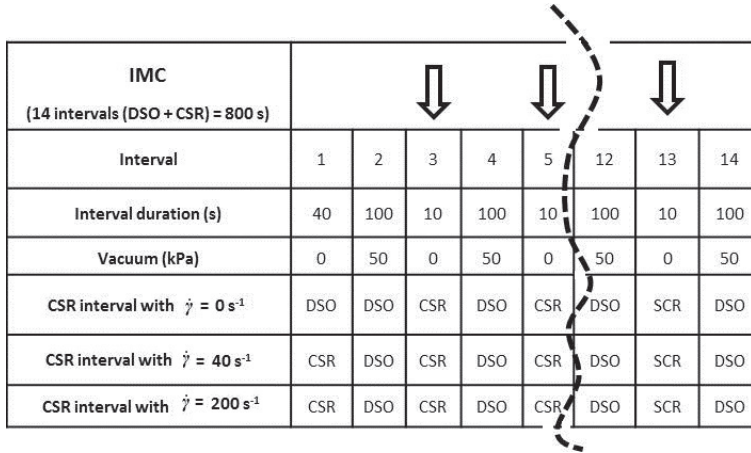


Figure 42 Shear controlled test mode for MFC and NFC¹ containing furnishes at $\dot{\gamma} = 0.1 - 1000 s^{-1}$, a) dynamic viscosity (η) flow curves for furnishes displaying a strong shear-thinning response to high shear, therefore data taken for power-law calculation is mapped on the diagram b) apparent static yield point (τ_0^d) obtained from amplitude sweep measurement as the tangent crossing point, and c) flow coefficient k calculated for the fit of the power law index set to $n = -1$ (Publication II).

The dewatering model, with application of shear only between oscillation and vacuum cycles, combines both testing approaches for IMC, DSO and CSR modes. Dewatering with vacuum was performed during the DSO intervals, due to the fact that applying vacuum during the CSR cycle would force the finest particles in the bottom layer to stick to and in the filter pores, preventing water removal from upper layers. The samples were pre-sheared in the cycle for 40 s, in the first interval, and then the periodic succession of DSO and CSR proceeded, as schematically presented in Table 9. Three different measurement schemes were performed, with different shear rates that were applied in the CSR intervals; shear rates being 0/ 40/ 200 s^{-1} .

Table 9 Dewatering with IMC utilising shear as a combination of DSO cycles with applied vacuum and CSR cycles with three shear rates $\dot{\gamma} = 0/40/200 \text{ s}^{-1}$. The shear rate 40 s^{-1} was chosen as the smallest which produced an observed difference in the dewatering results, and 200 s^{-1} as the highest which gave reproducible results due to the Weissenberg effect (Publication I).



IMC (14 intervals (DSO + CSR) = 800 s)									
Interval	1	2	3	4	5	12	13	14	
Interval duration (s)	40	100	10	100	10	100	10	100	
Vacuum (kPa)	0	50	0	50	0	50	0	50	
CSR interval with $\dot{\gamma} = 0 \text{ s}^{-1}$	DSO	DSO	CSR	DSO	CSR	DSO	SCR	DSO	
CSR interval with $\dot{\gamma} = 40 \text{ s}^{-1}$	CSR	DSO	CSR	DSO	CSR	DSO	SCR	DSO	
CSR interval with $\dot{\gamma} = 200 \text{ s}^{-1}$	CSR	DSO	CSR	DSO	CSR	DSO	SCR	DSO	

Figs. 43a)-c) show the response of MNFC furnishes to IMC dewatering with combined DSO and CSR as a function of gap decrease, and development of apparent viscosities (η^* and η) during the succession of DSO and CSR cycles. The gap behaviour during dewatering plotted in Fig. 43a) shows a significant gap increase at the instant of the beginning of rotation of the CSR intervals, due to the breakdown response of the highly viscoelastic structure to shear, i.e. the change during the Weissenberg effect (Yamamoto 1958, Mezger 2006). Reasons for the difference in the final gap position, i.e. a lower final gap position for the NFC¹ containing furnishes can be related to an uneven solid content gradient in both the radial and z -direction of the sample (Willenbacher *et al.* 1999), or to the different flocculation tendency upon shearing for MFC, both giving rise to a different viscoelastic response of the dewatered sample. Fig. 43b) presents the increase of η^* (DSO), and it clear to see that, apart from the first (pre-shearing) DSO interval, each following DSO interval is dependent on the viscoelastic response of the furnish rheology during the previous CSR intervals. Of note is the non-linear dependency of η^* on the increase in solids content, shear thinning during the DSO interval and in response to the shearing history in previous CSR intervals, which is accompanying the Weissenberg effect. In Fig. 43c) are plotted the η responses in the DSO intervals from the NFC¹ containing furnishes during the time period from 470-800 s in the measurement, i.e. over the last three intervals. An increase in η at the beginning of rotation, due to the Weissenberg effect, is followed by a profound shear thinning during all three intervals, for all imposed consistencies. The behaviour of η shows that even after many previous “initial dewatering” intervals (DSO), the shear thinning mechanism is still very much present up to the end of the complete measurement, providing further creation of dewatering channels. Therefore, the solids content of the furnish cake, in the case of

MNFC containing furnishes, cannot be calculated from the IMC measurement directly as a function of a gap decrease.

To resolve this, the final solid content, for each given furnish, and hence the dewatering model applied, was calculated gravimetrically as the average of ten measurements from ten separate dewatered pads (Publication II).

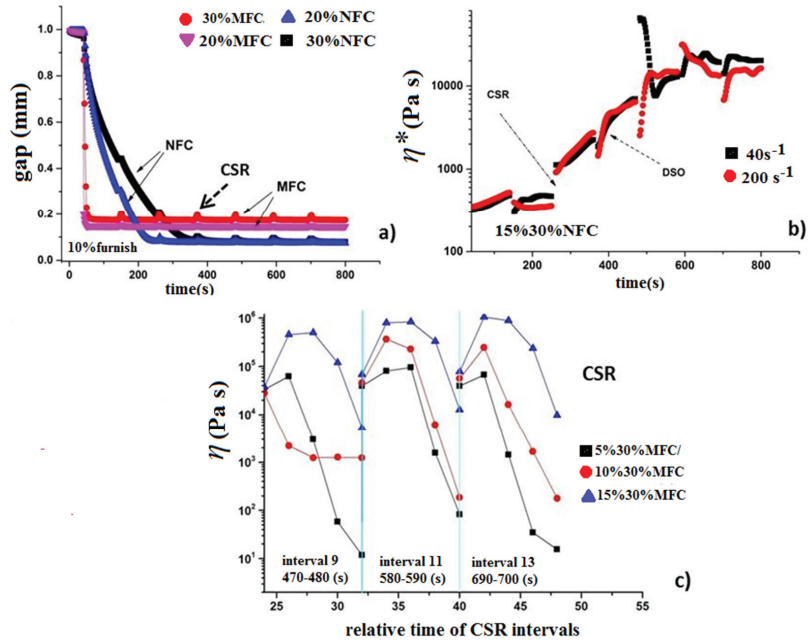


Figure 43 Dewatering with shear and vacuum application cycles: a) gap decrease for MFC and NFC containing furnishes at 15 % consistency, b) η^* in the DSO dewatering intervals for 15 % NFC¹ containing furnish (data plotted are from DSO intervals, while the broken discontinuity points - empty places without data - are CSR intervals), c) dynamic viscosity η during last three CSR intervals for NFC¹ containing furnishes with shear rate 200 s^{-1} (DSO intervals are not plotted but marked with a vertical line); time is expressed as relative time of duration of the last intervals (9, 11, and 13) of the measurement (Publication I).

Fig. 44 shows the final solids content increase of the dewatered samples as a function of shear rate (dewatering scheme), and the k values as presented in Fig. 42. As this figure depicts, applying a higher shear rate results in a solids content increase regardless of the MFC/NFC¹ type, i.e. displaying no difference in their dewatering nature or whether cellulose fibres are present or not (Publication I). This again indicates the gel-like response of the nanofibrillar material, which under high shear becomes broken down and phase separated.

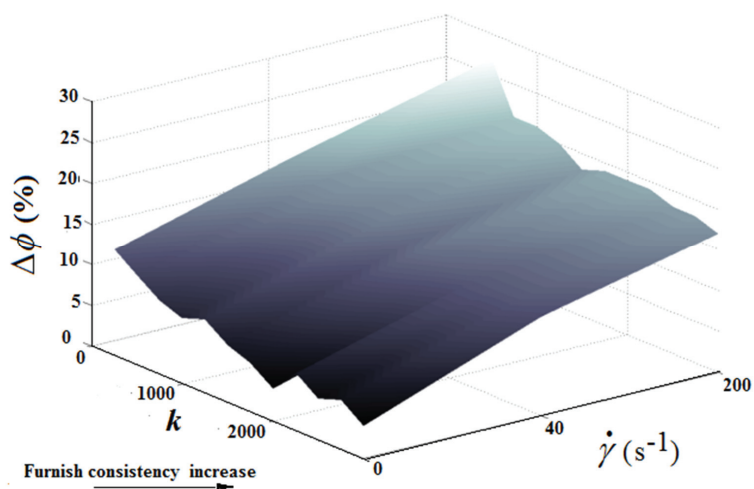


Figure 44 Final solids content increase of the dewatered samples as a function of shear rate (dewatering scheme) and the respective k value (Publication I).

4.2.5 Use of MFC/NFC in coating colours as a co-binder (Publications III, IV and V)

4.2.5.1 Viscometry, oscillatory and gravimetric dewatering response for partial substitution with MNFC

Comparison of the apparent viscosity using the low shear Brookfield viscometer, for the coating colours shown previously in Table 4, at rotation rates of 50 and 100 min^{-1} , is presented in Table 10. We see that, across the formulated coating colours, for each given pigment blend, CMC as co-binder always gives a higher viscosity value than MFC/NFC¹ as co-binder. The higher mobility of the particulates in the MFC/NFC¹ coating colour matrix is reflected in a lower apparent viscosity value (Astarita and Marrucci 1974, Wu *et al.* 2000). From ÅA-GWR results, CMC as co-binder results in greater static water retention in the coating colour compared with that of MFC/NFC¹ as co-binder. Contrary to the MFC/NFC suspensions, as seen previously from Table 7, coating colours with NFC¹ as co-binder have higher apparent viscosity than those with MFC, which is considered to be related to the independent structural behaviour of MFC/NFC¹ and pigment.

Table 10 Results of low-shear apparent viscosity (Brookfield) and gravimetric dewatering (AA-GWR) for MFC/NFC¹ and coating colours. Complementary to the GCC portion is the kaolin (clay) in all clay containing formulations in order to form 100 pph pigment (Publication III).

Coating colours	eGCC/ ref	eGCC/ MFC	eGCC/ NFC	fGCC/ ref	fGCC/ MFC	fGCC/ NFC	75 eGCC/ ref	75 eGCC/ MFC	75 eGCC/ NFC	50 GCC/ ref	50 eGCC/ MFC	50 eGCC/ NFC	100 fclay/ ref	100 fclay/ MFC	100 fclay/ NFC
AA-GWR (gm ²)	198	235	213	189	233	208	153	190	195	99	194	206	129	152	194
η_v @ 50 min ⁻¹ (mPa s)	844	534	793	1 809	1 459	1 548	896	525	652	782	480	581	725	330	423
η_v @ 100 min ⁻¹ (mPa s)	512	328	496	1 094	894	981	553	339	422	476	307	374	431	225	275

Oscillatory measurements were used to characterise the microstructure of the coating colours, Figs. 45a)-c), illustrating the dependence of G' and G'' moduli on the strain at a constant angular frequency of $\omega = 1 \text{ rad s}^{-1}$. For all coatings, the presented G' is much larger than G'' , with G' values being larger for the CMC alone containing coatings than those having MNFC as co-binder. The linear domain is extended further in respect to shear stress for kaolin coatings than for carbonate coatings, due to stronger supra molecular structure build-up by CMC and kaolin, Figs. 45b)-c) (Husband *et al.* 1993, Husband 1998, Triantafillopoulos 1985, Triantafillopoulos 1996). Transition between the linear and non-linear regimes occurs at larger deformations when MNFC is included in the co-binder system, indicating a different thickening mechanism (Publication I).

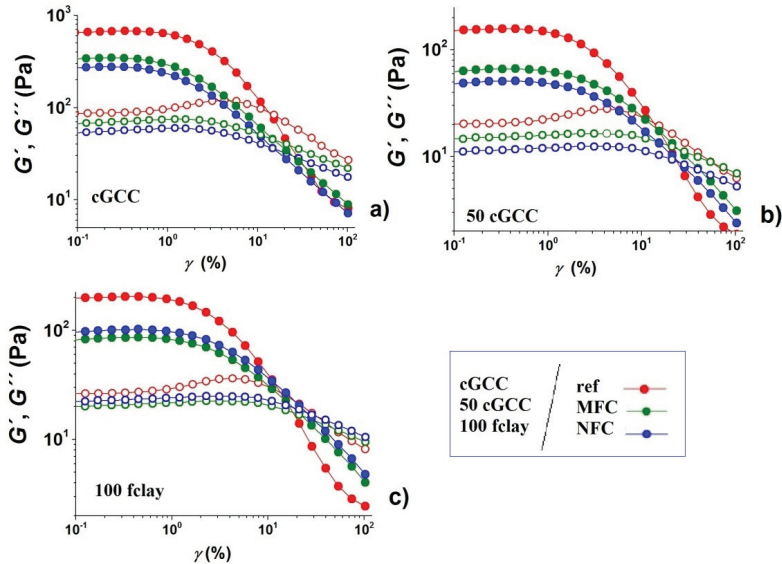


Figure 45 Storage modulus (G') and viscous modulus (G'') against strain (γ) for the various coating colour thickener systems containing a) fGCC, b) 50:50 eGCC:clay, and c) 100 clay. Complement to the GCC portion is kaolin (clay) in all blend formulations in order to form 100 pph pigment. Elastic modulus (G') closed symbols, loss modulus (G'') open symbols (Publication III).

In Figs. 46a-e), the G' and G'' moduli in the linear regime are presented as functions of the frequency. Again we notice that G' is considerably larger than the G'' , and G' increases slowly with frequency whilst its magnitude remains considerably larger than that of G'' (Coussot 2005, Whittle and Dickinson 1997). The G'' increases at higher frequencies and also slightly at lower frequencies, with decreased values in between.

For coating colours that have kaolin pigments, G' and G'' both increase with the increase in proportion of kaolin in the pigment coating formulation blend (Bossard *et al.* 2007). For carbonate pigment-only coatings, G' and G'' increase with higher pigment packing density, Figs. 46 a)-b), similarly as seen for the apparent viscosity in Table 10. However, all coatings show a decrease in G' when CMC is partially replaced with MNFC.

Rreplacement of CMC does not regenerate the floc structure interactions, and MNFC essentially behave more or less independently in the mix environment. This may be due to their mutual charge repulsion and/or the higher inter-particle mobility of MNFC, seen in Publication I and II (Lindström and Carlsson 1982, Wu *et al.* 2000) which results in lower elasticity than in the case of the higher CMC level in the presence of pigments/latex (Husband *et al.* 1993, Husband 1998, McGenity *et al.* 1992, Sosa *et al.* 2006). Essentially, pigment and latex pass independently through or around the nanocellulose gel-formed regions (Ridgway and Gane 2007).

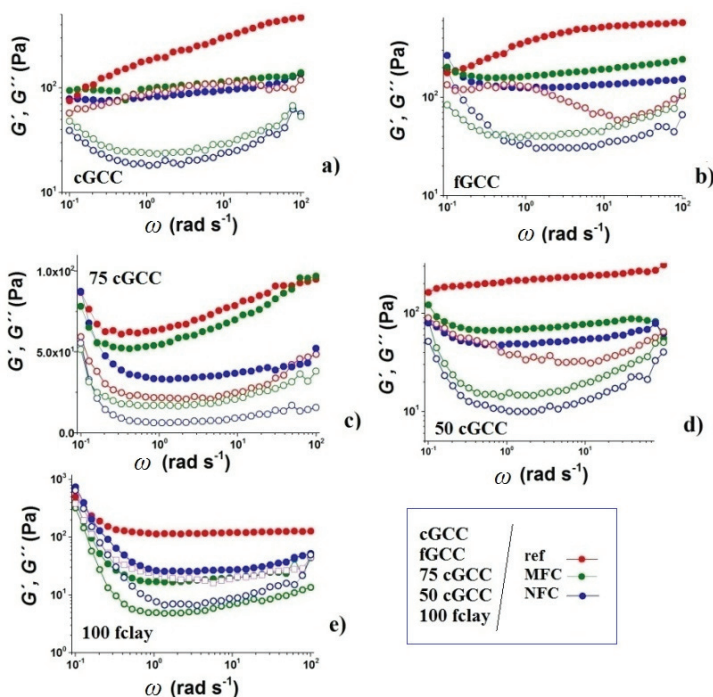


Figure 46 Response of G' and G'' against angular frequency ($\omega = 0.1-100 \text{ rad s}^{-1}$) for all coating colours: a) 100 cGCC, b) 100 fGCC, c) 75 cGCC d) 50 cGCC and e) 100 clay. Complement to the GCC portion is kaolin (clay) in all formulations in order to form 100 pph pigment. Elastic modulus (G') closed symbols, loss modulus (G'') open symbols (Publication III).

4.2.5.2 Steady shear flow curves for coating colours - partial substitution of CMC with MNFC

Steady shear flow curves of coating colours are presented in Figs. 47a)-c). All coatings show a similar pattern of decrease in η as the shear rate increases from very low to very high ($\dot{\gamma} = 0.001 - 1\,000\text{ s}^{-1}$), i.e. shear thinning behaviour. Unlike in the case of η^* , where the elucidation of elastic and viscous components is combined under oscillation, the dynamic flow curves show three distinct regions (Fadat *et al.* 1988, Moan *et al.* 2003), covering three shear rate zones: i) $\dot{\gamma} = 0.001 - 100\text{ s}^{-1}$, over which viscosity decreases drastically and data do not follow a single power law behaviour, ii) at shear rates $\dot{\gamma} = 100 - 500\text{ s}^{-1}$, in which all flow curves follow a close fit to a perfect power law behaviour, as presented in Fig. 47 a), and iii) at high shear rates $\dot{\gamma} = 500 - 1\,000\text{ s}^{-1}$. It is important to point out that in the zone with highest shear rate NFC¹ coatings have a further strong drop in viscosity at very high shear rates, Figs. 47b)-c), due to either a complete collapse of the gel-like structure within the coating colour matrix, or much more likely a boundary slip condition due to the expulsion of water from the gel. This latter effect, if confirmable, is potentially a vital observation in respect to blade coater runnability and the establishment of plug flow under a high speed running blade (Gane 1997).

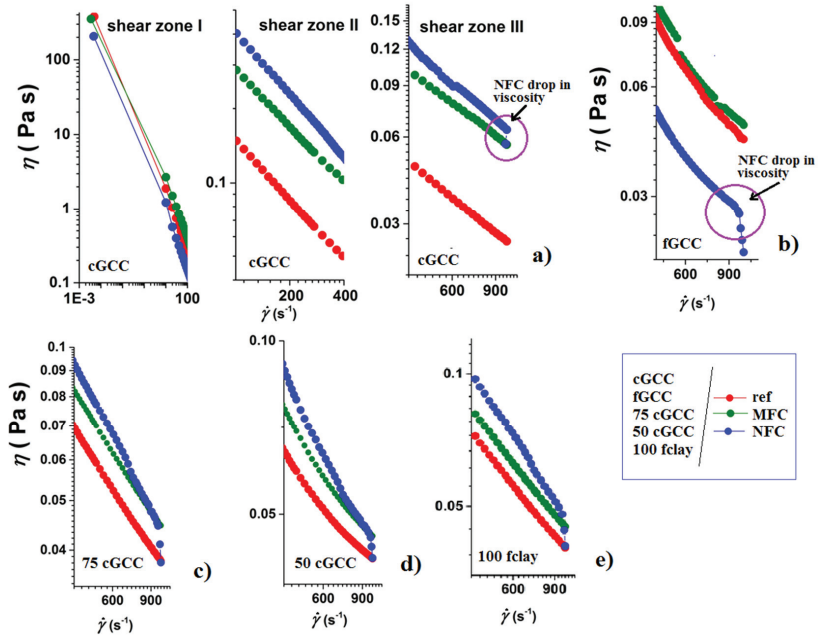


Figure 47 Dynamic viscosity (η) log-log flow-rheograms as a function of shear rate ($\dot{\gamma} = 0.001 - 1\,000\text{ s}^{-1}$) with the three different shear rate zones: a) flow rheograms with three distinct shear zones for cGCC coatings, b) third shear zone for fgGCC coatings, c) third shear zone for 75 cGCC coatings, d) third shear zone for 50 cGCC coatings, and e) third shear zone for 100 fclay coatings. Complement to the GCC portion is kaolin (clay) in all blend formulations in order to form 100 pph pigment (Publication III).

4.2.5.3 Cox-Merz rule – does MNFC behave as a polymer during partial substitution of CMC?

Following the Cox-Merz rule provides an indication of polymer-like behaviour (Deka and Dey 2012), it does not hold for MNFC containing coating colours, with the η^* being much higher than the η , and this follows observed behaviour for MNFC suspensions reported by other authors, Figs. 48a)-e).

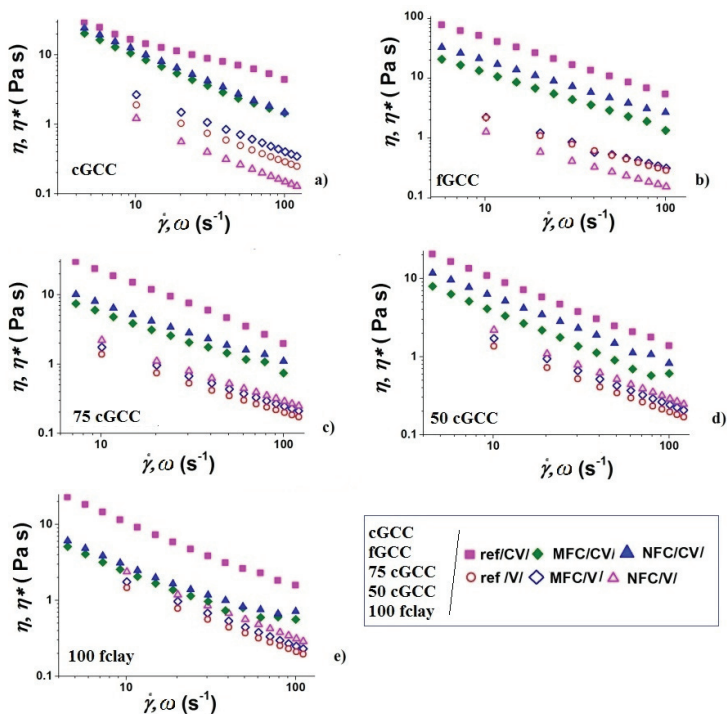


Figure 48 Complex viscosity (η^*) response as a function of increasing angular frequency ($\omega = 0.1 - 100 \text{ rad s}^{-1}$) and dynamic viscosity (η) as a function of shear rate (within the same range $\dot{\gamma} = 1 - 110 \text{ s}^{-1}$) (Cox-Merz test condition) for reference and MFC/NFC¹ containing coatings: a) cGCC, b) fGCC, c) 75 cGCC, d) 50 cGCC, and e) 100 clay: complex viscosity (η^*) (shown also as sample label postscript “CV”) and steady state viscosity (η) (shown also as sample label postscript “V”). Complement to the GCC portion is kaolin (clay) in all blend formulations in order to form 100 pph pigment (Publication III).

Iterative least squares methods are used to calculate an average value of the shear thinning coefficient (n) for each of the flow curves at a given viscosity (η and η^*), and then the behaviour of the k value is observed according to the power law. From data presented in Table 11 we see in most cases that k is larger for NFC¹ containing than for MFC containing coatings, indicating the strong gelation properties of the NFC¹.

Table 11 Shear thinning behaviour for all coating colours: initial and final values of flow curves for complex viscosity response (η^*) and dynamic viscosity (η) with their respective fitted flow indexes (k) and shear thinning coefficients (n) (Publication III).

	eGCC/ CMC	eGCC/ MFC	eGCC/ NFC	fGCC/ CMC	fGCC/ MFC	fGCC/ NFC	75 eGCC/ ref	75 eGCC/ MFC	75 eGCC/ NFC	50 GCC/ ref	50 eGCC/ MFC	50 eGCC/ NFC	100 clay/ ref	100 clay/ MFC	100 clay/ NFC
η^* (Pas) at $\omega = 0.1 \text{ rad s}^{-1}$	1157	978	1060	2870	1790	2180	1380	949	1270	1181	1040	1048	2490	5000	6810
η^* (Pas) at $\omega = 100 \text{ rad s}^{-1}$	1.47	1.45	1.49	2.90	1.35	2.70	1.96	0.74	1.09	1.38	0.60	0.82	1.58	0.56	0.71
η (Pas) at $= 0.01 \text{ s}^{-1}$	378	252	206	252	245	214	157	344	254	154	335	252	166	344	274
η (Pas) at $= 100 \text{ s}^{-1}$	0.280	0.290	0.150	0.287	0.317	0.150	0.198	0.247	0.280	0.190	0.241	0.287	0.210	0.250	0.310
η (Pas) at $= 1000 \text{ s}^{-1}$	0.050	0.040	0.020	0.040	0.050	0.20	0.040	0.450	0.030	0.030	0.440	0.040	0.040	0.050	0.040
k_{η^*} ($n_{\eta^*} = 0.83$)	181.2	63.4	69.3	262.2	68.9	120.8	103.4	36.1	49.1	63.7	23.8	37.8	69.0	20.6	24.8
n_{η^*} ($k_{\eta^*} = 79.61$)	0.630	0.880	0.863	0.630	0.880	0.860	0.770	1.015	0.940	0.880	1.110	1.000	0.862	1.134	1.090
k_{η} ($n_{\eta} = 0.82$)	13.3	17.5	7.0	12.8	13.4	7.2	9.3	11.2	12.9	9.0	12.8	11.8	9.9	11.0	11.2
n_{η} ($k_{\eta} = 11.45$)	0.790	0.740	0.930	0.800	0.780	0.913	0.865	0.817	0.802	0.860	0.820	0.800	0.850	0.780	0.820

4.2.5.4 Structure recovery measurements for partial substitution of CMC with MNFC in coating colours

Results from the 3ITT recovery experiment are presented in Figs. 49a)-b). The 3ITT (CSR-CSR-CSR) test reveals the viscosity recovery as an increase of η in the third interval of the test (Willenbacher *et al.* 1997). The data are normalised by its final value (η/η_f) at the end of the third interval, η_f , as presented in Fig. 49a). Coating colours that have CMC as co-binder have a typical overshoot behaviour after high shear, which is more pronounced for kaolin based coating colours (Bossard *et al.* 2007, Sosa *et al.* 2006). While the CMC coatings in the third interval show the expected overshooting character of η after high shear, the behaviour for MNFC containing coatings is very different, without any overshooting character (Li *et al.* 2001, Yziquel *et al.* 1999). The results from the 3ITT elasticity recovery test are presented in the Fig. 49b), showing normalised elasticity (G' normalised by its final value G'_f) higher for CMC coatings. The overall conclusion from the 3ITT tests is that the traditional nature of interactivity induced by CMC with pigments/latex is very different to that of independence between MNFC and pigments/latex.

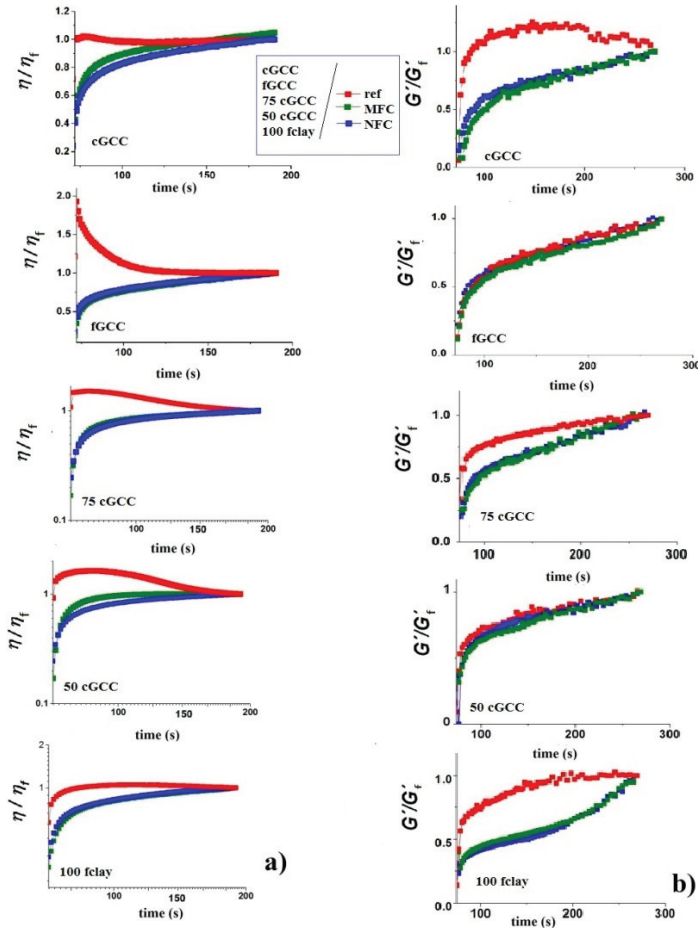


Figure 49 3ITT tests: a) normalised (η/η_t) in the third interval of the 3ITT experiment for all coatings, b) normalised elastic modulus (G'/G'_t) after the third interval for all coating colours. Complement to the GCC portion is kaolin (clay) in all blend formulations in order to form 100 pph pigment (Publication III).

4.2.5.5 Immobilisation measurements (IMC) for partial substitution of CMC with MNFC in coating colours

The immobilisation curves for the various coating colours are presented in Figs. 50a)-e) in the form of the increase in G' and change in $\tan \delta$ during dynamic dewatering in DSO mode (Wallström and Järnström 2004, Wollny 2001). Partial substitution of CMC with MNFC decreases water retention, as immobilisation times decrease for all coatings regardless of the pigment blend, which is seen as a consistent pattern in all immobilisation curves, Figs. 50a)-e), supporting gravimetric dewatering data. Both cGCC and fGCC coatings having MNFC as co-binder have shorter immobilisation time t_i than clay based MNFC containing coatings, as seen from $\tan \delta$.

Immobilisation is presented as an increase in elasticity, and t_i determined as the plateau of G' , Figs. 50a), c) and e). From immobilisation time scale it is obvious that calcium carbonate based coatings have less water retention than clay containing coatings, with coarse carbonate grade (cGCC) having the least water retention, seen in gravimetric dewatering results (Gane and Hooper 1989, Sand *et al.* 2009, Sandås *et al.* 1989) Table 10. The major effect with such high aspect ratio clay, as used here, is emphasised in the CMC-clay interaction (Li *et al.* 2001). The finer carbonate grade (fGCC) has medium water retention in the series, related to the increased particle number, Fig. 50d). The immobilisation curves of all MFC containing coatings have a much steeper increase in G' and $\tan \delta$, than NFC¹ containing, indicating much faster initial dewatering and lower water retention over time, as seen in Fig. 40 previously for the respective MNF/NFC¹ suspensions.

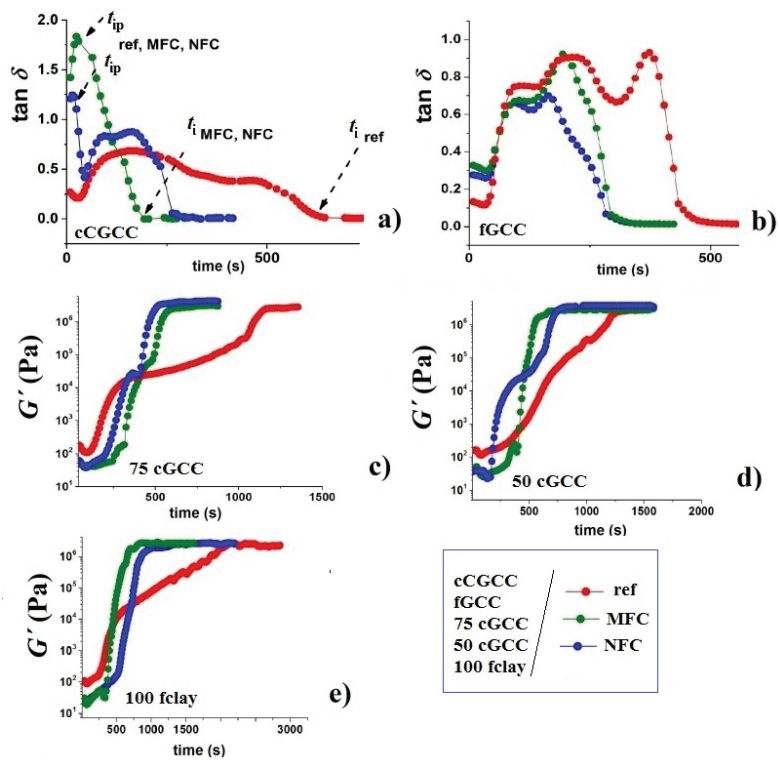


Figure 50 Elastic modulus (G') and damping factor ($\tan \delta$) immobilisation rheograms: a) change in $\tan \delta$ during immobilisation interval (t_i - t_{ip}) for cGCC coatings, b) change in $\tan \delta$ during immobilisation seen as (t_i - t_{ip}) for fGCC coatings, c) increase of G' during immobilisation for 75 cGCC coatings, d) increase of G' during immobilisation for 50 cGCC coatings, and e) increase of G' during immobilisation for 100 fclay coatings. Complement to the GCC portion is kaolin (clay) in all blend formulations in order to form 100 pph pigment (Publication III).

To illustrate the link between structure recovery and dewatering, the structure regeneration of coating colours, as presented previously in Fig. 49, was defined as the time needed for recovery to 90 % of the viscosity/ elasticity in the 3ITT tests. The correlation, therefore, between filtrate amount and elasticity starting value, Figs. 49 and 50, and hereby shows similar behaviour for all CMC containing coatings, as shown in Figs. 51a)-b). Higher structure elasticity, indicating likely flocculation, results in higher water retention under gravimetric dewatering for CMC coatings, as observed in longer immobilisation intervals and faster elasticity recovery time. In fact, the immobilisation time behaviour is seen to be following strongly an inverse correlation to the recovery of G' , Fig. 51b). As presented in Fig. 52c), when CMC is partially substituted with MNFC, the correlation given in Eq. 63 does not follow a linear trend except for the reference coatings, but rather a curvilinear form encompassing the MNFC containing samples. This is related to the viscoelastic gel-like nature of the MNFC, which affects the IMC measurements as if it were an independent additive (Puisto *et al.* 2012, Sand *et al.* 2009, Walls *et al.* 2003).

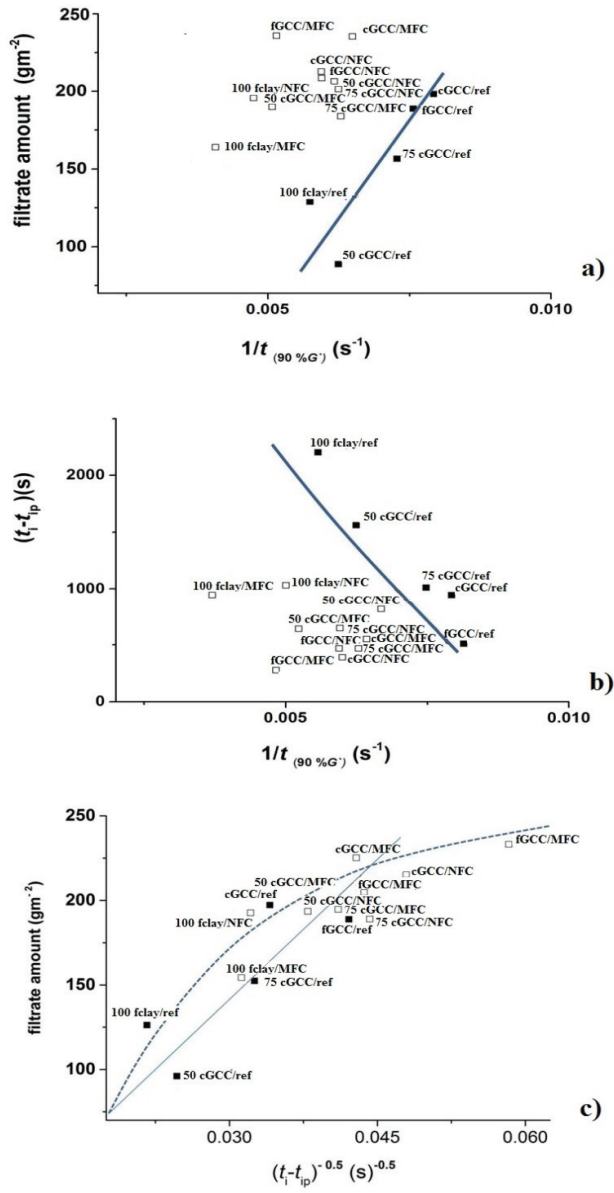


Figure 51 Influence of coating colour elasticity recovery on dewatering: a) correlation amongst certain formulations between filtrated amount with AA-GWR against recovery value defined as time needed for recovery of 90 % of starting elasticity (G') in the third interval of 3ITT tests, b) correlation amongst certain formulations between immobilisation interval against recovery value of time needed for recovery of 90 % elasticity (G') viscosity in the third interval of 3ITT tests, and c) correlation diagram showing filtrated amount in the AA-GWR measurement and immobilisation interval ($t_i - t_{ip}$) for reference and MFC/NFC¹ coatings (Publication III).

4.2.6 MFC/NFC compared as partial and total substitute for CMC in coating colours

4.2.6.1 Viscometry, oscillatory and gravimetric dewatering measurements

For the evaluation of how total substitution of CMC with MNFC would affect coating colour rheology and dewatering behaviour, the formulations shown in Table 5 are used, with NFC² as the nanocellulosic constituent, as presented in Table 3. The relative amount of each ingredient in the coating colour formulations is shown in Table 12.

Comparison of the apparent viscosity values, shows that CMC as co-binder always gives a higher viscosity value than MFC/NFC² as co-binder, which can be associated with the induced flocculation mechanism between CMC and pigments/latex, as concluded from Table 10. Pronounced shear thinning behaviour is seen as a change in apparent viscosity discernible for all coating colours. Absence of the flocculating elastic effect of CMC on the pigment/latex content reduces the yield stress of coatings (τ_c^s and τ_c^d), determined as in Fig. 33. Gel-like NFC² as sole co-binder generates a coating with higher structure strength, as seen previously in Fig. 34.

Table 12 The properties of coating colours where MFC/NFC² is used as total substitution of CMC (Publication IV).

Coating colour	Ref/ no CMC	Ref	MFC /no CMC	MFC/CMC	NFC /noCMC	NFC/CMC
ζ (mV)	- 18.0	- 18.2	-18.4	- 18.3	- 18.0	- 18.4
τ_0^s (Pa)	4	33	25	30	33	62
τ_0^d (Pa)	6	27	23	27	37	68
Consistency (%)	62	62	62	62	62	62
AA-GWR (gm ⁻²)	220.2	156.2	267.3	215.0	233.1	207.3
η_v @ 10 min ⁻¹ (mPa.s)	3 478	4 400	3 270	2 980	2 960	2 870
η_v @ 10 min ⁻¹ (mPa.s)	5 64	1 806	1 345	1 112	1 121	985
η_v @ 100 min ⁻¹ (mPa.s)	257	907	886	870	775	750

Figs. 52A-B show the G' and G'' at the constant angular frequency $\omega = 1$ (rads⁻¹), for all coating colours. Both G' and G'' exhibit a constant initial value at small strains, G_0' and G_0'' , respectively, with $G_0' > G_0''$, until a critical strain amplitude γ_c is reached, Fig. 52Aa). Reduced normalised storage modulus (G'/G_0') and elastically normalised loss modulus (G''/G_0') are presented in Fig. 52Ab). By normalising or reducing G'' by G_0' (the underlying static elasticity) we observe an effective isolated description of the free flowing suspension phase viscosity, providing an understanding of the phase separation between the flocculated or gel-like material and the flowing components. In the cases where reduced loss moduli (G''/G_0') have lower values, the flocculated material is

separated from the liquid flow phase, and so we can conclude that in the absence of CMC fibrils are generally flocculated under the static condition.

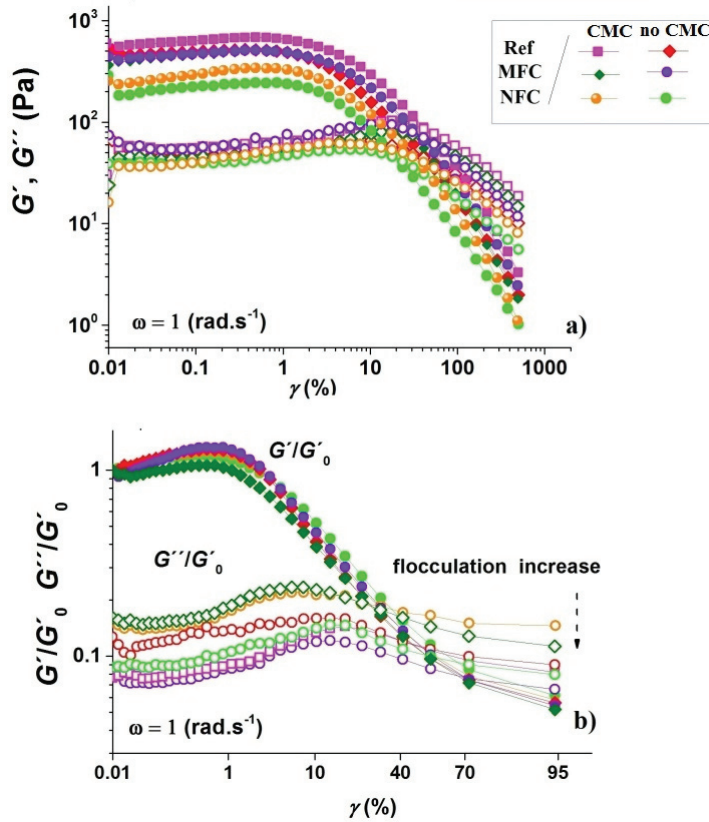


Figure 52A Storage G' and viscous modulus G'' as a function of strain γ , over a range of angular frequency $\omega = 1, 3$ and 10 rad s^{-1} , respectively: a) G' and G'' at $\omega = 1 \text{ rad s}^{-1}$, b) reduced G'/G_0' and elastic reduced G''/G_0'' at $\omega = 1 \text{ rad s}^{-1}$. Elastic modulus (G') closed symbols, loss modulus (G'') open symbols (Publication IV).

Furthermore, oscillatory measurements have been carried out at various angular frequencies, $\omega = 1, 3$ and 10 rad s^{-1} , respectively, Fig. 52Ba-c), showing that G' and G'' intrinsic curve profiles are frequency independent. As shown in the same figure, above γ_c , G' decreases gradually, while G'' shows a strain hardening characterised by an overshoot in the curve, Figs. 52Ba-c). We see this effect more pronounced for coatings without CMC, as strain hardening is typical for agglomerate particulate systems incorporating the presence of fillers (Dickinson and Chen 1999, Husband *et al.* 1993, Husband 1998, McGenity *et al.* 1992, Ridgway and Gane 2007, Sosa *et al.* 2006, Page *et al.* 2002). Overshoots of G'' are also related to non-linear oscillatory response of gel-like materials due to shear bands and wall slip, resulting, in particular, in difficulties with data analysis from the plate-plate geometry (Dickinson and Chen 1999, Gisler *et al.* 1999).

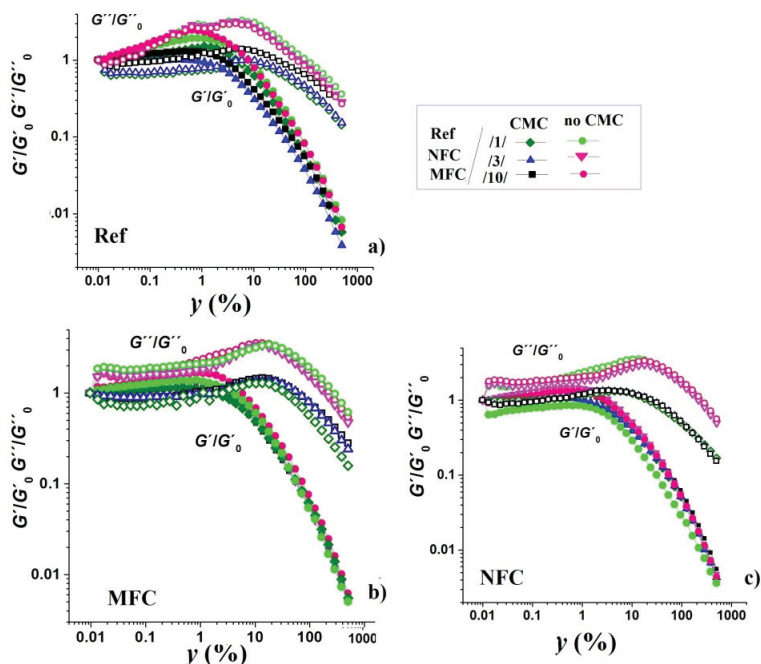


Figure 52B Storage G' and viscous modulus G'' as a function of strain γ , over a range of angular frequency $\omega = 1, 3$ and 10 rad s^{-1} , respectively: a) reduced G'/G'_0 and G''/G''_0 of Ref coatings, b) reduced G'/G'_0 and G''/G''_0 of MFC containing coatings, c) reduced G'/G'_0 and G''/G''_0 of NFC² coatings. Elastic modulus (G') closed symbols, loss modulus (G'') open symbols (Publication IV).

4.2.6.2 Structure recovery measurements comparing partial with total substitution of CMC by MNFC in coating colours

Viscosity recovery in the 3ITT test for each formulated colour at all three intervals is presented in Fig. 53a), and reduced dynamic viscosity (η/η_f) is shown in Fig. 53b), where η is reduced by its final value at the end of the third interval (η_f).

Here we see clearly much more rapid recovery of structure for the reference sample, where the elasticity inducing effect of CMC by flocculation of pigment/latex is strongest, as was seen in Fig. 49a). The dispersing effect of CMC on the fibrils, and conversely the absence of this effect when CMC is totally absent, can be seen through longer recovery after cessation of high shear. Recovery time, as defined by the time needed for the 90 % recovery of dynamic viscosity η to the value of the initial dynamic viscosity (η_0), is presented in Fig. 53c).

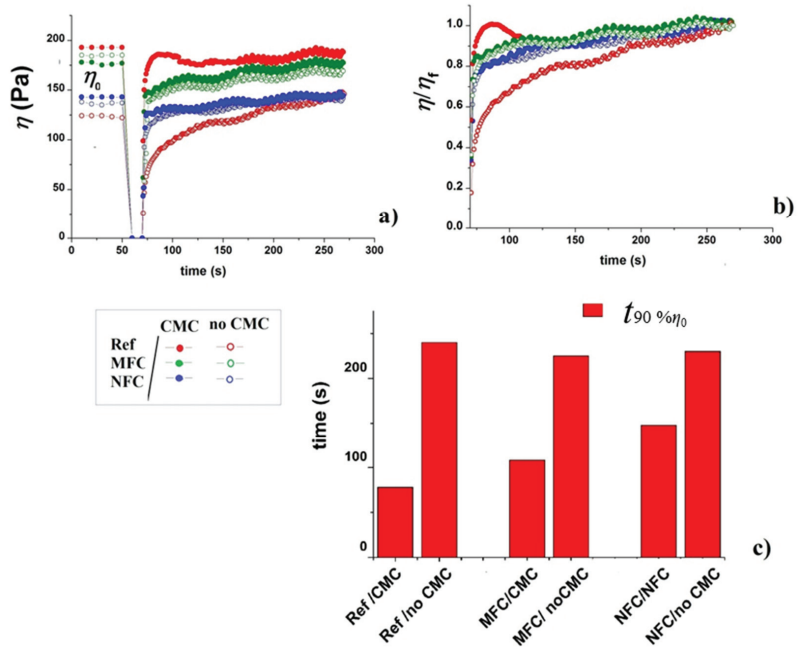


Figure 53 Viscosity recovery 3ITT (CSR-DSO-CSR) test: a) transient viscosity (η^+) against time for all coatings, b) reduced transient viscosity η^+/η_t , and c) time for 90 % recovery in transient viscosity (η^+) in the third interval low shear regime after high shear in the second interval to the initial dynamic viscosity (η_0) (Publication IV).

Transient shear viscosity of coating colours at low shear rate (0.01 and 0.1 s^{-1}) was observed using both smooth and roughened plate surface geometry, Figs. 54a)-c). The effect of strain hardening for MFC/NFC containing coatings at very low shear rate ($\dot{\gamma} = 0.01 \text{ s}^{-1}$) is observed within the LVE region for η^* as an increase during long measuring time, Fig. 54a), and as a function of τ . The strain hardening effect is stronger for smooth geometry, as distorting boundary alignment by having a rough surface reduces the strain hardening, Figs. 54b)-c) (Fenistein and van Hecke 2003, Seth *et al.* 2008, Van Hecke 2005, Weber *et al.* 2012). For higher shear rate ($\dot{\gamma} = 0.1 \text{ s}^{-1}$) the continuous strain hardening effect for smooth geometry is modified by a stress oscillation effect around the plateau value, connected with instrumental feedback due to gel-like wall slip, following the schematic in Fig. 54d) (Klein *et al.* 2007, Yeow *et al.* 2005). Thus, to develop the understanding of the internal structural properties of the gel-dominated component of the rheological behaviour, it is important to observe in addition the recovery in elasticity exposed by the related overshoot occurring up to the strain hardening zone, Figs. 54e)-f), which is equivalent up to the duration of $t = 1\,000 \text{ s}$, as seen in Figs. 54a)-c). The reduced transient viscosity ($\eta^+/\eta_{t=1\,000 \text{ s}}$), and its overshoot in the elastic recovery is a typical feature of the flocculating action of CMC with pigment/latex (Bossard *et al.* 2007, Li *et al.* 2001, Yziquel *et al.* 1999).

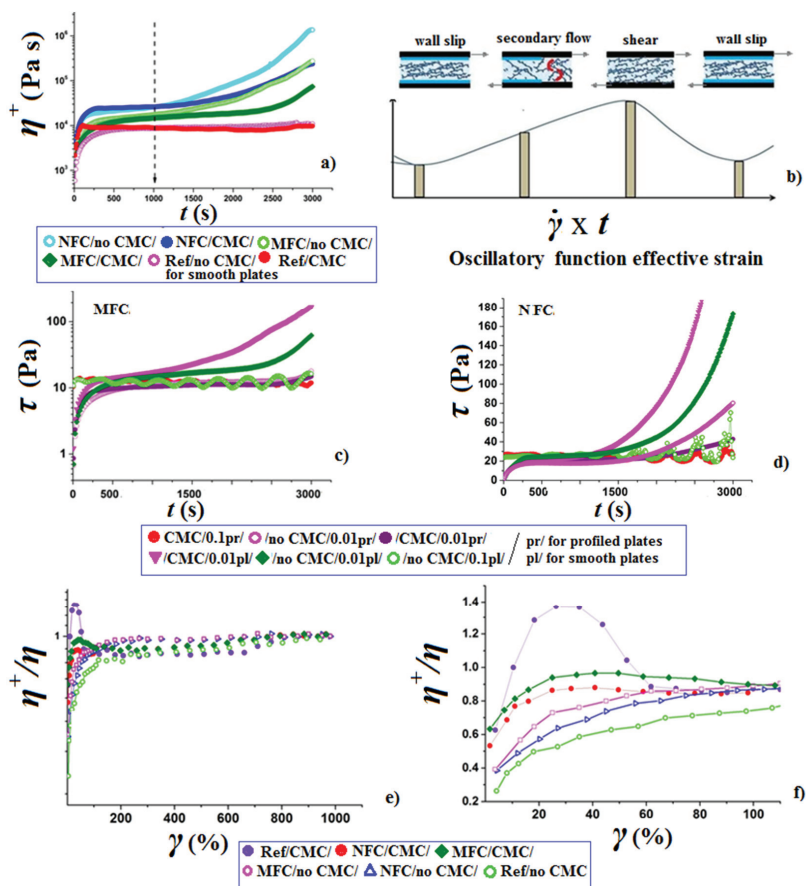


Figure 54 Small shear rate stress response toward equilibrium: a) strain hardening seen as increase of complex viscosity in LVE, b) MFC containing coating colours, c) NFC² containing coating colours, d) schematic drawing of phase separation and instrumental feedback events, e) reduced transient viscosity ($\eta^+/\eta_{t=1000}$), equivalent to the whole measurement duration, and f) first 100 s overshoots for CMC containing coatings (Publication IV)

4.2.6.3 Immobilisation measurements (IMC) comparing partial with total substitution of CMC with MNFC in coating colours (Publication IV)

Clear difference in the immobilisation time is seen between total and partial substitution of CMC by fibrillar gel-like MNFC material. Figs. 55a-c) show the change in G' , and $\tan \delta$ is shown in Fig. 55d). All immobilisation curves plotted in comparison to each other, Figs. 55c)-d), show that: (i) reference coatings with and without CMC show the contrast between water retention induced by the flocculating effect of the highly charged polymer chain acting on pigments/latex, and (ii) providing the comparison with MFC/NFC coatings, for which, in absence of CMC, the nanocellulose prevents water from leaving the sample by its gel forming properties. Highly flocculated MFC, in the form of agglomerates, induces phase separation in coatings in the absence of CMC, and thus has the lowest water retention.

In contrast, the highly gel-like NFC component, when in coatings with CMC, retains water strongly, as do the flocculated pigments/latex, but this decreases somewhat if CMC is withdrawn, supporting results from gravimetric dewatering, Table 12.

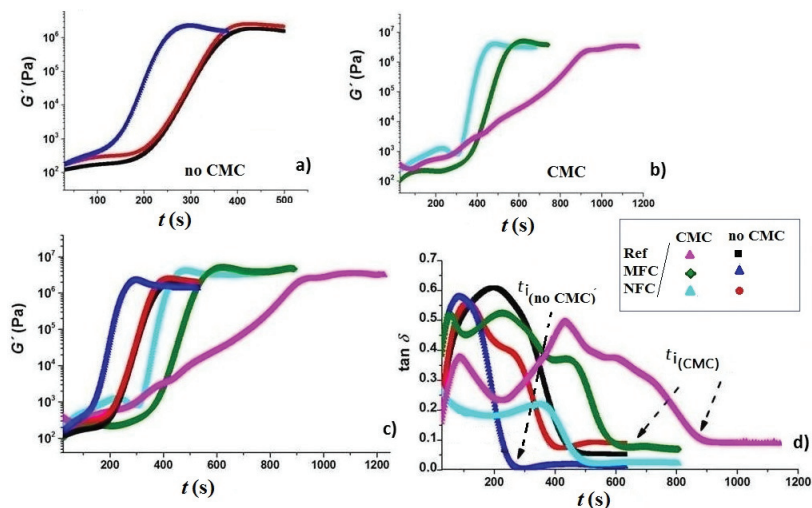


Figure 55 Increase of storage moduli: a) immobilisation observed in the form of elasticity increase (G') for coatings without CMC, b) immobilisation observed as elasticity increase (G') for coatings with CMC, c) immobilisation observed as change in loss factor ($\tan \delta$) for all coatings (Publication IV).

Figs. 56a-c) present groupings of like-behaving materials, illustrating how the immobilisation mechanism differs between the flocculating action of CMC on pigment/latex and that of the absence of its flocculating effect on gel-forming fibrillar materials. The MNFC colours group together, when considering gravimetric dewatering and recovery of structure, presented in Table 11 and Fig. 53. To be clearly observed is the action of CMC in dispersing the nanofibrillar component, which results in increasing water retention and prolonging immobilisation, Figs. 56b-c). However, this prolongation is clearly not as lengthy as the case for pigment/latex and CMC alone.

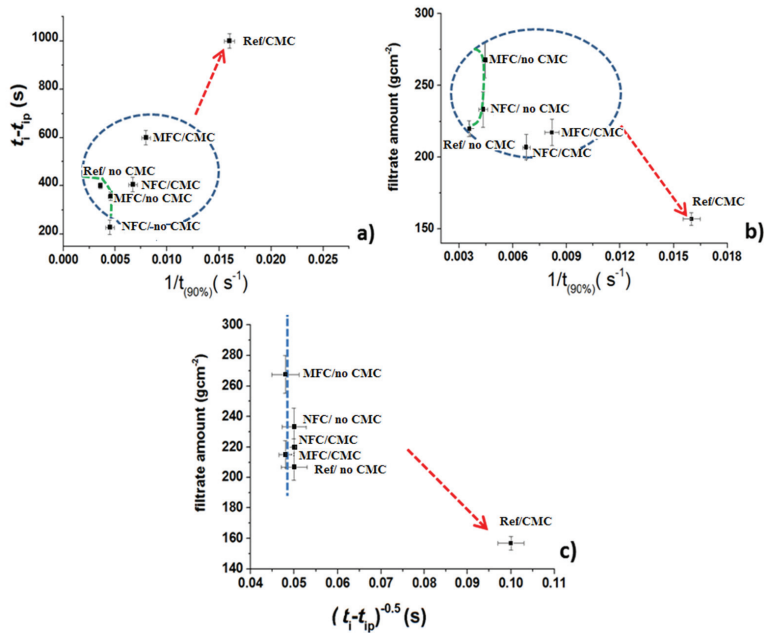


Figure 56 Grouping of like-behaving materials: a) correlation amongst coatings between filtrate amount with $\dot{A}A$ -GWR against structure recovery value defined as time needed for recovery to 90 % of starting viscosity in the third interval of the 3ITT tests, b) correlation amongst coatings between immobilisation interval ($t_i - t_{ip}$) against recovery value, c) plot of filtrate amount in the $\dot{A}A$ -GWR measurement and immobilisation interval ($t_i - t_{ip}$) for reference and MFC/NFC² coatings, showing little to no correlation (Publication IV).

From rheological analysis of structure recovery and immobilisation, Fig. 56, it is obvious that absence of CMC leads to an agglomeration tendency of the nanofibrillar component, reducing its ability to retain water in the matrix, but in contrast the pigment/latex becomes more stable when CMC is removed, as presented schematically in Fig. 57.

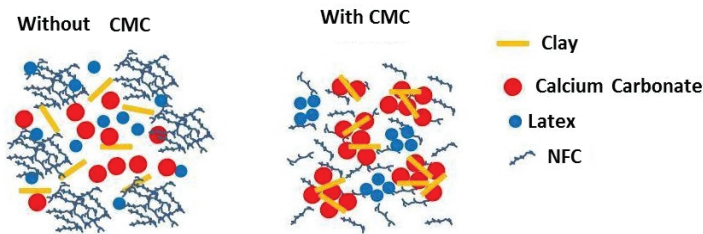


Figure 57 Schematic representation of the balance between the action of CMC in dispersing NFC and in flocculating pigment and latex (Publication IV).

4.3 Coating structure of MNFC containing coatings

Analysis of the dried tablets structure using microscopy, mercury intrusion porosimetry, and the contrasting liquid interaction reveal the changes in consolidation mechanism when MNFC additives are present in coating colour formulations and its resulting impact on pore connectivity (Publication III).

4.3.1 SEM images of MNFC containing coatings

Scanning electron microscopy (SEM) images, Fig. 58, were taken of a clean broken surface of the tablets, made from coating colours presented in Table 4. Images (10) are shown in Figs. 58a)-c) for cGCC, fGCC and clay, respectively.

The cGCC/MFC sample in Figs. 58a) and b) appears to be more dispersed than the reference sample, suppressing the typical flocculating mechanism of the CMC by being trapped on the cellulose fibrils. The NFC¹, however, does not perform in the same way as the MFC, and contributes to more flocculation. The SEM pictures for the clay containing colours, Fig. 58c) show the general high aspect ratio of the clay particles, as well as the relative disorientation properties of the platelets in the presence of the complementary 75 parts cGCC.

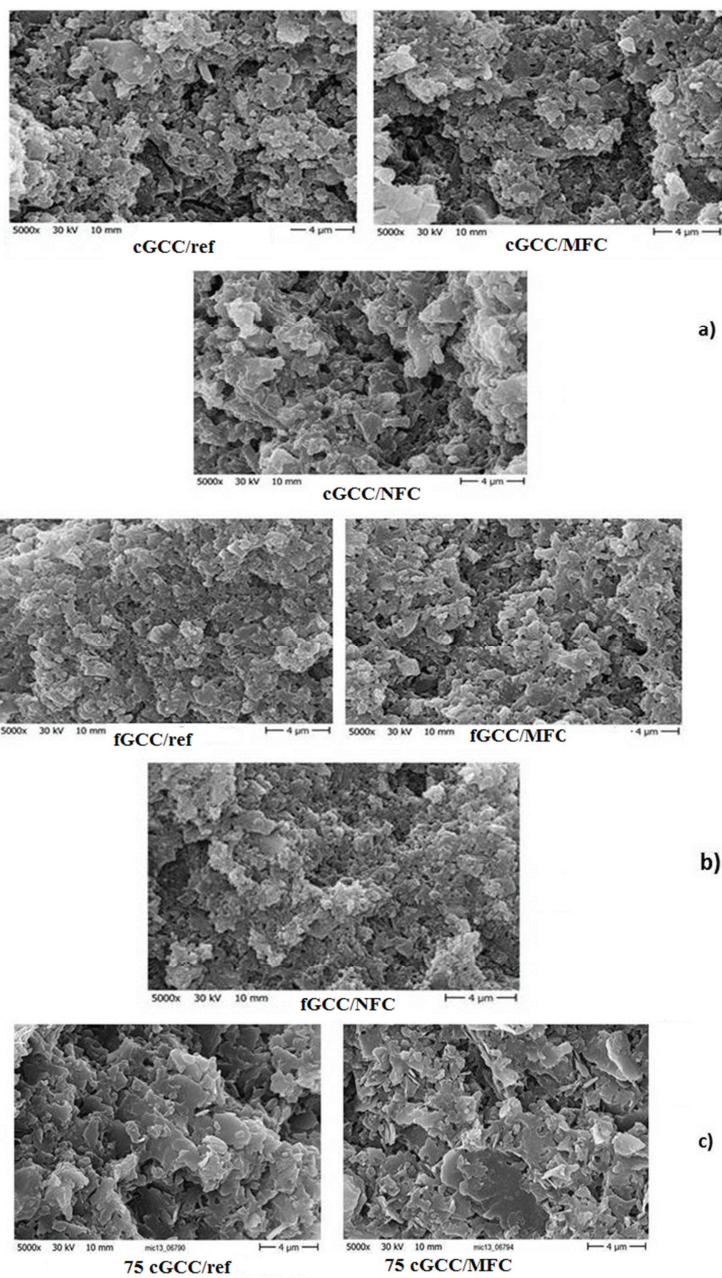


Figure 58 SEM images of the various cgcc and fgcc containing coating structure tablets: a) cGCC/ref (CMC as sole co-binder), cGCC/ MFC and cGCC/NFC¹ (partial CMC substitution), b) fGCC/ref, fGCC/MFC and fGCC/NFC¹, and c) 75cGCC/ref; 75cGCC/MFC (Publication V).

4.3.2 Mercury intrusion porosimetry : MNFC containing coatings

Cumulative mercury intrusion curves of all samples are presented in Fig. 59, and by taking their first derivative the pore size distributions based on equivalent Laplace diameter show that the samples have monomodal pore size distributions, Figs. 59b)-d) (Gane *et al.* 1996, Gane *et al.* 2004). Reduction of CMC and addition of NFC¹, Fig. 59b), makes the coating structure of the cgcc coatings more porous with larger pores, i.e. it is suspected to be immobilised sooner at lower solids content. This suggests that the coating colour matrix is either more flocculated or has immobilised at lower solids content due to the gel nature of the NFC¹ (Publication II) – confirmed by the rheological and immobilisation analysis, Publication III. Reduction of CMC and addition of MFC in the fgcc sample, Fig. 59c) only slightly reduces the pore volume but hardly changes the pore size distribution - as it is already fine without the addition of the MFC and so cannot pack more tightly. For coating colours containing some 25 parts of kaolin clay, Fig. 59d), the reduction of CMC and replacement by MFC has led to a somewhat larger pore size. This could be related to the potential disruptive packing by fibres on the orientation of clay platelets (Gane *et al.* 1997).

The overall conclusion to be drawn from Figs. 59b)-d) is that reduction of CMC and addition of gel-like NFC¹ makes the coating structure become more porous with larger pores, i.e. it is either more flocculated or immobilised sooner at lower solids content in relation to the gelation properties of the NFC¹.

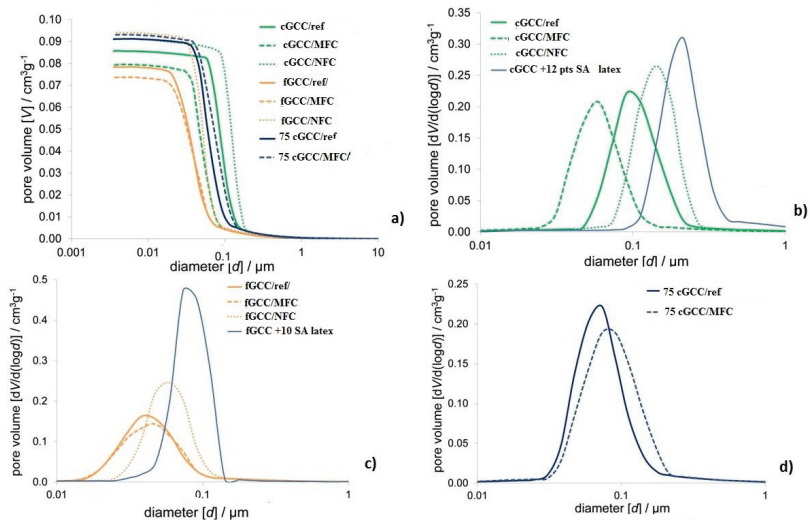


Figure 59 Mercury intrusion measurements: a) mercury intrusion curves for all the tablet samples, the data have been corrected using Pore-Comp for mercury and penetrometer effects and also for sample compression, b) pore size distribution of the cGCC tablet samples including an extra control structure containing latex only for comparison, c) pore size distribution of the fgcc tablet samples, including also an extra control structure containing latex only, and d) pore size distribution of the carbonate-clay tablet samples (Publication V).

The total specific intruded volumes of mercury into the samples over the diameter range 0.004 – 414 μm and the porosity and bulk modulus values are summarised in Table 13, showing the increase in pore volume on the addition of NFC¹ and the decrease in pore volume on the addition of MFC compared to the Reference samples for the cgcc samples. The increased pore volume in the case of NFC¹ addition can be related back to the stronger gel formation and thus the higher pore volume left after removal of the interstitial gel-bound water. This, however, is also in combination with the reduction of the CMC from 0.4 parts to 0.1 parts, as presented in Table 4. Reduction of CMC and addition of MFC/NFC¹, do not change bulk modulus, i.e. the skeletal material is dominated by the pigment and remains hard.

Table 13 Total intruded volume of mercury into the tablet samples (Publication V).

Sample	Total specific intruded volume (cm ³ g ⁻¹)	Porosity (%)	Bulk modulus (MPa)
cGCC/ref	0.086	16.29	21 100
cGCC/MFC	0.079	15.13	21 600
cGCC/NFC	0.091	17.38	21 900
fGCC/ref	0.078	15.10	19 600
fGCC/MFC	0.074	14.14	18 900
fGCC/NFC	0.094	17.76	21 600
75 cGCC/ref	0.091	17.07	20 900
75 cGCC/MFC	0.093	17.24	20 400

4.3.3 Hexadecane Absorption: non-polar liquid interaction with MNFC containing coatings

The tablet blocks were firstly 100 % saturated after the hexadecane absorption time of 48 hours (Ridgway *et al.* 2006, Ridgway *et al.* 2011, Schoelkopf *et al.* 2000). The absorption of non-polar liquid, therefore, is slow in these modified formulations compared with typical coatings. Absorption rates curves (Ridgway *et al.* 2006, Schoelkopf *et al.* 2002) Figs. 60a)-c), show the longest absorption rates for those samples containing MNFC, which diverge slightly from the overall linear behaviour between 100 and 350 s^{0.5}, compared to that of the reference CMC as sole co-binder samples. Figs. 60a) and b) show that from the stable linear regions (data up to 100 s^{0.5}) it is possible to deduce the discretely separable short and long time absorption rates (Ridgway *et al.* 2006). Inclusion of MFC has reduced the short time absorption rate and increased the long time scale absorption, while the inclusion of NFC¹ reduced both short and long time absorption rates, Fig. 60c).

Since the long timescale absorption rate is related to the balance between the wetting force and the permeability of the saturated structure, this increase in long timescale absorption rate for MFC containing samples indicates the presence of larger pores or more highly connected pores (Gane *et al.* 2004).

Porosimetry showed that the addition of MFC introduced larger pores in the case of the clay containing sample but no increase in pore size for the 100 % cGCC samples as addition of MFC to cGCC has led to a higher pore connectivity to inert liquid flow, indicating that residual fibre content in the MFC is responsible for the increased pore connectivity effect.

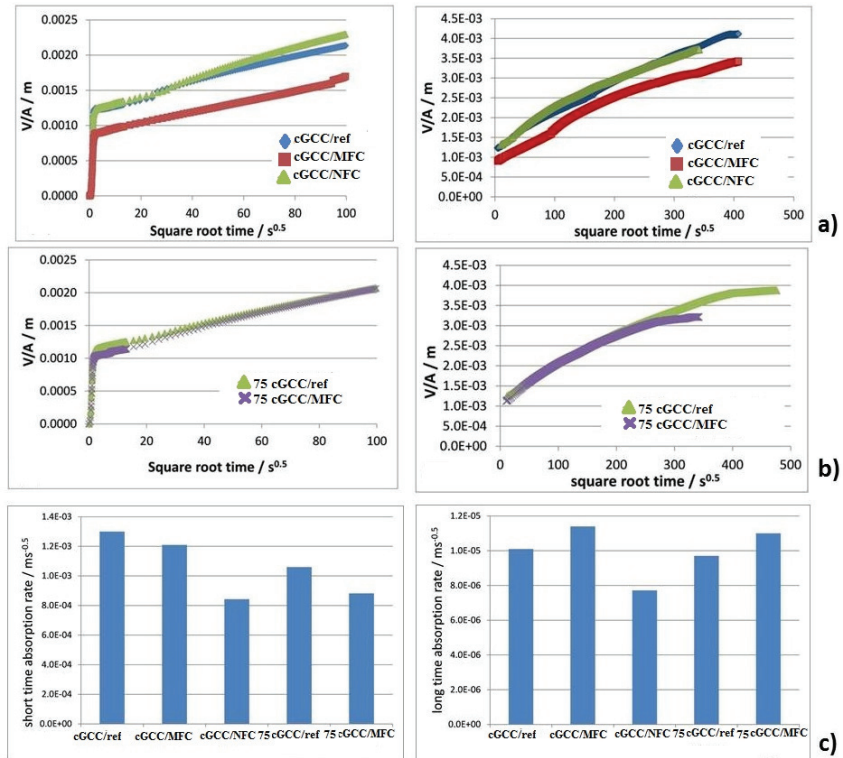


Figure 60 Hexadecane absorption: a) absorption curves for the 100 % cGCC samples, short and long time absorption, b) absorption curves for 75cGCC-clay samples short and long time absorption, c) short timescale absorption rates up to $2 \text{ s}^{0.5}$, and long timescale absorption rates over times greater than $5 \text{ s}^{0.5}$ and less than $100 \text{ s}^{0.5}$ (Publication V).

4.3.4 Water Absorption: rewetting interaction with MNFC containing coatings

The water absorption curves, following correction for evaporation, are shown in Figs. 61a) and b) for the cGCC and 75cGCC samples, respectively. Absorption curves reveal that after the initial absorption there is a continually increasing non-linearly, with an upward curvature trend with square \sqrt{t} (Schoelkopf *et al.* 2002). Furthermore, curves show that samples did not reach water saturation.

These effects are related to the swelling of MNFC which is assumed to act to block pores, and so prevents further water absorption (Gane and Koivunen 2010). Short, mid and long timescale absorption rates for water uptake (Ridgway *et al.* 2006) can, however, be derived prior to the deviation from linearity and are presented in Fig. 61c).

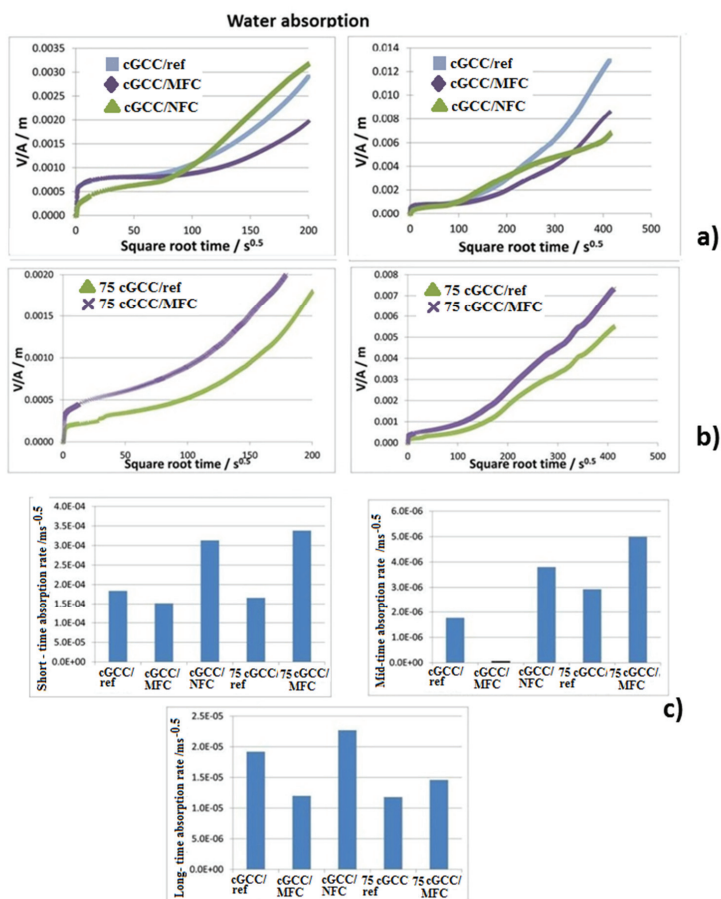


Figure 61 Water absorption curves: a) absorption curves for the 100 % cGCC samples, up to 200 s^{0.5} and up to 400 s^{0.5}, b) absorption curves for the 75cGCC samples up to 200 s^{0.5} and up to 400 s^{0.5}, c) short time absorption rate (up to 2 s^{0.5}), mid time scale (greater than 20 s^{0.5} and less than 80 s^{0.5}) and long timescale absorption rates (over time scale greater than 120 s^{0.5} and less than 180 s^{0.5}) (Publication V).

The time over which the liquid in contact with the tablet sample underwent absorption differed between the first ($n = 1$) and second ($n = 2$) repeated absorption experiments. Values of the ratio of the volume occupied by the liquid, calculated from Eq. 53 and Eq 54, in each water absorption run, to the available volume before any absorption had taken place, are shown in Fig. 62.

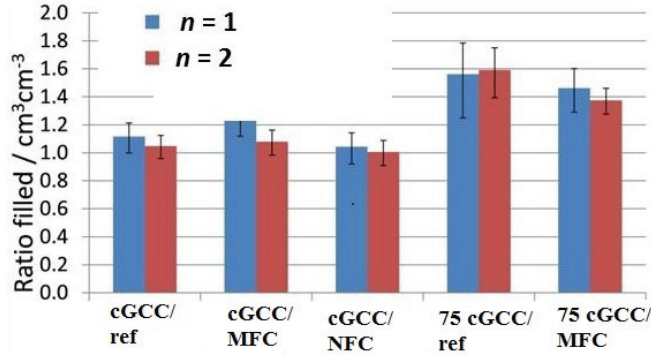


Figure 62 Ratio of volume filled by water in the tablet samples up to the wetting length at cessation of the first and second absorptions compared with the available pore volume in that same length of the original sample before wetting measured by mercury porosimetry. Error bars are derived from the estimated error of length measurement of the observed saturated absorption region (± 1 mm) (Publication V).

Presence of MFC and presence of kaolin in both the Reference and the MFC containing sample increases available pore volume for water to that of mercury intrusion, Table 14. The clay samples have the ratio of volume filled by water compared to initial pore volume $\gg 1$, and this suggests that the water is finding a preferred pathway through the structure and opening (increasing) the connectivity. The cGCC/ref sample shows the expected unchanged porosity after the first absorption wetting compared with the second absorption (ratio =1). The presence of MFC was one major factor in showing strong water interaction with the structure and the clearly observed tendency to deliver an apparently greater pore volume available for saturation than suggested by mercury intrusion and during saturation using the inert alkane.

Table 14 Summary of water absorption pore filling volume ratios, and comparison with mercury intrusion and hexadecane pore filling values (Publication V).

1 st Absorption Dried 2 nd Absorption	WATER						Specific pore volume	
	1 st absorption	2 nd absorption	1 st absorption	2 nd absorption	1 st absorption	2 nd absorption	Hexadecane (inert)	Hg
	Length proportion filled with water after fixed time		Volume of water absorbed per unit sample weight		Volume of water absorbed per unit initial pore volume (>1 => dissolution of skeletal material or swelling)		Volume filled at saturation per unit sample weight	
	l/L		$(\text{cm}^3 \text{g}^{-1})$		$V_{\text{liq}}/V_{\text{Hg pores}}$		$(\text{cm}^3 \text{g}^{-1})$	
cGCC/ref	0.83	1.00	0.08	0.09	1.12	1.05	0.10	0.09
cGCC/MFC	0.74	1.00	0.08	0.09	1.28	1.08	0.09	0.08
cGCC/NFC	0.84	1.00	0.08	0.09	1.04	1.01	0.09	0.09
75cGCC/ref	0.48	0.72	0.07	0.10	1.56	1.59	0.10	0.09
75 cGCC/MFC	0.52	0.83	0.07	0.10	1.46	1.38	0.10	0.09

4.3.5 Extractives present in MNFC containing coatings

Liquid water left remaining after the absorption into the tablet samples containing MFC as co-binder contained a sticky mass upon drying. The resulting FTIR spectrum, derived from the remaining sticky material, is shown in Fig. 63, and, when compared with a typical cellulose spectrum (Yang *et al.* 2007) indicated no significant trace of cellulose in the extractives. Rather, a mix of inorganic salts/minerals, especially sodium carbonate and sulphates, was found. These are remaining residues from Kraft pulping prior to production of the MFC, which could not be filtered afterwards due to the gel-like nature, and eventually affecting flocculation within the coating colour matrix. High flocculation of pigments in the presence of this increased ion concentration provides readily an alternative or additional reason for the larger pore sizes seen in the porosimetry analysis, as well as the greater connectivity seen during the absorption of inert liquid and the disorientation of the clay platelets in the microscopic images leading to the action of the liquid revealing a preferred pathway.

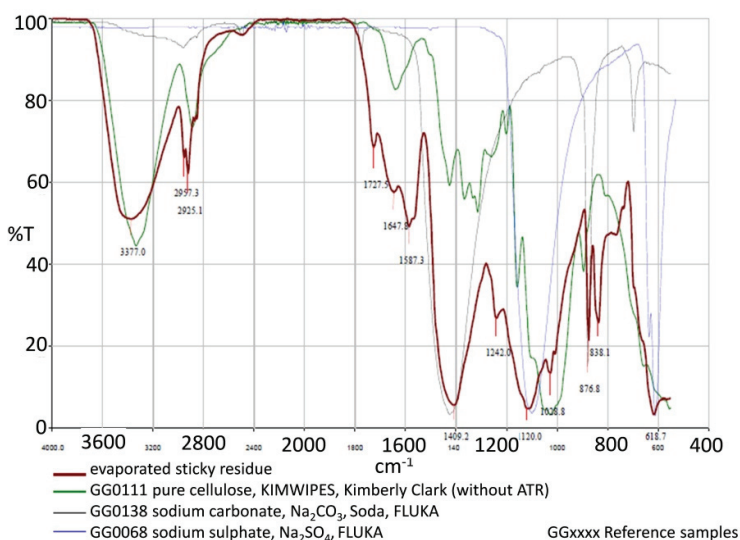


Figure 63 FTIR-spectra in attenuated total reflection (ATR) analysis of remaining residue in the absorption water reservoir after absorption experiments into MFC-containing structures (Publication V).

4.3.6 Selective permeability of MNFC containing coatings

As seen from Fig. 63 it is impossible to saturate MNFC containing samples with water despite their porous nature. This suggests that swelling of the nanocellulose acts to block the pores within the structure, making them impermeable to liquid water.

After three days of water absorption, the MNFC containing tablets still displayed incomplete saturation. Nonetheless, the samples were mounted for the permeation experiments in the permeability measurement cell presented in Fig. 30, but there was no measurable volume of water passed through the samples, showing complete impermeability of the samples to water. The permeability of the samples, though very low, were, however, measured successfully with the inert hexadecane (Ghosh *et al.* 1997, Ridgway *et al.* 2006, Ridgway *et al.* 2011) and 0.3 – 0.5 g of fluid had come through the sample giving Darcy permeation constants $\sim 10^{-18} \text{ m}^2$, Fig. 64.

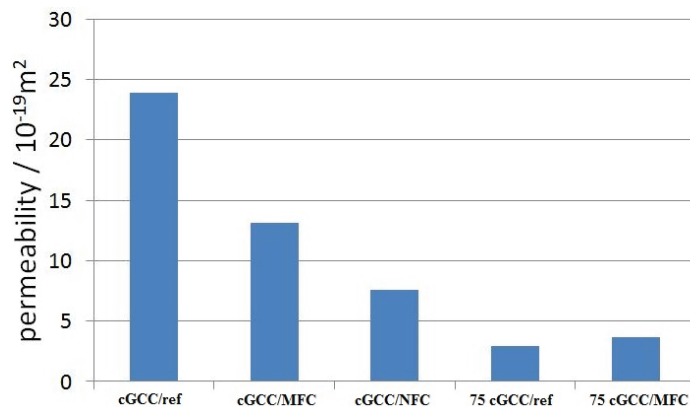


Figure 64 Permeability of tablet samples using hexadecane as the permeation fluid (Publication V).

From Fig. 64, we see that, although the permeabilities are generally low, a coarse blocky pigment in a standard reference formulation of CMC and latex (cGCC/ref) shows the highest permeability, while addition of MFC reduces permeability somewhat and NFC¹ more so. The presence of clay, with its tortuous path-creating structure related to the platy particle nature, leads to the greatest reduction in permeability.

5 Conclusions

The general approach of this thesis is focused on rheological determination of MNFC suspensions and their influence on developing novel and advanced papermaking formulations.

There is a difference in rheology between MFC and NFC due to differences in their flocculation state, aspect ratio, and swelling degree of fibres, all of which affect mobility within the suspension through the size and elasticity of aggregates and the strength of the water binding gel structure. On (i) the molecular scale, it is related to colloidal interactions between particles, i.e. the electrostatic and dispersion effect between fibrils, on (ii) the microscopic scale, it depends on the amount of reactive groups on the fibre surface controlling the amount of bound water developing the balance between lubrication of the fibrils at low solids and gel formation at higher solids, and on (iii) the macroscopic scale, it is related to flow uniformity, wall slip, thixotropy and aging/rejuvenation, primarily related to the phase separable nature of the gel structures formed and the entanglement and flocculation of residual fibrous components.

In the **Publication I** are identified several challenging issues with the associated measurement of the rheological and dewatering properties of MNFC suspensions and furnishes. MNFC containing furnish properties are effectively determined by those of the corresponding nanofibrillar suspensions alone.

The novel method of determining the immobilisation interval between the onset of immobilisation and the final immobilisation point, defined as the time difference between the first derivative zeros of the loss factor with respect to time, allows us to quantify the difference in the dewatering behaviour of high consistency nanocellulose based furnishes through changes in the viscoelastic character of the furnishes. The immobilisation intervals of the two types of MNFC differ considerably, which is an important factor when trying to optimise the dewatering kinetics. Much longer immobilisation intervals were observed for NFC based materials, the immobilisation starting later than in the case of MFC based materials due to the fact that in this case, the water is effectively immobilised both within and between the nanofibres instead of being held in the voids between contacting particles during the traditional mechanical slip-stick transition at immobilisation.

In the **Publication II** there is an introduction of a novel application of shear and vacuum dewatering of high consistency MNFC containing furnishes. The implementation of rotation cycles in between the oscillation vacuum cycles was found to increase the final solids content of the samples with small difference in the final solids content between different MNFC type and the presence of cellulose fibres. During the dewatering measurement, the solids content of the sample increases with an increase in yield stress and the shear thinning behaviour of the furnish, which shows an important relationship to the structure development during dewatering. The shear thinning is almost without exception related to the breakage of the suspension internal gel-like structure (**Publication I**), freeing parts of the internally bound/isolated water. Free water can then be easily removed from the fluid by a simple vacuum suction. However, there are limitations related to this method. Firstly, the Weissenberg effect, which tends to

distribute the solids on the rheometer plate unevenly, and which increases with the shear rate. Secondly, as the structure of the solid phase is broken into small parts there is a risk that these penetrate the cake and the filter, therefore reducing the solids retention.

The main questions addressed in **Publication III** were whether the partial substitution of CMC with MNFC would allow the introduction of new types of rheology modifiers in coating colours, which could bring improved strength properties and levelling on the paper surface. Retained fibrous material becomes swollen in water, and the nanofibrillar fraction forms a gel structure containing water within the nanoporous structure. The difference in rheological and dewatering behaviour for MNFC based coating is not affected directly by the pigment type, i.e. pigment or pigment blend in the coating formulation.

MNFC based coatings are predicted to show a tendency to sagging, related to the lack of flocculation of the pigment/latex and so a slow elastic recovery time, but have good levelling characteristics as they have flow mobility as well as improved freedom for diffusion compared to CMC coatings. Both gravimetric and dynamic dewatering results show a decrease in water retention properties for coating colours which have MNFC as part of the co-binder. A resultant too rapid dewatering, however, could cause problems as dewatering rate is one of the most important factors controlling formation of coating structure. However, the more rapid dewatering could allow the immobilisation to be rapidly implemented and so sagging reduced if high enough solids concentration can be applied.

Partial and total substitution of CMC with MFC/NFC as part of the coating formulation is examined in **Publication IV**. As concluded in **Publications I and III** MNFC builds a gel-like structure with water, and this modifies the traditional rheological behaviour of pigment and latex dispersions especially in the presence of pigment/latex flocculating polymers, such as CMC (**Publication III**). CMC is seen additionally to disperse MNFC, and its absence leads to an agglomeration tendency of the nanofibrillar component, reducing its ability to retain water in the matrix, but in contrast the pigment/latex becomes more stably dispersed when CMC is removed. This study identifies the importance of the presence of a small amount of polymer thickener in the coating colour recipe when MNFC is used as co-binder. This is to ensure the minimal amount of pigment/latex flocculation. The need for flocculation of pigment/latex to be present is to generate pigment-related water retention and rapid elasticity recovery in the colour independently of the MNFC contained in the coatings. This is particularly important when used, for example, on slow coating machines and permeable substrates.

In **Publication V** we analyse the pore structure of pigmented coatings, liquid absorption and permeability, in respect to the influence of partially substituting traditional co-binder carboxymethyl cellulose (CMC) with MNFC. To define the formation of the coating structure we connect rheological and immobilisation behaviour of the coating colour suspensions to the final pore structure (**Publication III**). The impact of flocculation versus dispersion of the suspension components defines the consolidation density of the final coating layer. The contrasting behaviour between polar water and non-polar oil, exemplified by alkane, is used to probe and isolate the water interactive and in-coating (internal) gel formation of the nanocellulosic material. Results show that the presence of nanocellulosic materials acts to reduce permeability of coatings dramatically, through the internal nanocellulose gel network. The exposure to water is seen to generate effective excess pore volume, especially in the presence of MFC and/or clay. This we conclude to

be related to the swelling tendency of the MNFC and the observation of extractives considered to derive from the presence of inorganic salts retained from Kraft pulp during the MFC production. Inert alkane, on the other hand, can absorb and permeate freely with no extractive effect.

In **Publication VI** the Brookfield viscometer is used as a model resembling vane bucket geometry to study MNFC suspension rheology. Using the combination of vane spindle and wide gap, the problems related to wall slip due to the fibres sticking in between the vanes and forming a discontinuous network compared to the bulk material were avoided. Shear localisation is taken into account, and, by applying a correction algorithm (Coussot 2005; Ovarlez *et al.*, 2008), it was observed that correction of flow curves makes a significant difference to the original results obtained in this geometry. Here the assumption was made that the steady state is unique and lies between the shear up and shear down measurements as would be assumed based on various models for complex fluids at sufficiently long waiting times (Mewis and Wagner, 2009).

5.1 Future work

The novel findings surrounding the nanocellulose fraction of MNFC in this thesis, specifically referring to the gel effect and the differentiating properties in interaction with polar and non-polar liquids, opens a wide field for potential further research. For example:

- the predictions from the rheological analyses that the viscoelastic properties being significantly different between MNFC containing and traditional CMC coating formulations would lead to different levelling and runnability properties could provide for new applications, such as improved levelling properties when used in topcoats;
- that MNFC on rewetting swells within coating structures in contact with water, but not with alkane, could provide new developments in respect to liquid separation technologies;
- differential flocculation between the action of CMC on MNFC acting as dispersant and on pigments/latex acting as flocculant could enable the construction of new fluidic additives based on nanocellulose for a range of engineering fluids in general.

These ideas by no means reflect the full development potential of MNFC when considered in combination with chosen co-materials, especially in colloidal systems technologies.

6 References

- Abe S, Mair K (2005) Grain fracture in 3D numerical simulations of granular shear. *Geophys Res Lett* 32
- Adams J (1993) Particle size and shape effects in materials science: examples from polymer and paper systems. *Clay Miner* 28:509-530
- Agoda-Tandjawa G, Durand S, Berot S, Blassel C, Gaillard C, Garnier C, Doublier J (2010) Rheological characterization of microfibrillated cellulose suspensions after freezing. *Carbohydr Polym* 80:677-686
- Aidun CK, Triantafillopoulos NG (1997) High-speed blade coating. In: *Liquid film coating*. Springer, pp 637-672
- Al-Hadithi T, Barnes H, Walters K (1992) The relationship between the linear (oscillatory) and non-linear (steady-state) flow properties of a series of polymer and colloidal systems. *Colloid and Polymer Science* 270:40-46
- Allen L (1979) Characterization of colloidal wood resin in newsprint pulps. *Colloid and Polymer Science* 257:533-538
- Al-Turaif H, Bousfield DW, LePoutre P (2002) The influence of substrate absorbency on coating surface chemistry. *Progress in organic coatings* 44:307-315
- Androusoy G, Mann R (1979) Evaluation of mercury porosimeter experiments using a network pore structure model. *Chemical Engineering Science* 34:1203-1212
- Aradian A, Cates M (2006) Minimal model for chaotic shear banding in shear thickening fluids. *Physical Review E* 73:041508
- Astarita G (1990) Letter to the Editor: The engineering reality of the yield stress. *Journal of Rheology* 34:275
- Astarita G, Marrucci G (1974) *Principles of non-Newtonian fluid mechanics*. McGraw-Hill, New York 154-227
- Aulin C, Ahola S, Josefsson P, Nishino T, Hirose Y, Österberg M, Wågberg L (2009) Nanoscale Cellulose Films with Different Crystallinities and Mesostructures: Their Surface Properties and Interaction with Water. *Langmuir* 25:7675-7685
- Ayol A, Dentel SK, Filibeli A (2010) Rheological characterization of sludges during belt filtration dewatering using an immobilization cell. *Journal of Environmental Engineering* 136:992-999
- Barbista F, Bousfield DW, Rigdahl M (2001) Modeling of rheological properties of coating colors. *Journal of Rheology* 45:139
- Barbista F, Bousfield DW, Rigdahl M (2001) Modeling of rheological properties of coating colors. *Journal of Rheology* 45:139
- Barnes HA, Nguyen QD (2001) Rotating vane rheometry—a review. *Journal of Non-Newtonian Fluid Mechanics* 98:1-14

- Barnes HA (1995) A review of the slip (wall depletion) of polymer solutions, emulsions and particle suspensions in viscometers: its cause, character, and cure. *Journal of Non-Newtonian Fluid Mechanics* 56:221-251
- Barnes HA (1989) Shear-thickening (“dilatancy”) in suspensions of non-aggregating solid particles dispersed in Newtonian liquids. *Journal of Rheology* 33:329
- Barnes HA (2007) The 'yield stress myth?' paper - 21 years on. *Applied Rheology* 17:43110-1-43100-5
- Barnes HA, Hutton JF, Walters K (1989) *An introduction to rheology*. Elsevier
- Baslingappa Swami S, Das S, Maiti B (2004) Effect of water and air content on the rheological properties of black gram batter. *Journal of Food Engineering* 65:189-196
- Beghello L, Eklund D (1999) Influence of the chemical environment on fibre flocculation. *J Pulp Paper Sci* 25:246-250
- Beghello L, Lindström T (1998) The influence of carboxymethylation on the fiber flocculation process. *Nordic Pulp & Paper Research Journal* 13:269-273
- Bennington C, Kerekes R, Grace J (1990) The yield stress of fibre suspensions. *The Canadian Journal of Chemical Engineering* 68:748-757
- Berg C, Åkerholm J, Karlsson M (2001) An experimental evaluation of the governing moisture movement phenomena in the paper coating process. I. Theoretical aspects. *Drying Technology* 19:2389-2406
- Bertola V, Bertrand F, Tabuteau H, Bonn D, Coussot P (2003) Wall slip and yielding in pasty materials. *Journal of Rheology* 47:1211
- Bingham EC (1922) *Fluidity and plasticity*. McGraw-Hill, New York
- Björkman U (2003) Break-up of suspended fibre networks. *Nordic Pulp & Paper Research Journal* 18:32-37
- Björkman U (2005) Floc dynamics in flowing fibre suspensions. *Nordic Pulp & Paper Research Journal* 20:247-252
- Björkman U (2008) The non-linear history of fibre flow research. Part 2: Continuation, reflections and suggestions. *Applied Rheology* 18
- Bobkowicz A, Gauvin W (1965) The turbulent flow characteristics of model fibre suspensions. *The Canadian Journal of Chemical Engineering* 43:87-91
- Boger D, Hur D, Petrie C (1990) The rheology of fibre suspensions. *Third European Rheology Conference and Golden Jubilee Meeting of the British Society of Rheology*: 4-5
- Bossard F, Moan M, Aubry T (2007) Linear and non-linear viscoelastic behavior of very concentrated plate-like kaolin suspensions. *Journal of Rheology* 51:1253
- Bousfield D W, Saucier R, Sahlberg T, Hayes P (2008) Short-time coating dewatering: a novel test method and model. *Advanced TAPPI Coating Fundamentals / aspx 08ADV35*

- Bousfield D W (2008) Rheological issues in the paper industry. *Rheology reviews. British Society of Rheology*: 47-70
- Bousfield D W, Co A (1999) Paper coating rheology. *Rheology Series (Advances in the Flow and Rheology of Non-Newtonian Fluids)* 9:827-842
- Brecht W, Heller H (1950) A study of the pipe friction losses of paper stock suspensions. *Tappi Journal* 33:14A-48A
- Brummer R (2006) *Rheology essentials of cosmetic and food emulsions*. Springer, Berlin
- Brunauer S, Emmett PH, Teller E (1938) Adsorption of gases in multimolecular layers. *Journal of the American Chemical Society* 60:309-319
- Bulota M (2012) Deformation and fracture mechanisms in nanocellulose reinforced composites. Doctoral dissertation, Aalto University publication series 109/2012
- Buri M, Gane PAC, Blum RV (2012) Composites of inorganic and/or organic microparticles and nano-dolomite particles. EP Patent 2.038.350
- Carreau P, Kee DD, Daroux M (1979) An analysis of the viscous behaviour of polymeric solutions. *The Canadian Journal of Chemical Engineering* 57:135-140
- Celzard A, Fierro V, Kerekes R (2009) Flocculation of cellulose fibres: new comparison of crowding factor with percolation and effective-medium theories. *Cellulose* 16:983-987
- Chen H, Park A, Heitmann JA, Hubbe MA (2009) Importance of cellulosic fines relative to the dewatering rates of fiber suspensions. *Industrial and Engineering Chemistry Research* 48:9106-9112
- Cheng DC (1986) Yield stress: a time-dependent property and how to measure it. *Rheologica Acta* 25:542-554
- Chhabra RP, Richardson JF (2011) *Non-Newtonian flow and applied rheology: engineering applications*. Butterworth-Heinemann
- Chi H, Li H, Liu W, Zhan H (2007) The retention and drainage-aid behavior of quaternary chitosan in papermaking system. *Colloids and Surfaces A: Physicochemical and Engineering Aspects* 297:147-153
- Corrêa AC, de Moraes Teixeira E, Pessan LA, Mattoso LHC (2010) Cellulose nanofibers from curaua fibers. *Cellulose* 17:1183-1192
- Coussot P (2005) *Rheometry of pastes, suspensions, and granular materials: applications in industry and environment*. John Wiley and Sons, New Jersey
- Coussot P, Nguyen QD, Huynh H, Bonn D (2002) Viscosity bifurcation in thixotropic, yielding fluids. *Journal of Rheology* 46:573-589
- Cox W, Merz E (1958) Correlation of dynamic and steady flow viscosities. *Journal of Polymer Science* 28:619-622
- Cui H, Grace JR (2007) Flow of pulp fibre suspension and slurries: A review. *International Journal of Multiphase Flow* 33:921-934

- Curvers D, Usher SP, Kilcullen AR, Scales PJ, Saveyn H, Van der Meeren P (2009) The influence of ionic strength and osmotic pressure on the dewatering behaviour of sewage sludge. *Chemical Engineering Science* 64:2448-2454
- Da Cruz F, Chevoir F, Bonn D, Coussot P (2002) Viscosity bifurcation in granular materials, foams, and emulsions. *Physical Review E* 66:051305
- Dahlvik P, Ström G, Eklund D (1997) Variations in calcium ion concentration and pH influencing coating colour rheology, dewatering and immobilization. *Nordic Pulp and Paper Research Journal* 12(1):61-66
- Dahlvik P, Ström G, Karathanasis M, Hermansson E, Eklund D (1996) Interactions in Coating Colors induced by Temperature-Sensitive Cellulosic Polymer. Conference proceedings, Paper and Coating Chemistry Symposium Canada, Conference proceedings: 155-162
- Dalpke B, Kerekes R (2005) The influence of fibre properties on the apparent yield stress of flocculated pulp suspensions. *Journal of Pulp and Paper Science* 31:39-43
- Deka A, Dey N (2012) Rheological studies of two component high build epoxy and polyurethane based high performance coatings. *Journal of Coatings Technology and Research* 10 (3): 305-315
- Derakhshandeh B, Kerekes R, Hatzikiriakos S, Bennington C (2011) Rheology of pulp fibre suspensions: A critical review. *Chemical Engineering Science* 66:3460-3470
- Derjaguin B (1941) Theory of the stability of strongly charged lyophobic sols and the adhesion of strongly charged particles in solutions of electrolytes. *Acta Physicochim. USSR* 14:633-662
- Dickinson E, Chen J (1999) Heat-set whey protein emulsion gels: role of active and inactive filler particles. *Journal of Dispersion Science and Technology* 20:197-213
- Divoux T, Grenard V, Manneville S (2013) Rheological hysteresis in soft glassy materials. *Physical Review Letters* 110:018304(1-5)
- Divoux T, Tamarii D, Barentin C, Manneville S (2010) Transient shear banding in a simple yield stress fluid. *Physical Review Letters* 104:208301(1-4)
- Doraiswamy D, Mujumdar A, Tsao I, Beris A, Danforth S, Metzner A (1991) The Cox–Merz rule extended: a rheological model for concentrated suspensions and other materials with a yield stress. *Journal of Rheology* 35:647-685
- Ducker WA, Senden TJ, Pashley RM (1991) Direct measurement of colloidal forces using an atomic force microscope. *Nature* 353:239-241
- Dullaert K, Mewis J (2006) A structural kinetics model for thixotropy. *Journal of Non-Newtonian Fluid Mechanics* 139:21-30
- Dzuy NQ, Boger DV (1983) Yield stress measurement for concentrated suspensions. *Journal of Rheology* 27:321-349
- Einstein A (1906) A new determination of molecular dimensions. *Annalen der Physik* 19:289-306

- Eklund D, Salminen P (1986) Water transport in the blade coating process. *Tappi J* 69:116-119
- Ercili-Cura D, Lille M, Legland D, Gaucel S, Poutanen K, Partanen R, Lantto R (2012) Structural mechanisms leading to improved water retention in acid milk gels by use of transglutaminase. *Food Hydrocolloids* 30: 419-427
- Evans ID (1992) Letter to the editor: On the nature of the yield stress. *Journal of Rheology* 36:1313-1316
- Fadat G, Engström G, Rigdahl M (1988) The effect of dissolved polymers on the rheological properties of coating colours. *Rheologica acta* 27:289-297
- Fall AB, Lindström SB, Sundman O, Ödberg L, Wågberg L (2011) Colloidal Stability of Aqueous Nanofibrillated Cellulose Dispersions. *Langmuir* 27:11332-11338
- Fend M, Liu Y, Guo Y, Dou X (2007) Influence of CMC Content on Properties of Coating Color and Coated Paper [J]. *Paper Chemicals* 4:013
- Fenistein D, van Hecke M (2003) Kinematics: Wide shear zones in granular bulk flow. *Nature* 425:256-256
- Fisher ME, Barber MN (1972) Scaling theory for finite-size effects in the critical region. *Physics Review Letters* 28:1516-1519
- Flory, PJ (1953) *Principles of polymer chemistry*. Cornell University Press
- Forsström U (2009) Base Paper, in *Pigment Coating and Surface Sizing of Paper*, (Ed) J Paltakari, *Paperi ja Puu Oy* 3:42-59
- Franco J, Gallegos C, Barnes H (1998) On slip effects in steady-state flow measurements of oil-in-water food emulsions. *Journal of Food Engineering* 36:89-102
- Gane PAC (1997) Relaxation-Induced Dilatancy in Separable Visco-Elastic Suspensions: proposing a novel rheological phenomenon. A paper presented at the Tappi Advanced Coating Fundamentals Symposium, Philadelphia, Conference Proceedings, Tappi Press, Atlanta: 73-82
- Gane PAC (2009) Pigments, In *Pigment Coating and Surface Sizing of Paper* Ed (Paltakari J), *Paperi ja Puu Oy*, 5: 339-430
- Gane PAC, Kettle JP, Matthews GP, Ridgway CJ (1996) Void space structure of compressible polymer spheres and consolidated calcium carbonate paper-coating formulations. *Industrial and Engineering Chemistry Research* 35:1753-1764
- Gane PAC (2009) *Paper Coating Technology*, Lecture notes. Aalto University (Helsinki University of Technology)
- Gane PAC, Hooper JJ, Grunwald A (1997) Coating pigment orientation: a comparative analysis of the application mechanisms and properties of blade and roll coatings. *Tappi Journal* 80:109-115
- Gane PAC, Ridgway CJ, Schoelkopf J (2004) Absorption rate and volume dependency on the complexity of porous network structures. *Transport in Porous Media* 54:79-106

- Gane PAC, Burri P, Spielmann D, Drechsel J, Reimers O (1997) Formulation Optimisation for Improved Runnability of High Speed Pigmented Coatings on the Metered Size Press. TAPPI Coating Conference, Conference proceedings:15-22
- Gane PAC, Coggon L (1987) Coating blade geometry: its effect on coating color dynamics and coated sheet properties. Tappi Journal 70:87-96
- Gane PAC, Hooper JJ (1989) An evaluation of interactions between coating color and basepaper by coating profile analysis. Fundamentals of Papermaking 2:871-893
- Gane PAC, Koivunen K (2010) Relating liquid location as a function of contact time within a porous coating structure to optical reflectance. Transport in Porous Media 84:587-603
- Gane PAC, McGenity PM, Watters P (1992) Factors influencing the runnability of coating colors at high speed. Tappi Journal 75:61-73
- Gane PAC, Ridgway C, Barcelo E (2006) Analysis of pore structure enables improved tablet delivery systems. Powder Technol 169:77-83
- Gane PAC, Ridgway CJ, Lehtinen E, Valiullin R, Furo I, Schoelkopf J, Paulapuro H, Daicic J (2004) Comparison of NMR cryoporometry, mercury intrusion porosimetry, and DSC thermoporosimetry in characterizing pore size distributions of compressed finely ground calcium carbonate structures. Industrial and Engineering Chemistry Research 43:7920-7927
- Geankoplis CJ (1983) Transport Processes and Unit Operations. PTR Prentice Hall (Engelwood Cliffs, N.J)
- Gerstner P (2010) Heat transfer through porous multiphase systems: measurement, modelling and applications in printing of coated papers. Doctoral dissertation, Aalto University (Helsinki University of Technology) 1797-5093
- Ghosh T, Lavoine PA, Carreau P (1997) Rheology of coating colors and their runnability on a cylindrical laboratory coater. TAPPI Journal 80:11-34
- Gisler T, Ball RC, Weitz DA (1999) Strain hardening of fractal colloidal gels. Physical Review Letters 82:1064
- Greenwood R, Bergström L (1997) Electroacoustic and rheological properties of aqueous Ce-ZrO₂ (Ce-TZP) suspensions. Journal of the European Ceramic Society 17: 537-548.
- Grön J, Salminen J, Toivakka M, Paltakari J (2009) Coating layer consolidation and formation of the coating layer structure, In Pigment coating and surface sizing of paper (Ed) J Paltakari, Paperi ja Puu Oy 11:356-390
- Hamaker H (1937) The London—van der Waals attraction between spherical particles. Physica 4:1058-1072
- Hanciogullari H (2009) Co-binders and Thickeners, In Pigment Coating and Surface Sizing of Paper (Ed) J Paltakari, Paper ja Puu Oy: 228-267

- Hatakeyama T, Inui Y, Iijima M, Hatakeyama H (2013) Bound water restrained by nanocellulose fibres. *Journal of Thermal Analysis and Calorimetry* 113:1019-1025
- Hatakeyama T, Nakamura K, Hatakeyama H (1988) Determination of bound water content in polymers by DTA, DSC and TG. *Thermochimica Acta* 123:153-161
- Heirman G, Vandewalle L, Van Gemert D, Wallevik O (2008) Integration approach of the Couette inverse problem of powder type self-compacting concrete in a wide-gap concentric cylinder rheometer. *Journal of Non-Newtonian Fluid Mechanics* 150:93-103
- Henriksson G, Brännvall E, Lennhol H (2009) The trees, Chapter 2. In: *Pulp and Paper Chemistry and Technology Volume 1, Wood Chemistry and Wood Biotechnology* (Eds. M Ek, G Gellerstedt, G Henriksson), Walter de Gruyter, Berlin, pp. 13–44.
- Henriksson M, Henriksson G, Berglund L, Lindström T (2007) An environmentally friendly method for enzyme-assisted preparation of microfibrillated cellulose (MFC) nanofibers. *European Polymer Journal* 43:3434-3441
- Herrick FW, Casebier RL, Hamilton JK, Sandberg KR (1983) Microfibrillated cellulose: morphology and accessibility. *Journal of Applied Polymer Science, Applied Polymer Symposium* 37:conf.8205294
- Hodges C (2002) Measuring forces with the AFM: polymeric surfaces in liquids. *Advances in Colloid and Interface Science* 99:13-75
- Horvath AE, Lindström T (2007) The influence of colloidal interactions on fiber network strength. *Journal of Colloid and Interface Science* 309:511-517
- Hu H, Larson R, Magda J (2002) Measurement of wall-slip-layer rheology in shear-thickening wormy micelle solutions. *Journal of Rheology* 46:1001
- Hubbe MA (2007) Flocculation and redispersion of cellulosic fiber suspensions: a review of effects of hydrodynamic shear and polyelectrolytes. *BioResources* 2:296-331
- Hubbe MA, Chen H, Heitmann JA (2009) Permeability reduction phenomena in packed beds, fiber mats, and wet webs of paper exposed to flow of liquids and suspensions: A review. *BioResources* 4:405-451
- Hubbe MA, Panczyk M (2007) Dewatering of refined, bleached hardwood kraftpulp by gravity, vacuum, and centrifugation with applied pressure Part 2. Effects of wet-end additives. *O Papel (Brazil)* 68:88-100
- Hubbe MA, Rojas OJ, Lucia LA, Sain M (2008) Cellulosic nanocomposites: a review. *BioResources* 3:929-980
- Hult E, Iotti M, Lenés M (2010) Efficient approach to high barrier packaging using microfibrillar cellulose and shellac. *Cellulose* 17:575-586
- Husband J (1998) Adsorption and rheological studies of sodium carboxymethyl cellulose onto kaolin: effect of degree of substitution. *Colloids Surf A: Physicochemical and Engineering Aspects* 134:349-358
- Husband, JC, Adams, JM (1993) Interactions in rotogravure coating colours containing clay and alkali thickening latices, *Tappi Coating Conference Proc.*, Tappi Press:207-221

- Illa X, Puisto A, Lehtinen A, Mohtaschemi M, Alava MJ (2013) Transient shear banding in time-dependent fluids. *Physical Review Letters* E 87:022307
- Iotti M, Gregersen Ø W, Moe S, Lenes M (2011) Rheological Studies of Microfibrillar Cellulose Water Dispersions. *Journal of Polymers and the Environment* 19:137-145
- Irmay S (1958) On the theoretical derivation of Darcy and Forchheimer formulas. *Transactions, American Geophysical Union* 39:702-707
- Isogai A, Saito T, Fukuzumi H (2011) TEMPO-oxidized cellulose nanofibers. *Nanoscale* 3:71-85
- Israelachvili J, Wennerström H (1996) Role of hydration and water structure in biological and colloidal interactions. *Nature* 379: 219-225
- Israelachvili J N (2011) *Intermolecular and surface forces: revised third edition*. Elsevier Inc.
- Iwamoto S, Abe K, Yano H (2008) The effect of hemicelluloses on wood pulp nanofibrillation and nanofiber network characteristics. *Biomacromolecules* 9:1022-1026
- Iyer R R, Bousfield D W (1996) The leveling of coating defects with shear thinning rheology. *Chemical engineering science* 51:4611-4617
- Jäder J, Järnström L (2001) Calculation of filter cake thickness under condition of dewatering under shear. *Annual transactions of the Nordic Rheology Society* 9:113-117
- Jäder J, Järnström L (2003) The Influence of thickener addition on filter cake formation during Dewatering of Mineral Suspensions. *Applied Rheology* 13:125-131
- Jin H, Kettunen M, Laiho A, Pynnönen H, Paltakari J, Marmur A, Ikkala O, Ras RH (2011) Superhydrophobic and superoleophobic nanocellulose aerogel membranes as bioinspired cargo carriers on water and oil. *Langmuir* 27:1930-1934
- Jones D S, Woolfson A D, Brown A F (1997) Textural, viscoelastic and mucoadhesive properties of pharmaceutical gels composed of cellulose polymers. *International Journal of Pharmaceutics* 151:223-233
- Karppinen A, Vesterinen A H, Saarinen T, Pietikäinen P, Seppälä J (2011) Effect of cationic polymethacrylates on the rheology and flocculation of microfibrillated cellulose. *Cellulose* 18:1381-1390
- Katchalsky A, Lifson S, Exsenberg H (1951) Equation of swelling for polyelectrolyte gels. *Journal of Polymer Science* 7:571-574
- Kavanagh G M, Ross-Murphy S B (1998) Rheological characterisation of polymer gels. *Progress in Polymer Science* 23:533-562
- Kerekes R, Harvey D (1980) TAPPI Fluid Mechanics Committee drainage tester survey. *TAPPI Journal* 63: 89-91
- Kerekes R, Schell C (1992) Characterization of fibre flocculation regimes by a crowding factor. *Journal of Pulp and Paper Science* 18:J32-J38

- Kerekes R, Soszynski R, Doo T (1985) The flocculation of pulp fibres, In Papermaking Raw Materials: Their Interaction with the Production Process and their Effect on Paper Properties. Transactions of the Eighth Fundamental Research Symposium held at Oxford: 265-310
- Keshtkar M, Heuzey M, Carreau P (2009) Rheological behavior of fiber-filled model suspensions: effect of fiber flexibility. *Journal of Rheology* 53:631
- Kettle J, Lamminmäki T, Gane P (2010) A review of modified surfaces for high speed inkjet coating. *Surface and Coatings Technology* 204:2103-2109
- Kettunen M (2013) Cellulose Nanofibrils as a Functional Material. Doctoral dissertation, Aalto University of Technology 114/2013
- Kimura M, Hatakeyama H, Usuda M, Nakano J (1972) Studies on absorbed water in cellulose by broad-line NMR. *Journal of Applied Polymer Science* 16:1749-1759
- Klein CO, Spiess HW, Calin A, Balan C, Wilhelm M (2007) Separation of the non-linear oscillatory response into a superposition of linear, strain hardening, strain softening, and wall slip response. *Macromolecules* 40:4250-4259
- Klemm D, Kramer F, Moritz S, Lindström T, Ankerfors M, Gray D, Dorris A (2011) Nanocelluloses: A New Family of Nature-Based Materials. *Angewandte Chemie International Edition* 50:5438-5466
- Klemm D, Schumann D, Kramer F, Heßler N, Koth D, Sultanova B (2009) Nanocellulose materials—different cellulose, different functionality 280:60-71
- Kloow G, Tran T, Hentschel P, Hanciogullari H (2009) Co-binders and Thickeners, In *Pigment Coating and Surface Sizing of Paper* (Ed) J Paltakari, Paper ja Puu Oy: 228-267
- Kugge C (2003) Consolidation and structure of paper coating and fibre systems. Doctoral Dissertation, KTH, Stockholm 91-7283-419
- Kugge C, Vanderhoek N, Bousfield D (2011) Oscillatory shear response of moisture barrier coatings containing clay of different shape factor. *J Colloid Interface Sci* 358:25-31
- Kwongá Leong Y (1993) Rheological evidence of adsorbate-mediated short-range steric forces in concentrated dispersions. *Journal of the Chemical Society, Faraday Transactions* 89:2473-2478
- Laine J, Lindstrom T, Nordmark GG, Risinger G (2000) Studies on topochemical modification of cellulosic fibres Part 1. Chemical conditions for the attachment of carboxymethyl cellulose onto fibres. *Nordic Pulp & Paper Research Journal* 15:520-526
- Landman K, Russel W (1993) Filtration at large pressures for strongly flocculated suspensions. *Physics of Fluids A: Fluid Dynamics* 5:550-560
- Landman K, Sirakoff C, White L (1991) Dewatering of flocculated suspensions by pressure filtration. *Physics of Fluids A: Fluid Dynamics* 3:1495-1509
- Landman KA, White LR, Eberl M (1995) Pressure filtration of flocculated suspensions. *AIChE J* 41:1687-1700

Larsson K, Berglund LA, Ankerfors M, Lindström T (2012) Poly lactide latex/nanofibrillated cellulose bionanocomposites of high nanofibrillated cellulose content and nanopaper network structure prepared by a papermaking route. *Journal of Applied Polymer Science* 125:2460-2466

Larsson K, Hermansson E, Eklund D, Dahlvik P (2000) Composition, use of cellulose ether as thickening agent and production of a coated cellulose-based two-dimensional product. United States Patent No.6.123.996

Lasseuguette E, Roux D, Nishiyama Y (2008) Rheological properties of microfibrillar suspension of TEMPO-oxidized pulp. *Cellulose* 15:425-433

Laudone GM, Matthews GP, Gane PA (2006) Effect of latex volumetric concentration on void structure, particle packing, and effective particle size distribution in a pigmented paper coating layer. *Industrial & Engineering Chemistry Research* 45:1918-1923

Laudone GM, Matthews GP, Gane PAC (2004) Observation of shrinkage during evaporative drying of water-based paper coatings. *Industrial & Engineering Chemistry Research* 43:712-719

Läger J, Wollny K, Huck S (2002) Direct strain oscillation: a new oscillatory method enabling measurements at very small shear stresses and strains. *Rheologica Acta* 41:356-361

Legrand V, Hourdet D, Audebert R, Snidaro D (1998) Deswelling and flocculation of gel networks: application to sludge dewatering. *Water Research* 32:3662-3672

Lehtinen E (2000) Pigment-coated products, In *Pigment coating and surface sizing of paper* (Ed.) Jouni Paltakari, Paper ja Puu Oy 2: 30-38

Letzelter P, Eklund D (1993) Coating color dewatering in blade coaters. II: The influence of machine configuration. *Tappi Journal* 76:93-98

Li J, Tanguy P, Carreau P, Moan M (2001) Effect of thickener structure on paper-coating color properties. *Colloid and Polymer Science* 279:865-871

Liese A, Hilterhaus L (2013) Evaluation of immobilized enzymes for industrial applications. *Chemical Society Review* 42: 6236-6249

Lindström T (1985) Cellulose suspensions and polyelectrolytes - some kinetic aspects. *International Symposium on Wood and Pulping Chemistry, Canada, Conference Proceedings*: 121-122

Lindström T, Carlsson G (1982) The effect of chemical environment on fiber swelling. *Svensk Papperstidning-Nordisk Cellulosa* 85:14-20

Lohmander S (2000) The influence of particle shape of coating pigments on their packing ability and on the flow properties of coating colours. *Doctoral Dissertation, KTH Stockholm, series 2000:5*

Lukkonen Pirjo, Malonet TC, Rantanen J, Paulapuro H, Ylirusi J (2001) Microcrystalline cellulose-water interaction: a novel approach using thermoporosimetry. *Pharmaceutical Research* 18: 1562-1568

Luukko K, Maloney TC (1999) Swelling of mechanical pulp fines. *Cellulose* 6:123-136

- Maloney T, Laine J, Paulapuro H (1999) Comments on the measurement of cell wall water. *Tappi Journal* 82:125-131
- Manninen M, Nieminen K, Maloney T (2013) The swelling and pore structure of microfibrillated cellulose. 15th Fundamental Research Symposium, Cambridge, UK, Conference Proceedings: 725-738
- Marrucci G (1996) Dynamics of entanglements: A non-linear model consistent with the Cox-Merz rule. *Journal of Non-Newtonian Fluid Mechanics* 62:279-289
- Mashkour M, Kimura T, Kimura F, Tajvidi M (2014) Tunable self-assembly of cellulose nanowhiskers and polyvinyl alcohol chains induced by surface tension torque. *Biomacromolecules* 15: 60-65
- Mayer RP, Stowe RA (1965) Mercury porosimetry—breakthrough pressure for penetration between packed spheres. *Journal of Colloid Science* 20:893-911
- Mazza M, Catana D, Vaca-Garcia C, Cecutti C (2009) Influence of water on the dissolution of cellulose in selected ionic liquids. *Cellulose* 16:207-215
- McGenity P, Gane P, Husband J, Engley M (1992) Effects of Interactions between Coating Color Components on Rheology, Water Retention and Runnability. *TAPPI Conference Proceedings* 8:1992-133
- McGregor C, Knight P. Utilizing Process Chemicals to Improve Water Removal. *Paper Technology* 35: 31-42 (1996).
- Mezger TG (2006) *The rheology handbook: for users of rotational and oscillatory rheometers.* Vincentz Network GmbH & Co KG
- Milling A, Mulvaney P, Larson I (1996) Direct measurement of repulsive van der Waals interactions using an atomic force microscope. *Journal of Colloid and Interface Science* 180:460-465
- Mitchell J (1980) The rheology of gels. *Journal of Texture Studies* 11:315-337
- Moan M, Aubry T, Bossard F (2003) Non-linear behaviour of very concentrated suspensions of plate-like kaolin particles in shear flow. *Journal of Rheology* 47:1493
- Moan M, Page A, Carreau PJ, Heuzey M (2002) Rheological behaviour of coating colours: Influence of thickener. *The Canadian Journal of Chemical Engineering* 80:1181-1188
- Mobuchon C, Carreau PJ, Heuzey M (2007) Effect of flow history on the structure of a non-polar polymer/clay nanocomposite model system. *Rheologica Acta* 46:1045-1056
- Møller PCF, Mewis J, Bonn D (2006) Yield stress and thixotropy: On the difficulty of measuring yield stresses in practice. *Soft Matter* 2:274-283
- Mörseburg K, Chinga-Carrasco G (2009) Assessing the combined benefits of clay and nanofibrillated cellulose in layered TMP-based sheets. *Cellulose* 16:795-806
- Nakagaito A, Yano H (2004) The effect of morphological changes from pulp fiber towards nano-scale fibrillated cellulose on the mechanical properties of high-strength plant fiber based composites. *Applied Physics A* 78:547-552

- Nakamura K, Hatakeyama T, Hatakeyama H (1981) Studies on bound water of cellulose by differential scanning calorimetry. *Textile Research Journal* 51:607-613
- Norman B, Moller K, Ek R, Duffy G (1977) Hydrodynamics of papermaking fibers in water suspension BPBIF Symposium of Fibre-Water Interactions 195: 1977-195
- Notley SM, Wågberg L (2005) Morphology of modified regenerated model cellulose II surfaces studied by atomic force microscopy: Effect of carboxymethylation and heat treatment. *Biomacromolecules* 6:1586-1591
- Nuopponen M, Vuorinen T, Jämsä S, Viitaniemi P (2003) The effects of a heat treatment on the behaviour of extractives in softwood studied by FTIR spectroscopic methods. *Wood Science and Technology* 37:109-115
- O'Sullivan AC (1997) Cellulose: the structure slowly unravels. *Cellulose* 4:173-207
- Ovarlez G, Rodts S, Chateau X, Coussot P (2009) Phenomenology and physical origin of shear localization and shear banding in complex fluids. *Rheologica acta* 48:831-844
- Öztürk HB, Potthast A, Rosenau T, Abu-Rous M, MacNaughtan B, Schuster KC, Mitchell JR, Bechtold T (2009) Changes in the intra-and inter-fibrillar structure of lyocell (TENCEL®) fibers caused by NaOH treatment. *Cellulose* 16:37-52
- Pääkkö M, Ankerfors M, Kosonen H, Nykänen A, Ahola S, Österberg M, Ruokolainen J, Laine J, Larsson P, Ikkala O (2007) Enzymatic hydrolysis combined with mechanical shearing and high-pressure homogenization for nanoscale cellulose fibrils and strong gels. *Biomacromolecules* 8:1934-1941
- Pabst W, Gregorová E, Berthold C (2006) Particle shape and suspension rheology of short-fiber systems. *Journal of the European Ceramic Society* 26:149-160
- Pajari H, Koskela H (2010) Consolidation of coating colors - Experimental studies. 11th Advanced Coating Fundamentals Symposium Proceedings: The Latest Advances in Coating Research and Development: 347-359
- Paradis MA, Genco JM, Bousfield DW, Hassler JC, Wildfong V (2002) Determination of drainage resistance coefficients under known shear rate. *Tappi Journal* 1:12-18
- Patel M, Trivedi R (1994) Variations in strength and bonding properties of fines from filler, fiber, and their aggregates. *Tappi Journal* 77: 32-39
- Persello J, Magnin A, Chang J, Piau J, Cabane B (1994) Flow of colloidal aqueous silica dispersions. *Journal of Rheology* 38:1845
- Pierotti R, Rouquerol J (1985) Reporting physisorption data for gas/solid systems with special reference to the determination of surface area and porosity. *Pure & Applied Chemistry* 57:603-619
- Poehler T, Juvonen K, Sneek A (2006) Coating layer microstructure and location of binder: results from SEM analysis. Proceedings of the 9th.TAPPI advanced coating fundamental symposium, Turku. TAPPI Press, Atlanta: 89-100
- Pöhler T, Lappalainen T, Tammelin T, Eronen P, Hiekkataipale P, Vehniäinen A, Koskinen T (2010) Influence of fibrillation method on the character of nanofibrillated

cellulose (NFC) TAPPI Conference on Nanotechnology for the forest products industry, Conference Proceedings: 27-29

Protzman TF, Brown GL (1960) An apparatus for the determination of the minimum film forming temperature of polymer emulsions. *Journal of Applied Polymer Science* 4:81-85

Przybysz K, Czechowski J (1985) The effect of pulp fines on the drying process and paper strength properties. *Cellulose chemistry and technology* 19:197-209

Przybysz K, Szwarcztajn E (1973) Effect of crill on pulp freeness. *Przegląd Papier* 29:105-108

Puisto A, Illa X, Mohtaschemi M, Alava M (2012) Modeling the viscosity and aggregation of suspensions of highly anisotropic nanoparticles. *The European Physical Journal E* 35:1-7

Puisto A, Illa X, Mohtaschemi M, Alava M (2012) Modeling the rheology of nanocellulose suspensions. *Nordic Pulp and Paper Research Journal* 27:277-281

Raisanen KO, Paulapuro H, Karrila SJ (1995) The effects of retention aids, drainage conditions, and pretreatment of slurry on high-vacuum dewatering: a laboratory study. *Tappi Journal* 78:32-39

Ratner B, Hoffman AS, Schoen F, Lemons JE (2004) *Biomaterials science: an introduction to materials in medicine*. Elsevier Academic Press, 2nd Edition.

Richmond F, Co A, Bousfield DW (2012) The Coating of Nanofibrillated Cellulose onto Paper using Flooded and Metered Size Press Methods. 2012 PaperCon Conference *TAPPI 2012* ; (12PAP) 18.

Ricka J, Tanaka T (1984) Swelling of ionic gels: quantitative performance of the Donnan theory. *Macromolecules* 17:662-681

Ridgway CJ, Gane PAC (2002) Dynamic absorption into simulated porous structures. *Colloids and Surfaces A: Physicochemical and Engineering Aspects* 206:217-239

Ridgway CJ, Gane PAC (2003) Bulk density measurement and coating porosity calculation for coated paper samples. *Nordic Pulp & Paper Research Journal* 18:24-31

Ridgway CJ, Gane PAC (2007) Effect of latex and pigment volume concentrations on suspension and consolidated particle packing and coating strength. *Journal of Pulp and Paper Science* 33:71-78

Ridgway CJ, Gane PAC, El AE, Czachor A (2006) Water absorption into construction materials: comparison of neutron radiography data with network absorption models. *Transport in Porous Media* 63:503-525

Ridgway CJ, Gane PAC, Schoelkopf J (2006) Achieving rapid absorption and extensive liquid uptake capacity in porous structures by decoupling capillarity and permeability: nanoporous modified calcium carbonate. *Transport in Porous Media* 63:239-259

Ridgway CJ, Schoelkopf J, Gane PAC (2003) A new method for measuring the liquid permeability of coated and uncoated papers and boards. *Nordic Pulp & Paper Research Journal* 18:377-381

- Ridgway CJ, Schoelkopf J, Gane PAC (2011) Competitive absorption of polar and non-polar liquids into latex bound porous structures of fine ground calcium carbonate. *Transport in Porous Media* 86:945-964
- Ridgway CJ, Schoelkopf J, Matthews GP, Gane PAC, James PW (2001) The effects of void geometry and contact angle on the absorption of liquids into porous calcium carbonate structures. *Journal of Colloid and Interface Science* 239:417-431
- Ritala R, Huiku M (1989) Scaling, percolation and network theories: new insight into papermaking In *Transactions of the 9th Fundamental Research Symposium, Cambridge*: 195-218
- Roper J (2009) Rheology of pigment slurries and coating formulations In *Pigment Coating and Surface Sizing of Paper* (Ed) J Paltakari. *Paperi ja Puu Oy* 10: pp.319-354
- Roper J, Bousfield D, Urscheler R, Salminen P (1997) Observations and proposed mechanisms of misting on high-speed metered size press coaters TAPPI coating conference. *TAPPI Conference proceedings*:1-14
- Roschy A, Fischer K, Kleemann S (2002) Comparison of modern wet-end methods for determination of drainage & retention in laboratory scale. *Wochenblatt für Papierfabrikation* 130:1187-1196
- Saarikoski E, Saarinen T, Salmela J, Seppälä J (2012) Flocculated flow of microfibrillated cellulose water suspensions: an imaging approach for characterisation of rheological behaviour. *Cellulose* 19:647-659
- Saarinen T, Karppinen A, Saarikoski E, Salmela J, Nuopponen M, Laukkanen A, Seppälä, J (2010) A method to correlate floc size to rheological characteristics of microfibrillated cellulose water suspension. *Transactions of the Nordic Rheology Society*: 153-156
- Saito T, Isogai A (2005) TEMPO-mediated oxidation of native cellulose. *Appita Annual Conference* 3:337-340
- Sand A, Kniivilä J, Toivakka M, Hjelt T (2011) Structure formation mechanisms in consolidating pigment coatings—Simulation and visualisation. *Chemical Engineering and Processing: Process Intensification* 50:574-582
- Sandås S, Salminen PJ, Eklund D (1989) Measuring the water retention of coating colors. *Tappi Journal* 72:207-210
- Schmid CF, Switzer LH, Klingenberg DJ (2000) Simulations of fiber flocculation: Effects of fiber properties and interfiber friction. *Journal of Rheology* 44:781
- Schmidt-Thümmes J, Lawrenz D, Kröner H (2009) Latex, In *Pigment Coating and Surface Sizing of Paper* (Ed) J Palatakari, *Paperi ja Puu Oy* 5:207-226
- Schoelkopf J, Gane P, Ridgway C, Matthews GP (2000) Influence of inertia on liquid absorption into paper coating structures. *Nordic Pulp & Paper Research Journal* 15:422-430
- Schoelkopf J, Gane PAC, Ridgway CJ, Matthews GP (2002) Practical observation of deviation from Lucas–Washburn scaling in porous media. *Colloids and Surfaces A, Physicochemical Engineering Aspects* 206:445-454

Schoelkopf J, Ridgway CJ, Gane PAC, Matthews GP, Spielmann DC (2000) Measurement and network modeling of liquid permeation into compacted mineral blocks. *Journal of Colloid and Interface Science* 227:119-131

Seth JR, Cloitre M, Bonnecaze RT (2008) Influence of short-range forces on wall-slip in microgel pastes. *Journal of Rheology* 52:1241

Shirato M, Maurase T, Iwata M (1986) In (Ed) Wakeman J, *Progress in Filtration and Separation*. Elsevier, Amsterdam 4

Siddiqui N, Mills RH, Gardner DJ, Bousfield D (2011) Production and characterization of cellulose nanofibers from wood pulp. *Journal of Adhesion Science and Technology* 25:709-721

Siró I, Plackett D (2010) Microfibrillated cellulose and new nanocomposite materials: a review. *Cellulose* 17:459-494

Sjöberg M, Bergström L, Larsson A, Sjöström E (1999) The effect of polymer and surfactant adsorption on the colloidal stability and rheology of kaolin dispersions. *Colloids and Surfaces A: Physicochemical and Engineering Aspects* 159:197-208

Smith S (1922) The action of the beater in papermaking. *Paper Trade Journal* 106:47-52

Smoluchowski M (1912) On the practical applicability of Stokes' law of resistance, and the modification of it required in certain cases. 5th International Congress in Mathematics, Conference Proceedings, Cambridge 2:192

Sosa A, Carreau P, Tanguy P, Ascanio G, Guerrero C (2006) The effect of thickener on the rheology of coating colours. *Chemical Engineering Communications* 193:917-928

Subramanian R, Hiltunen E, Gane PAC (2011) Potential use of Micro-and Nanofibrillated Cellulose Composites exemplified by Paper. *Cellulose Fibers: Bio-and Nano-Polymer Composites: Green Chemistry and Technology* (Kalia, Susheel; Kaith, B. S.; Kaur, Inderjeet (Eds.)), Chapter 5 Part II Cellulosic Fiber Reinforced Polymer Composites and Nanocomposites. Springer Verlag, 1st Edition. 2011; (ISBN: 978-3-642-17369-1:121):750

Swerin A, Powell R, Ödberg L (1992) Linear and non-linear dynamic viscoelasticity of pulp fiber suspensions. *Nordic Pulp and Paper Research Journal* 7: 78-83

Taipale T, Österberg M, Nykänen A, Ruokolainen J, Laine J (2010) Effect of microfibrillated cellulose and fines on the drainage of kraft pulp suspension and paper strength. *Cellulose* 17:1005-1020

Tanaka A, Hjelt T, Sneek A, Korpela A (2012) Fractionation of Nanocellulose by Foam Filter. *Separation Science and Technology* 47:1771-1776

Tatsumi D, Ishioka S, Matsumoto T (2002) Effect of fiber concentration and axial ratio on the rheological properties of cellulose fiber suspensions. *日本レオロジー学会誌* 30:27-32

Teece LJ, Faers MA, Bartlett P (2011) Ageing and collapse in gels with long-range attractions. *Soft Matter* 7:1341-1351

Thies-Weesie DM, Philipse AP (1994) Liquid permeation of bidisperse colloidal hard-sphere packings and the Kozeny-Carman scaling relation. *Journal of Colloid and Interface Science* 162:470-480

Toivakka M, Eklund D, Bousfield D (1999) Simulation of pigment motion during drying. TAPPI coating conference, Conference Proceedings: 78-84

Toivakka M, Bousfield D (1999) Levelling of coating suspensions. *Journal of pulp and paper science* 25: 183-188

Toivakka M, Kokko A, Salminen P, Urscheler R, Bousfield D (2001) Leveling of surface defects in thin films of pigmented coatings. *Nordic Pulp & Paper Research Journal* 16:246-250

Triantafillopoulos N (1998) Measurement of Fluid Rheology and Interpretations of Rheograms. Kaltec Scientific Inc.

Triantafillopoulos NG (1985) Shear induced anisotropy in the rheology of solids dispersions. Doctoral Dissertation, Western Michigan University 1985

Triantafillopoulos NG (1996) Measurement of fluid rheology and interpretation of rheograms. Kaltec Scientific, Inc. 2nd edition

Triantafillopoulos NG (1996) Paper coating viscoelasticity and its significance in blade coating. TAPPI Press, Atlanta GA

Turbak AF, Snyder F, Sandberg K (1984) Microfibrillated Cellulose-a new composition of commercial significance: 115-123

Uetani K, Yano H (2011) Zeta Potential Time Dependence reveals the Swelling Dynamics of Wood Cellulose Nanofibrils. *Langmuir* 28:818-827

Usher SP, De Kretser RG, Scales PJ (2001) Validation of a new filtration technique for dewaterability characterization. *AIChE Journal* 47:1561-1570

Valencia C, Sanchez M, Ciruelos A, Latorre A, Madiedo J, Gallegos C (2003) Non-linear viscoelasticity modeling of tomato paste products. *Food Research International* 36:911-919

Van Hecke M (2005) Granular matter: A tale of tails. *Nature* 435:1041-1042

Van Loosdrecht M, Lyklema J, Norde W, Schraa G, Zehnder A (1987) Electrophoretic mobility and hydrophobicity as a measured to predict the initial steps of bacterial adhesion. *Applied and Environmental Microbiology* 53:1898-1901

Verwey EJ, Evert JW, Overbeek JTG, Jan TG (1999) Theory of the stability of lyophobic colloids. Dover Publications.com

Wågberg L, Decher G, Norgren M, Lindström T, Ankerfors M, Axnäs K (2008) The build-up of polyelectrolyte multilayers of microfibrillated cellulose and cationic polyelectrolytes. *Langmuir* 24:784-795

Wågberg L, Lindström T (1987) Kinetics of polymer-induced flocculation of cellulosic fibers in turbulent flow. *Colloids and Surfaces* 27:29-42

- Wågberg L, Winter L, Ödberg L, Lindström T (1987) On the charge stoichiometry upon adsorption of a cationic polyelectrolyte on cellulosic materials. *Colloids and Surfaces* 27:163-173
- Wakeman RJ (1985) Filtration theory: formation and structure of compressible filter cakes. In *Mathematical models and design methods in solid-liquid separation*. Springer: 48-82
- Walecka JA (1956) An investigation of low degree of substitution carboxymethylcelluloses. Doctoral Dissertation. Georgia Institute of Technology
- Wallqvist V, Claesson PM, Swerin A, Schoelkopf J, Gane PA (2006) Interaction forces between talc and hydrophobic particles probed by AFM. *Colloids and Surfaces A: Physicochemical and Engineering Aspects* 277:183-190
- Walls HJ, Caines SB, Sanchez AM, Khan SA (2003) Yield stress and wall slip phenomena in colloidal silica gels. *Journal of Rheology* 47:847-868
- Wallström A, Järnström L (2004) The relation between viscoelastic properties of suspensions based on paper coating minerals and structures of the corresponding coating layers. Conference Proceedings Nordic Rheology Conference, Reykjavik, Iceland
- Wang Q, Zhu J, Gleisner R, Kuster T, Baxa U, McNeil S (2012) Morphological development of cellulose fibrils of a bleached eucalyptus pulp by mechanical fibrillation. *Cellulose* 19:1631-1643
- Weber E, Moyers-González M, Burghilea TI (2012) Thermorheological properties of a Carbopol gel under shear. *Journal of Non-Newtonian Fluid Mechanics* 12:65-72
- Weise U, Maloney T, Paulapuro H (1996) Quantification of water in different states of interaction with wood pulp fibres. *Cellulose* 3:189-202
- Whittle M, Dickinson E (1997) Stress overshoot in a model particle gel. *Journal of Chemical Physics* 107:10191-10200
- Wildfong VJ, Genco JM, Shandsa JA, Bousfield DW (1998) Filtration Resistance Determination of Fibrous Suspensions utilizing a Rapid Drainage Tester. TAPPI FFluid Mechanics Committee: 89-91
- Willenbacher N, Hanciogullari H, Rädle M (1998) New laboratory test to characterize immobilization and dewatering of paper coating colors. *Tappi Journal* 82:193-202
- Willenbacher N, Hanciogullari H, Wagner HG (1997) High shear rheology of paper coating colors—more than just viscosity. *Chemical and Engineering Technology* 20:557-563
- Wollny K (2001) New rheological test method to determine the dewatering kinetics of suspensions. *Applied Rheology* 11:197-202
- Wu J, Yu D, Chan C, Kim J, Mai Y (2000) Effect of fiber pretreatment condition on the interfacial strength and mechanical properties of wood fiber/PP composites. *Journal of Applied Polymer Science* 76:1000-1010
- Yamamoto M (1958) The viscoelastic properties of network structure III. Normal stress effect (Weissenberg Effect). *Journal of the Physical Society of Japan* 13:1200-1211

- Yang H, Yan R, Chen H, Lee DH, Zheng C (2007) Characteristics of hemicellulose, cellulose and lignin pyrolysis. *Fuel* 86:1781-1788
- Yeo K, Maxey MR (2010) Dynamics of concentrated suspensions of non-colloidal particles in Couette flow. *Journal of Fluid Mechanics* 649:205-231
- Yeow YL, Leong Y, Khan A (2006) Non-Newtonian flow in parallel-disk viscometers in the presence of wall slip. *Journal of Non-Newtonian Fluid Mechanics* 139:85-92
- Yeow YL, Leong Y, Khan A (2007) Error introduced by a popular method of processing parallel-disk viscometry data. *Applied Rheology* 17:66415-66493
- Yoshida H, Hatakeyama T, Hatakeyama H (1992) Effect of water on the main chain motion of polysaccharide hydrogels. *Viscoelasticity of Biomaterials*: 217-230
- Yoshinaga F, Tonouchi N, Watanabe K (1997) Research progress in production of bacterial cellulose by aeration and agitation culture and its application as a new industrial material. *Bioscience, Biotechnology and Biochemistry* 61:219-224
- Yziquel F, Carreau P, Moan M, Tanguy P (1999) Rheological modelling of concentrated colloidal suspensions. *J Non-Newtonian Fluid Mechanics* 86:133-155
- Yziquel F, Moan M, Carreau P, Tanguy P (1999) Non-linear viscoelastic behaviour of paper coating colors. *Nordic Pulp and Paper Research Journal* 14:37-47
- Zauscher S, Klingenberg DJ (2001) Friction between cellulose surfaces measured with colloidal probe microscopy. *Colloids and Surfaces A: Physicochemical and Engineering Aspects* 178:213-229
- Zhang Q, Archer LA (2002) Poly (ethylene oxide)/silica nanocomposites: structure and rheology. *Langmuir* 18:10435-10442
- Zhang X, Stebbing DW, Saddler JN, Beatson RP, Kruus K (2000) Enzyme treatments of the dissolved and colloidal substances present in mill white water and the effects on the resulting paper properties. *Journal of Wood Chemistry and Technology* 20:321-335
- Zhong F, Mitchell KL, Hays CC, Choukroun M, Barmatz M, Kargel JS (2009) The rheology of cryovolcanic slurries: motivation and phenomenology of methanol-water slurries with implications for Titan. *Icarus* 202:607-619

Nanocellulose applied in paper making suspensions may introduce additional strength properties in traditional products, and when considered for coatings may deliver oil and gas barrier properties.

Although many studies have been conducted relating to papermaking furnishes and their water suspensions while including nanocellulose containing materials, these rheological investigations were conducted independently from conditions of dynamic dewatering.

Once reliable rheological measurements were designed and the methodology established, this thesis goes on to analyse the possible structures attained by nanocellulose containing suspensions in combination with macroscopic fibres, pigments and dispersing polymers, traditionally used as water retention aids.



ISBN 978-952-60-5696-8
ISBN 978-952-60-5697-5 (pdf)
ISSN-L 1799-4934
ISSN 1799-4934
ISSN 1799-4942 (pdf)

Aalto University
School of Chemical Technology
Department of Forest Product Technology
www.aalto.fi

**BUSINESS +
ECONOMY**

**ART +
DESIGN +
ARCHITECTURE**

**SCIENCE +
TECHNOLOGY**

CROSSOVER

**DOCTORAL
DISSERTATIONS**